Experimental Studies of Gas Phase Reactions Using the Turbulent Flow Tube Technique

by

John Vincent Seeley

B.S. Chemistry
Central Michigan University
(1989)

Submitted to the Department of Chemistry
in Partial Fulfillment of the Requirements
for the Degree of

Doctor of Philosophy in Chemistry

at the

Massachusetts Institute of Technology

May, 1994

Signature of Author _____
Department of Chemistry
February 22, 1994

Certified by _____
Mario J. Molina
Martin Professor of Environmental Chemistry
Thesis Supervisor

Accepted by _____
Glenn A. Berchtold
Professor of Chemistry
Chairman, Departmental Committee on Graduate Students

Science

This doctoral thesis has been examined by a Committee of the Department of Chemistry as Follows:

Professor Jeffrey I. Steinfeld _____ Chairman

Professor Mario J. Molina _____
Thesis Supervisor

Professor Ronald G. Prinn _____
Department of Earth, Atmospheric and Planetary Sciences

Experimental Studies of Gas Phase Reactions Using the Turbulent Flow Tube Technique

by

John Vincent Seeley

Submitted to the Department of Chemistry on February 22, 1994
in partial fulfillment of the requirements for the
Degree of Doctor of Philosophy in Chemistry

Abstract

This thesis describes the development and implementation of the turbulent flow tube technique, a new method for studying gas phase reaction kinetics. The plausibility of the turbulent flow tube technique has been examined using a numerical model. Several experimental studies of key fluid dynamical processes have also been performed. These experiments include flow visualization of reactant mixing, pitot tube measurements of velocity profiles, reactant wall loss measurements, and pulsed tracer studies. The validity of the turbulent flow tube technique has been verified by determining the rate constants of several well characterized reactions. The reactions studied are $H + O_3 \rightarrow OH + O_2$, $H + Cl_2 \rightarrow HCl + Cl$, $Cl + NO_2 \rightarrow ClNO_2$, $Cl + CH_4 \rightarrow HCl + CH_3$, and $Cl + O_3 \rightarrow ClO + O_2$. The turbulent flow tube technique has also been used to measure the reaction rate constants of two reactions of the hydroxyl radical which are believed to play an important role in atmospheric chemistry: $OH + HNO_3 \rightarrow H_2O + NO_3$ and $OH + H_2O_2 \rightarrow H_2O + HO_2$. The rate constants for both of these reaction have been measured over a wide range of pressures and temperatures. Finally, a high pressure ionizing mass spectrometer has been developed which will ultimately be used as a detection technique in a turbulent flow tube system.

Thesis Supervisor: Dr. Mario J. Molina
Title: Martin Professor of Environmental Chemistry

Table of Contents

Acknowledgments

I would like to thank my research advisor, Mario Molina, for his endless supply of knowledge, patience, and support. The idea of a turbulent flow tube system was originally his, and I am grateful for being asked to help in its development.

An enormous amount of thanks and credit must be given to John Jayne. In my first few years at MIT, John and I worked together on much of the research that makes up this thesis. It has been a privilege to work with such an amazing laboratory craftsman.

I would also like to thank several other individuals who had a direct impact on my thesis research: John Abbatt for selflessly sharing his knowledge of flow tube systems; Keith Beyer for many enlightening discussions; Bob Boldi for his instruction on the rudiments of numerical modeling; Jamie Gardner for providing late night rides into work, free meals, and a lot of good advice; Tun-li Shen for his collaboration on the API-MS research; Darryl Spencer for answering frequent computer questions; Debbie Sykes for administrative support; Paul Woolridge for his large supply of insightful answers; and all the other members of the MIT Atmospheric Chemistry Group.

Special thanks are given to Professor Robert E. Kohrman of Central Michigan University who six years ago took the time to talk to me about graduate school. I am certain that I would have never obtained a Ph.D. from MIT without his advice and encouragement.

Finally, I would like to thank my family. Throughout the last five years they have constantly given me the support and affirmation that was necessary to complete my studies at MIT. My mother and father provided a great deal of emotional and financial stability which helped smooth out some of the bumpier times. My wife, Stacy, was always there to give what was needed whether it was congratulations, condolences, or inspiration – but most of all she always kept reminding me to believe in myself. I consider myself a fortunate person to be surrounded by such a loyal and loving family.

Chapter I: Introduction

The field of chemical kinetics is primarily devoted to studying the temporal nature of chemical reactions. In perhaps more practical terms, chemical kinetics attempts to determine the rates at which reactions occur and the factors that influence these rates. The studies reported in this thesis are concerned with the experimental investigation of gas phase reaction kinetics.

I.1 Review of Experimental Methods in Gas Phase Kinetics

The characterization of elementary gas phase reactions often represents a substantial experimental challenge. Elementary reactions typically involve extremely reactive species. As a result, reactants must often be generated immediately before use and the concentrations of reactants must be kept at low levels to avoid interfering reactions. Elementary reactions also typically involve small molecules. The high mobilities of these gas phase species can easily create conditions where concentration variations due to reactant transport are confused with variations due to chemical removal. Thus, the experimental systems used to study gas phase reactions must be able to cleanly generate reactants, detect low levels of reactant concentrations, and discern between chemical removal and transport processes. Two systems have been used extensively in the past: flash photolysis and flow tubes. Several excellent reviews of both of these methods can be found in the literature [*Finlayson-Pitts and Pitts*, 1986; *Howard*, 1979; *Kaufman*, 1984; *Kaufman*, 1985; *Steinfeld et al.*, 1989].

In flash photolysis systems, temporal variations in reactant concentrations are predominantly due to chemical reaction. Under such conditions, reaction rate constants can be directly determined by observing the decay of reactant concentrations (or the appearance of products) as a function of time. Flash photolysis systems are subject to three main

requirements: (1) labile reactants must be produced in a pulse-like fashion over time periods shorter than the time scale of the reaction; (2) the time scale of the reaction must be shorter than the time scale of reactant transport; and (3) the detection method must have a time response faster than the time scale of the reaction. In flash photolysis reactive species are produced by a pulse of light emitted from a lamp or laser. The progress of the reaction is often monitored by observing the concentration of the reactants using an optical detection scheme.

When applicable, flash photolysis has proved to be an extremely effective method for characterizing reactions over a wide range of temperatures and pressures. Unfortunately, this technique is difficult to use for many reactions: radical-radical reactions are difficult to study because creating accurately known concentrations of species via photolysis is a formidable task; reactions for which there are no direct photolytic reactant precursors are problematic because reactants need to be generated in extremely short time spans; and reactions where unwanted photolysis readily occurs are also troublesome because subsequent secondary reactions often complicate the data analysis.

In contrast to flash photolysis, flow tube systems create conditions where the chemical removal of reactants is equally balanced by reactant transport. Under such conditions the reactant concentrations reach steady state and kinetic information is given in terms of spatial variations in the reactant densities. The biggest requirement of flow tube systems is that the effects of transport on the reactant concentration distributions must be understood before kinetic parameters can be determined. This often means that a detailed knowledge of the fluid dynamics within the reactor must be obtained.

Unlike flash photolysis, the flow tube technique can be used to study virtually every class of reaction. Because reactants are created in a continuous fashion, thermal and microwave discharges can be used to generate a wide variety of atoms and radicals. Flow tubes also allow reactants to be made through a series of titration reactions. This feature permits accurately known concentrations of radical species to be generated, allowing

radical-radical reactions to be studied with relative ease. The steady state nature of the flow tube method allows the use of detection schemes with slow time responses, such as mass spectrometry or magnetic resonance methods. Unfortunately, the effects of reactant transport have traditionally been believed to only be well defined at low pressures (1 torr < P < 10 torr) and at moderate temperatures (T > 250 K). As a result, rate constants are rarely determined outside these ranges using the flow tube technique.

I.2 Motivation for Research

Due to the limitations of flash photolysis and flow tube systems, there is a large number of reactions (radical-radical reactions in particular) that have been studied only at moderate temperatures and low pressures. Predictions of the behavior of such reactions outside the narrow range of conditions where direct observations have been made are often based on extrapolations.

Recently, it has been discovered that a multitude of gas phase bimolecular reactions display complex dependencies on temperature and pressure. Examples of such reactions are $OH + HNO_3$, $OH + HO_2$, and $ClO + HO_2$. Contrary to what is expected for simple bimolecular reactions, these reactions often possess rate constants with a non-Arrhenius temperature dependence (often a negative temperature dependence) and a dependence on total pressure [*Smith*, 1991]. The conventional theoretical model of bimolecular reactions (i.e., two reactants colliding, passing through a single transition state, and breaking apart to form two new products) cannot account for such behavior. As a result, several new theories have been put forth to explain the experimental observations [*Mozurkewich and Benson*, 1984; *Mozurkewich*, 1986; *Phillips*, 1990]. Most of these theories maintain that the reactants pass through a transition state to form an intermediate complex which can either revert back to reactants or go through a second transition state to form products. The multi-step nature of these reactions has led them to be called *complex mode reactions* or *indirect bimolecular reactions.*

Due to the lack of a firm understanding of complex mode reactions, it is difficult to predict the rate constants and products of these reactions outside the range of conditions where there have been direct experimental observations. As a result, it is essential that complex mode reactions be studied over a wide range of pressures and temperatures. Most of the reactions of this type are radical-radical reactions which can only be accurately characterized using flow tube techniques. Because of the narrow operating range of conventional flow tube techniques, the pressure and temperature dependence of complex mode reaction and their reaction products are often poorly defined.

I.3 Research Overview and Thesis Outline

The main goal of the research described in this thesis was to create an experimental technique which will allow a broad spectrum of gas phase reactions to be studied over a wide range of conditions. Ideally, such a technique should be capable of determining reaction rate coefficients at temperatures ranging from 190 K to 300 K and pressures ranging from 1 to 760 torr. The research described in this thesis is a first step in producing such a technique. We have created a flow tube method which can operate at pressures and temperatures well outside of the ranges accessible to the conventional flow tube technique. This improvement has been made by operating in the turbulent flow regime instead of the laminar flow regime.

This thesis describes the development and implementation of the turbulent flow tube technique. Chapter II first reviews the fluid dynamics of flow in tubes and examines the plausibility of the turbulent flow tube technique using a numerical flow model. Chapter III describes the results of several experimental studies designed to determine the effects of operating in the turbulent flow regime. Chapters IV and V describe kinetic studies performed using the turbulent flow tube technique on several simple reactions whose pressure and temperature dependencies have been well characterized by other laboratories using conventional flow tube and flash photolysis techniques. Chapter VI presents results

from the kinetic studies of two OH reactions whose pressure and temperature dependencies were previously uncertain. Finally, chapter VII presents preliminary results from current research on creating improved reactant detection schemes. Central to this effort is the production of a mass spectrometer system which provides high sensitivity at high pressures.

References for Chapter I

Finlayson-Pitts, B. J. and J. N. P. Pitts, *Atmospheric Chemistry*, Wiley, New York, 1986.

Howard, C. J., Kinetic measurements using flow tubes, *J. Phys. Chem.*, *83*, 3, 1979.

Kaufman, F., Kinetics of elementary radical reactions in the gas phase, *J. Phys. Chem.*, *88*, 4909, 1984.

Kaufman, F., Rates of elementary reactions: measurements and applications, *Science, 230,* 393, 1985.

Mozurkewich, M., and S. W. Benson, Negative activation energies and curved Arrhenius plots. 1. Theory of reactions over potential wells, *J. Phys. Chem.*, *88,* 6429, 1984.

Mozurkewich, M., Reactions of HO_2 with free radicals, *J. Phys. Chem.*, *90,* 2216, 1986.

Phillips, L. F., Collision-theory calculations of rate constants for some atmospheric radical reactions over the temperature range 10-600 K, *J. Phys. Chem., 94,* 7482, 1990.

Smith, I. W. M., Radical-radical reactions: kinetics, dynamics and mechanisms, *J. Chem. Soc. Faraday. Trans., 87,* 2271, 1991.

Steinfeld, J. I., J. S. Francisco, and W. L. Hase, *Chemical Kinetics and Dynamics.* Prentice Hall, Englewood Cliffs, New Jersey, 1989.

Chapter II: Models of Reactive Flow in Tubes

II.1 Introduction

The steady state nature of the flow tube technique creates conditions where kinetic information is expressed in terms of spatial concentration variations. Before kinetic parameters can be measured, the relationship between reactant concentration distributions and the rate constant must be determined. This relationship cannot be accurately resolved without knowledge of the fluid dynamics present in the flow tube.

This chapter examines the fluid dynamics of flow tube systems. The first section contains a qualitative description of flow in tubes. In the next section, a description of the conventional flow tube approach is presented along with an examination of its limitations. In the final section the plausibility of the turbulent flow tube method is assessed using a numerical model.

II.2 Fluid Dynamics of Flow in Tubes

This section describes basic fluid dynamic concepts which are pertinent to the flow tube technique. A more detailed discussion of these topics can be found in the texts of *Fahien* [1983], *Davies* [1972], *Ward-Smith* [1980] and the treatise of *Hoyerman* [1984].

II.2.1 General Description

A schematic of a flow tube system is depicted in figure 1. Flow tubes are usually constructed from a piece of tubing 50 to 100 cm in length with an internal radius between 1 and 3 cm.

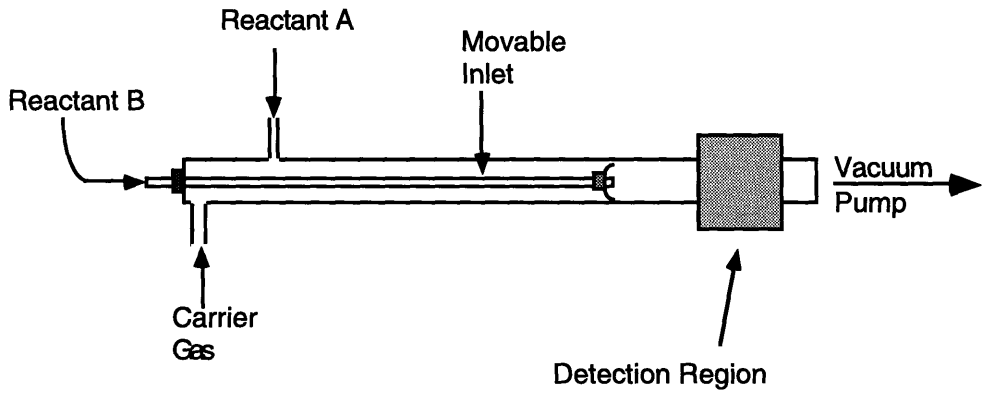

Figure 1. Schematic of discharge flow system for the study of the reaction $A + B \rightarrow$ products.

Gas flow down the tube is caused by an axial pressure gradient. In the laboratory, pressure gradients are typically created by injecting an inert carrier gas (usually He, Ar or N_2) at one end of the tube and removing the gas at the opposite end with a vacuum pump. The average velocity of the gas, $\bar{u}$, is typically set between 500 cm s^{-1} and 2000 cm s^{-1}. Trace amounts of reactants are continuously added to the flow. One reactant is often injected near the rear of the flow tube through a side arm inlet. A second reactant is usually injected through a movable glass tube.

The force pushing the gas down the tube is opposed by a viscous retarding force originating at the flow tube walls. At the entrance of the flow tube, only the molecules adjacent to the walls experience a viscous retardation. As the gas passes down the tube, the region under the influence of the viscous force, the *boundary layer*, increases in size. In the process of building up the boundary layer, a velocity profile develops which is zero at the flow tube walls and a maximum near the axis of the tube. The axial distance required for the boundary layer to reach the centerline of the tube is known as the *entrance length*. The flow in the region upstream of the entrance length changes with

axial position due to the axial dependence of the boundary layer thickness; flow in this region is often called *developing flow*. Downstream of the entrance length, the fluid dynamics do not vary greatly with axial position and hence the flow is considered to be *fully developed*. It is important to note that perturbations to the flow can destroy the boundary layer. In a flow tube, sudden changes in tube diameter or protruding reactant injectors can lead to boundary layer breakdown.

The motion of a fluid as it passes down the tube is particularly dependent upon the ratio of convective momentum transport to viscous momentum dissipation. The convective transport of momentum is proportional to $\rho\,\bar{u}^2$, where ρ is the density of the gas. The viscous dissipation of momentum is proportional to $\mu\,\bar{u} / 2\,a$, where μ is the viscosity coefficient of the gas and a is the internal radius of the flow tube. This dimensionless ratio is known as the Reynolds number, *Re*, and is given by

$$Re = \frac{2\,a\,\bar{u}\,\rho}{\mu} \tag{1}$$

For low values of *Re*, the dominance of viscous dissipation leads to damping of all lateral fluid movement creating *laminar flow*. For large values of *Re*, viscous dissipation is unable to damp out lateral fluid movement and *turbulent flow* results. Empirically it has been found that laminar flow is generally stable at $Re < 2000$ and that turbulent flow is stable at $Re > 3000$. Conditions between $2000 < Re < 3000$ are often classified as *transitional* because oscillations between turbulent and laminar flow can be observed under controlled conditions. For a flow tube with $\bar{u} = 1000$ cm s^{-1}, $a = 1.25$ cm, $T = 298$ K, and argon as the carrier gas, laminar flow is stable (i.e., Re < 2000) when the pressure is less than 85 torr.

Laminar flow is characterized by streamlined fluid convection. The velocity profile for fully developed laminar flow is given by

$$u(r) = 2\,\bar{u}\left[1 - \left(\frac{r}{a}\right)^2\right] \qquad (2)$$

where $u(r)$ is the velocity in the axial direction and r is the radial coordinate. The velocity profile present before the entrance length is reached depends on the method of gas injection. The value of the entrance length, L_{ent}, is commonly estimated to be $L_{ent} = 0.112\ a\,Re$ [*Ward-Smith,* 1980]. For a flow tube with $\bar{u} = 1000$ cm s^{-1}, $a = 1.25$ cm, $T = 298$ K, and Ar as the carrier gas, the entrance length equals 3.3 cm when $P = 1$ torr and 66 cm when $P = 20$ torr. Within the laminar flow regime, molecular diffusion is the sole mechanism for reactant mixing. It is important to note that the rate of transport via molecular diffusion is essentially inversely proportional to the total pressure; thus, the rate of reactant mixing decreases as the pressure is increased.

Turbulent flow is characterized by a multitude of eddies with rapidly oscillating trajectories. Unlike laminar flow, the fully developed velocity profile for turbulent flow cannot be exactly determined from simple theoretical considerations. However, a good empirically derived approximation is given by

$$u = u_{max}\left(1 - \frac{r}{a}\right)^{1/n} \qquad (3)$$

where u_{max} is the velocity at $r = 0$ and n is a parameter which depends on Re. For the case of $Re = 5000$, the value of n is roughly equal to 5.16 and $u_{max} / \bar{u} = 1.31$ [*Fox and McDonald,* 1985]. Figure 2 shows a comparison of fully developed velocity profiles found in laminar and turbulent flow. As is readily seen from figure 2, the turbulent velocity profile is flatter than the laminar profile in the central portion of the tube. Near the flow tube walls the turbulent velocity profile declines sharply due to increased viscous damping.

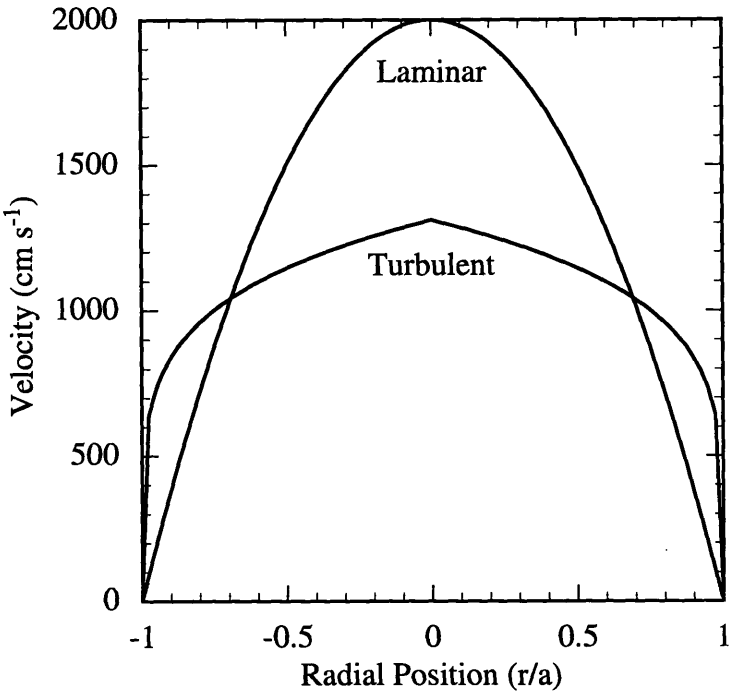

Figure 2. Fully developed velocity profile for the laminar and turbulent flow regimes with $\bar{u}$ = 1000 cm s^{-1}. Laminar flow velocity profile was calculated using equation 2. The turbulent velocity profile was calculated for *Re* = 5000 using equations 3, 17, and 18.

Within the turbulent flow regime, random motion occurs at the molecular level and at a larger size scale due to eddy motion. Eddy mixing is often modeled by a diffusion coefficient which is similar to the velocity profile in shape. In turbulent flow, the region near the wall ($r < 0.9\ a$) is commonly called the viscous sublayer since it is relatively free of eddy motion. The region in the central portion of the tube is commonly called the turbulent core.

Within the transitional regime ($2000 < Re < 3000$), the velocity profile is more peaked than the profiles found for $Re > 3000$. Unfortunately, no closed analytic expressions for the velocity profile in the transitional regime have been reported.

II.2.2 The Continuity Equation

One of the main challenges associated with flow tube experiments is assessing the importance of each process which can lead to spatial concentration variations. These processes include convection, diffusion, heterogeneous reactions (reactions with the interior surfaces of the reactor) and homogenous reactions. All of these processes can be mathematically modeled by a set of coupled partial differential equations commonly known as the continuity equations. The continuity equations can be derived from mass conservation principles assuming isothermal and constant density conditions. The continuity equation for reactive species i in a steady state flow reactor is given by

$$\nabla(E_i \nabla C_i) - \nabla(u\, C_i) + K_i = 0 \tag{4}$$

where C_i is the concentrations of species i, E_i is the diffusivity of i, u is the convective velocity, and K_i is the total rate of chemical production of species i. The diffusivity, E_i, is defined as the sum of the molecular diffusion coefficient of species i, D_i, and the eddy diffusion coefficient, D_e. The effect of heterogeneous removal of species i on the wall of the flow tube is modeled by the boundary condition

$$\left(\frac{\partial C_i}{\partial r}\right)_{r=a} = -\left(\frac{\gamma_i\, \bar{\omega}_i}{4\, E_i} C_i\right)_{r=a} \tag{5}$$

where γ_i is the collision efficiency for wall loss and $\bar{\omega}_i$ is the average molecular velocity of species i.

For a flow reactor where the only reaction is, $A + B \rightarrow products$, the relevant continuity equations are given by

$$\nabla(E_A \nabla C_A) - \nabla(u\, C_A) - k C_A C_B = 0 \tag{6a}$$

$$\nabla(E_B \nabla C_B) - \nabla(u\, C_B) - kC_A C_B = 0 \qquad (6b)$$

where k is the bimolecular reaction rate constant.

In order to determine k, the values of u, C_A, C_B, E_A and E_B must be known throughout a region in the reaction vessel. In principle, all of these quantities could be directly measured over a wide range of positions and k could then be determined numerically. This approach, however, has the serious drawback of requiring a large number of measurements. As a result, the more common approach has been to operate under conditions where the values for several of these quantities can be accurately predicted and only a few measurements are necessary.

A simplifying procedure that is used in virtually every flow tube experiment is the generation of pseudo-first-order conditions. Pseudo-first-order conditions are created when the concentration of one of the reactants is constant with respect to time and space (for demonstration purposes, B is chosen to be constant). For this assumption to be accurate, B must be thoroughly mixed and not substantially depleted by chemical reactions. The effect of homogeneous removal on C_B is minimized by injecting an excess quantity of B. In practice it has been found that minimal errors are incurred if the amount of B injected into the system is greater than 10 times the amount of A injected into the system [*Howard*, 1979].

In the region where C_B can be considered independent of position, only the continuity equation of the limiting reactant, A, needs to be considered. The continuity equation for A becomes

$$\nabla(E_A \nabla C_A) - \nabla(u\, C_A) - k^I C_A = 0 \qquad (7)$$

where k^I is the pseudo-first-order reaction rate coefficient given by $k^I = k\, C_B$.

II.3 Previous Flow Tube Approaches

This section briefly reviews the basic elements of conventional flow tube experiments. Special attention has been given to describing the constraints which limit these studies. Several authors have written excellent reviews of the flow tube technique [*Kaufman* ,1984; Kaufman, 1985; *Howard* , 1979; and *Finlayson-Pitts and Pitts* , 1986].

II.3.1 The Conventional Flow Tube Approach

The vast majority of flow tube studies have been performed in laminar flow conditions. Typically it is assumed that the concentration of the limiting reactant, C_A, depends only upon axial position and that reactant transport in the axial direction is exclusively due to convection (i.e., axial diffusion can be neglected). Under these assumptions the continuity equation of the limiting reactant becomes

$$-\bar{u}\frac{dC_A}{dz} - k^I C_A = 0 \tag{8}$$

Examination of equation 8 shows that these assumptions are equivalent to stating that each limiting reactant molecule travels at velocity equal to $\bar{u}$; a condition commonly known as *plug flow*.

The explicit relationship between C_A and k^I can be determined by integrating equation 8 to yield

$$C_A(z) = C_A(z_0)\exp\left(-\frac{k^I(z-z_0)}{\bar{u}}\right) \tag{9}$$

where $C_A(z_0)$ is the concentration of A at an axial position z_0. The radial and angular independence of C_A leads to three experimental advantages: (1) the exact shape of the velocity profile does not effect C_A ; (2) the value of C_A can be determined as a function of position without the need of radial and angular resolution; and (3) the data analysis is relatively straight forward, i.e., as long as $\bar{u}$ and C_B are known, the bimolecular rate constant can be determined by measuring C_A as a function of axial position.

A typical experiment proceeds through several steps in order to determine the bimolecular rate constant. First the injection rate of the excess reactant, B, is set at a known value. The value of C_B is calculated assuming that B is evenly mixed throughout the region downstream of the movable inlet. Next the concentration of the limiting reactant is determined as a function of axial position in the region downstream of the movable inlet. In principle, this could be done by moving the detector to different axial positions; however, a more common approach is to keep the detector at a fixed position and vary the position of the movable inlet. The logarithm of C_A is then plotted as a function of the injector-detector distance, z, and a linear least-squares fit is made to the data points. The value of k' is determined by multiplying the resulting slope by $-\bar{u}$. This process is repeated for several values of C_B and then a linear least-squares fit is made to a plot of k' *vs.* C_B. The slope of the plot is equal to the experimentally determined bimolecular rate constant.

II.3.2 Limitations of the Conventional Flow Tube Approach

The limitations of the conventional flow tube approach are primarily due to the breakdown of plug flow conditions. For laminar flow, the plug flow approximation is only accurate when axial diffusion and radial concentration gradients are negligible. Axial diffusive effects are substantial only at low pressures ($P < 3$ torr) and can be easily remedied by including the axial diffusion term into the continuity equation [*Howard,*

1979]. Unfortunately, radial concentration gradients cannot be as easily assessed, and as a result, represent the biggest limiting factor for conventional flow tube studies.

There are two main sources of radial concentration gradients in the laminar flow regime. First, radial concentration gradients are formed when radial transport of the limiting reactant is much slower than the rate of chemical removal. When radial transport is slow the limiting reactant molecules are confined to their original radial positions. Reactants in the center of the tube have shorter reaction times than those near the walls due to the peaked velocity profile of laminar flow. Subsequently, the degree of homogeneous chemical depletion increases near the flow tube walls. Radial concentration gradients become more pronounced with increasing pressure because diffusive transport correspondingly decreases. It has generally been found that rate constants determined in laminar flow using the plug flow approximation are unreliable when the pressure is greater than 10 torr [*Howard*, 1979].

Radial concentration gradients are also formed if heterogeneous reactions occur to an appreciable extent (i.e., γ becomes large). For many species the value of γ has been found to drastically increase as the temperature decreases. Although the reactivity of the walls can be lessened by the use of coatings, γoften becomes prohibitively large at temperatures below 250 K [*Howard*, 1979].

II.3.3 Previous Efforts to Improve the Flow Tube Technique

In order to determine kinetic parameters in high pressure laminar flow conditions ($P > 10$ torr) a more detailed approach must be used. Several research groups have attempted to assess the effects of radial concentration gradients using the following continuity equation for fully developed laminar flow which includes the axial and radial diffusion terms

$$D_A \left(\frac{1}{r} \frac{\partial}{\partial r} r \frac{\partial C_A}{\partial r} + \frac{\partial^2 C_A}{\partial z^2} \right) - 2\bar{u} \left(1 - \frac{r^2}{a^2} \right) \frac{\partial C_A}{\partial z} - k^I C_A = 0 \qquad (10)$$

where D_A is the molecular diffusion coefficient of the limiting reactant. A solution to equation 10 cannot be found in closed form but can be expressed in terms of an infinite series [*Walker*, 1961; *Brown*, 1978]. *Poirier and Carr* [1971] and *Keyser* [1984] have carried out measurements with this approach at pressures up to 15 and 100 torr, respectively. This technique has two main disadvantages: (1) the uncertainty of the calculated rate constant increases as the pressure or wall reactivity increases; and (2) as the pressure is increased it becomes increasingly difficult to create fully developed laminar flow. As a result of these constraints, this approach has been infrequently used.

Recently, a new flow tube method has been developed by *Abbatt et al.* [1990]. They have created a flow tube reactor in which the values of u and C_A can be experimentally determined as functions of radial and axial position. Rate constants are determined by plugging C_A and u into the continuity equation and numerically solving for k. With this method they have determined rate constants in both laminar and turbulent flow conditions at pressures ranging from 7 torr to nearly 400 torr. Although this approach can generate accurate rate constants, the experimental simplicity of the conventional flow tube technique has been sacrificed. It remains to be seen whether this approach will be used extensively in the future.

II.3.4 Conclusions from Past Flow Tube Studies

Past implementations of the flow tube technique have been primarily performed in laminar flow conditions. The majority of these studies have used the plug flow approximation to determine the relationship between the limiting reactant distribution and the rate constant. Due to the peaked velocity profile of laminar flow, the plug flow approximation breaks down as the pressure is increased above 10 torr. In low pressure conditions, however, the reactant molecules experience many collisions with the flow tube wall; making the technique highly susceptible to heterogeneous interferences.

Several efforts have been made to create flow tube methods which extend the limitations of the conventional flow tube technique. Unfortunately, the resulting approaches have been infrequently used because of their experimental complexity.

II.4 Numerical Flow Tube Model

In principle, the plug flow approximation would be accurate regardless of radial transport considerations if the velocity profile was flat. As shown in section II.2, the velocity profiles found in turbulent flow are much flatter than those found in laminar flow. Therefore, the plug flow approximation could potentially be more accurate in turbulent flow than in high pressure laminar flow. The higher operating pressures of a turbulent flow technique could also reduce reactant interaction with the flow tube walls and allow rate constants to be determined at lower temperatures.

Turbulent flow reactors have been used extensively in the field of chemical engineering. In many cases, the plug flow approximation has been found to accurately model the output of industrial turbulent flow reactors [*Denbigh and Turner,* 1984]. A turbulent flow reactor has also been developed at Princeton by Dryer et al. for the study of reactions involved in high temperature combustion processes [*Hochgreb and Dryer*, 1992]. In their studies the plug flow approximation has been used without incurring significant errors.

A numerical flow tube model was created in order to test the hypothesis that operating in turbulent flow will allow the plug flow approximation to be used at pressures greater than 10 torr and lead to a reduction in reactant-wall interactions. Simulations were performed for both laminar and turbulent flow in either developing or fully developed flow.

II.4.1 Model Construction

General Parameters

The numerical model was used to simulate a 50 cm long flow tube with an internal diameter of 1.25 cm. The simulated carrier gas was argon (at 298 K) with a viscosity of 227 x 10^{-6} g cm^{-1} s^{-1} and an average velocity of 1000 cm s^{-1}. Chlorine atoms were considered to be the limiting reactant.

Continuity Equations

The following two-dimensional continuity equation was used to model the flow tube

$$\frac{1}{r}\frac{\partial}{\partial r}\left(E_A\, r\frac{\partial C_A}{\partial r}\right) - \frac{\partial}{\partial z}(u\, C_A) - k^I C_A = 0 \qquad (11)$$

A model which included the axial diffusion term was also created; however, it was found that including axial diffusion had little effect on the spatial distribution of C_A except at pressures below 5 torr. The boundary conditions for equation 11 at the tube wall and centerline were respectively

$$\left(\frac{\partial C_A}{\partial r}\right)_{r=a} = -\left(\frac{\gamma\,\bar{\omega}}{4\,E_A} C_A\right)_{r=a} \qquad (12)$$

$$\left(\frac{\partial C_A}{\partial r}\right)_{r=0} = 0 \qquad (13)$$

The boundary condition at z = 0 was $C_A(r, z{=}0) = 100$ (i.e., the concentration of the limiting reactant was assumed to be constant throughout the tube cross section at $z = 0$).

Velocity Profiles

The velocity profile used for fully developed laminar flow was given by equation 2. For developing laminar flow conditions the following velocity profile proposed by *Cambell and Slattery* [1963] was used

$$u = u_{\max} \frac{y}{\delta}\left(2 - \frac{y}{\delta}\right) \quad \text{for} \quad 0 \le y \le \delta \tag{14}$$

$$u = u_{\max} \qquad \text{for} \quad \delta < y \le a \tag{15}$$

where y is the radial distance from the wall, $y = r - a$, and δ is the thickness of the boundary layer. The value of u_{max} was given by

$$u_{\max} = \frac{\bar{u}}{1 - \frac{2}{3}\frac{\delta}{a} + \frac{1}{6}\left(\frac{\delta}{a}\right)^2} \tag{16}$$

The mathematical relationship between axial position and the boundary layer thickness is rather lengthy so the reader is referred to *Cambell and Slattery* [1963] for details.

In turbulent flow conditions equation 3 was used for the fully developed velocity profile. The value of u_{max} was given by

$$u_{max} = \frac{(n+1)(2n+1)}{2n^2}\bar{u} \tag{17}$$

where n is a parameter which was estimated using

$$n = 1.78\ (Re)^{1/8} \tag{18}$$

[*Fox and McDonald*, 1985]. In developing conditions, the following velocity profile based on the model of *Na and Lu* [1973] was used

$$u = u_{max} \left(\frac{y}{\delta}\right)^{1/n} \qquad \text{for } 0 \le y \le \delta \tag{19}$$

$$u = u_{max} \qquad \text{for } \delta < y \le a \tag{20}$$

The value of u_{max} was given by

$$u_{max} = \frac{\bar{u}}{1 - \frac{2}{(n+1)}\frac{\delta}{a} + \frac{1}{(2n+1)}\left(\frac{\delta}{a}\right)^2} \tag{21}$$

The relationship between δ and axial position for turbulent flow conditions has been determined empirically [*Barbin and Jones*, 1963] and theoretically [*Na and Lu*, 1973]; however, no closed mathematical expressions for $\delta(z)$ are available. As a result, an expression was derived by assuming that the boundary layer in a tube grows at a rate similar to that found for boundary layer growth over a flat plate. This is a commonly used approximation [*Kay and Nedderman*, 1985]. In turbulent flow, the thickness of the boundary layer on a flat surface has been found to be proportional to $z^{4/5}$ where $z = 0$ at the edge of the plate [*Kay and Nedderman*, 1985]. Thus, it was assumed that in a flow tube the boundary layer thickness was given by

$$\delta(z) = g z^{4/5} \tag{22}$$

where g is a constant. The value of g was determined by setting $\delta = a$ at $z = L_{ent}$ resulting in $g = a / (L_{ent}^{4/5})$. Assuming $L_{ent} = 50\ a$, the boundary layer thickness in turbulent flow is given by

$$\delta(z) = 0.043\ a^{1/5}\ z^{4/5} \tag{23}$$

The evolution of the turbulent velocity profile predicted using equation 23 with equations 19-21 was found to be similar to the empirical results of *Barbin and Jones* [1963] and the theoretical results of *Na and Lu* [1973].

Diffusivity

The molecular diffusion coefficient of Cl in Ar was calculated, using the method recommended by *Reid et al.* [1987], to be 140 $cm^2\ s^{-1}$ (at 1 torr Ar). The eddy diffusion coefficient used in both fully developed turbulent flow and developing turbulent flow was based on the relation proposed by *Pinho and Fahien* [1981]. Their expression is given by

$$D_e = \overline{D}_e \left\{ \frac{1}{1.123\left[1+2.345\left(\frac{r}{a}\right)^2\right]\left[1-\left(\frac{r}{a}\right)^2\right]} + \frac{1}{0.000137(Re)^{1.75}\left(1-\frac{r}{a}\right)^3} \right\}^{-1} \tag{24}$$

where $\overline{D}_e$ is the average value of the eddy diffusion coefficient given by

$$\overline{D}_e = 0.014\ \bar{u}\ a\ (Re)^{-1/8} \tag{25}$$

For a flow tube with $\bar{u}$ = 1000 cm s^{-1}, a = 1.25 cm, and Re = 5000, the average eddy diffusion coefficient is approximately 6 $cm^2\ s^{-1}$. The radial dependence of the eddy diffusion coefficient is depicted in figure 3.

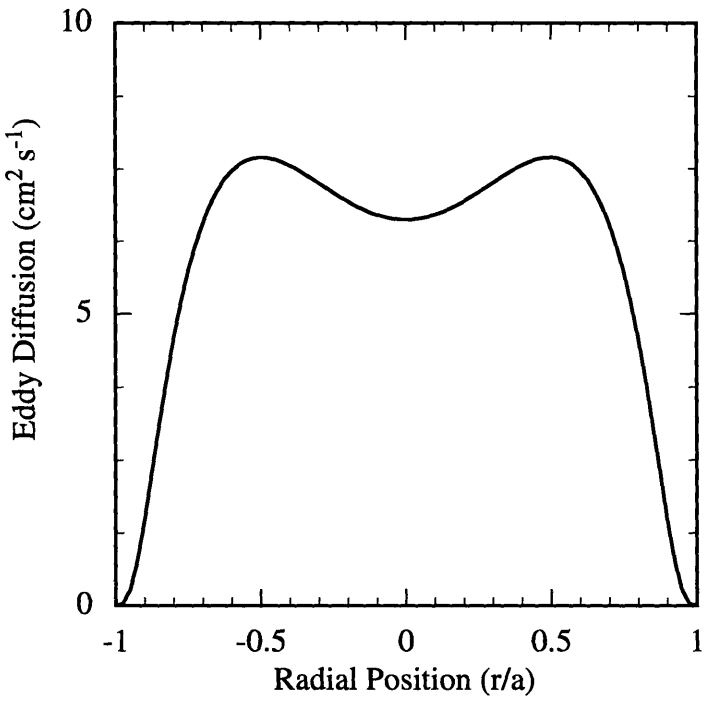

Figure 3. Eddy diffusion coefficient for fully developed turbulent flow calculated using equations 24 and 25(Re = 5000, $\bar{u}$ = 1000 cm s^{-1}, P = 210 torr, a = 1.25 cm).

Numerical Solution

Solution of equation 11 was based on the Crank-Nicholson method for solving parabolic partial differential equations [*Hoffman*, 1992]. The spatial concentration distribution of C_A was determined at 123,000 mesh points (41 points in the radial direction and 3000 points in the axial direction). The wall boundary condition was calculated using a cubic Newtonian extrapolation. For $Re < 2000$, the laminar flow expressions for u and E_A were used. For $Re > 3000$, the turbulent flow expressions for u and E_A were used. In the transitional regime ($2000 < Re < 3000$) separate simulations were performed using laminar and turbulent flow expressions. For low pressure laminar flow conditions the results of the model were checked against results from analytic models [*Brown,* 1978; *Ferguson et al.*, 1969] and found to be in good agreement.

Radial Concentration Averaging

After C_A was determined as a function of axial and radial position, C_A was radially averaged to simulate the sampling of real detection schemes. Three radial averaging schemes were used: centerline sampling where only the concentration at $r = 0$ is monitored

$$\overline{C_A}(z) = C_A(0,z) \tag{26}$$

core sampling where the concentration is averaged over the region of $0 < r < a/2$

$$\overline{C_A}(z) = \frac{8}{a^2}\int_0^{a/2} C_A(r,z)\, r\, dr \tag{27}$$

and full cross sectional sampling where the concentration is averaged over the region of $0 < r < a$

$$\overline{C_A}(z) = \frac{2}{a^2}\int_0^{a} C_A(r,z)\, r\, dr \tag{28}$$

II.4.2 Results and Discussion

Wall Loss

The model was first used to simulate the dependence of reactant wall loss on pressure (and hence Reynolds number). Reactant wall loss was expressed in terms of an observed first order decay constant, k_w. The simulation was performed as follows: For a prescribed set of P and γ, the value of C_A was determined throughout the tube with k^I equal to zero. C_A was then radially averaged at nine axial positions starting at $z = 10$ cm progressing up to $z = 50$ cm in 5 cm increments. A line was then fit to a plot of ln $\overline{C_A}(z)$

vs. z. The value of k_w was then calculated by multiplying the slope by $-\bar{u}$.

Simulations of wall losses in fully developed flow and developing flow yielded similar results regardless of the cross sectional averaging scheme used. Figure 4 contains the results of this study for three different values of γ in fully developed flow conditions with full cross sectional averaging.

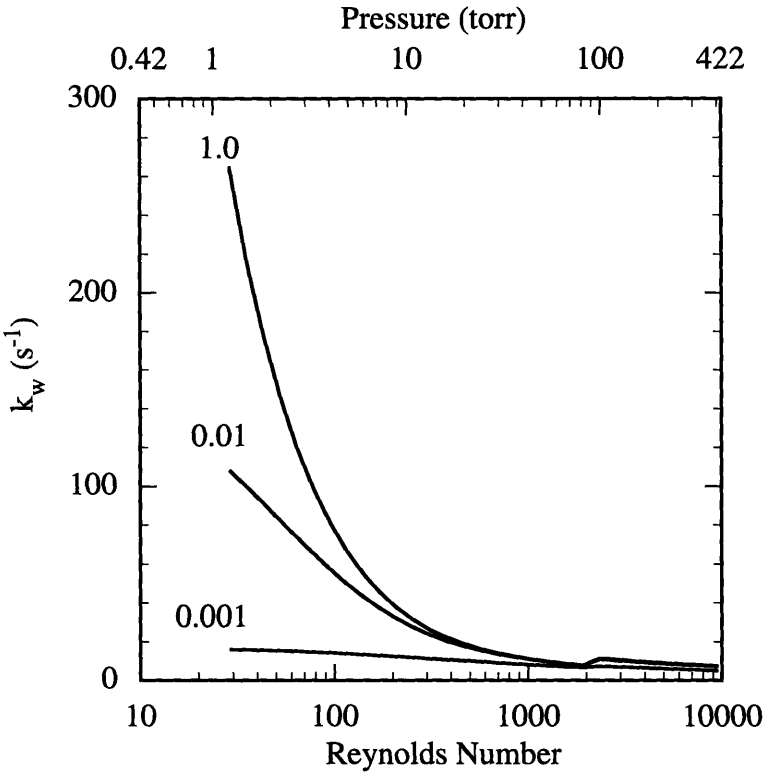

Figure 4. First order wall loss as determined using fully developed numerical model. Numbers on left end of curve represent the value of γ.

As can be seen from figure 4, the model results indicate that wall interactions are greatly reduced as the pressure is increased. When the flow goes into turbulence, the wall reaction rate goes up slightly due to increased radial mobility from eddy diffusion. At

low pressures the model results are in good agreement with the analytic model of *Ferguson et al.* [1969].

Accuracy of the Plug Flow Approximation

The model was used to simulate a standard flow tube experiment like that described in section II.3.1. The error incurred in making the plug flow approximation was determined as a function of pressure (and hence Reynolds number). The simulation was performed in several steps: For a prescribed set of P and γ, k^I was set at value ranging from 0 s^{-1} to 200 s^{-1} in 20 s^{-1} increments. The model was then used to calculate C_A throughout the tube. C_A was then radially averaged at nine axial positions . After a line was fit to a plot of ln $\overline{C_A}(z)$ *vs.* z , the value of k^I_{obs} was calculated by multiplying the slope of the fit by -$\bar{u}$. The values of k^I_{obs} were plotted as a function of k^I. The slope of this line represents the ratio of the rate constant calculated assuming plug flow to the actual rate constant (k_{obs} / k). This ratio will be called the relative observed rate constant for the discussion below.

Figure 5 contains results obtained for unreactive walls (i.e., $\gamma = 0$) in fully developed flow conditions. For low pressure laminar flow conditions ($P < 5$ torr) the relative observed rate constant is greater than 0.9; i.e., the model predicts that the plug flow approximation can be used in this regime without incurring relative errors greater than 10%. As the pressure is increased within the laminar flow regime, the value of k_{obs} / k decreases due to the formation of radial concentration gradients. At the high pressure limit of the laminar flow regime the value of k_{obs} / k reaches a minimum of approximately 0.5.

In the turbulent flow regime, the accuracy of the plug flow approximation is increased due to the flattened velocity profile: relative observed rate constants are greater than 0.9. Thus according to the model, the plug flow approximation could be used in fully developed turbulent without incurring relative errors greater than 10%.

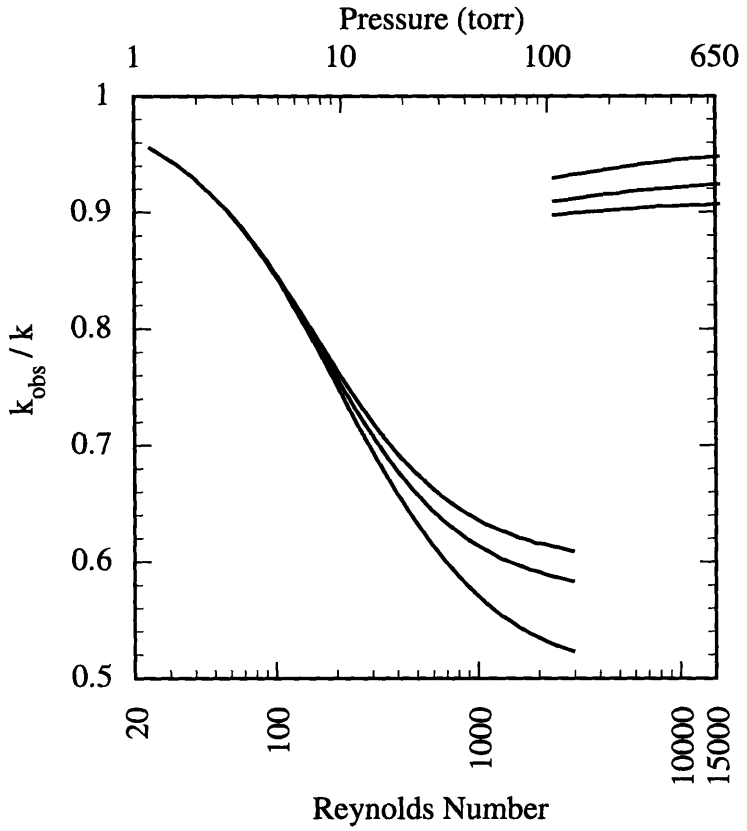

Figure 5. Relative rate constant determined using numerical model to simulate fully developed flow with $\gamma = 0$. Curves in both the laminar and turbulent flow case represent radial averaging over the following regions: lowest curve $r = 0$; middle curve $0 < r < 0.5\ a$; highest curve $0 < r < a$.

At pressures above 5 torr the value of the relative observed rate constant depends upon which radial averaging scheme is used, with the minimum values of k_{obs} / k obtained when centerline sampling is used. This effect results from the combination of the peaked velocity profile and limited radial transport which cause radial concentration gradients to become more pronounced as axial position is increased. Fortunately, in the turbulent flow regime the values of k_{obs} / k agree to within 5% regardless of which radial averaging scheme is used.

The simulation results obtained in developing flow conditions for unreactive walls (i.e., $\gamma = 0$) are depicted in figure 6. As can be seen by comparing figure 5 and figure 6, operating in developing flow conditions generally reduces the error incurred when the plug flow approximation is used. This result is due to the flattening of the velocity profile in the entrance region. The most pronounced difference between the simulation predictions occurs in the high pressure laminar flow regime where the entrance region extends throughout the entire flow tube.

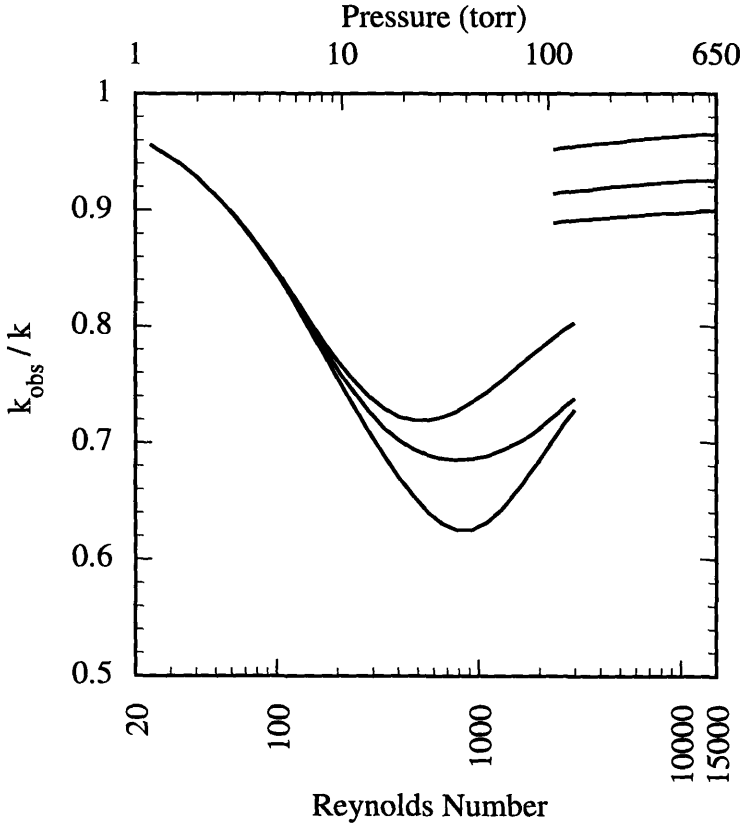

Figure 6. Relative rate constant determined using numerical model to simulate developing flow conditions with $\gamma = 0$. Curves in both the laminar and turbulent flow case represent radial averaging over the following regions: lowest curve $r = 0$; middle curve $0 < r < 0.5\ a$; highest curve $0 < r < a$.

Note that the observed rate constants predicted in developing and fully developed turbulent flow conditions agree to within 3%. This good agreement is resultant of the fact that the difference between the fully developed velocity profile and the completely flat profile at the entrance of the tube is rather small in the turbulent flow regime.

The case of high wall reactivity is depicted in figures 7 and 8 for fully developed and developing flow conditions respectively.

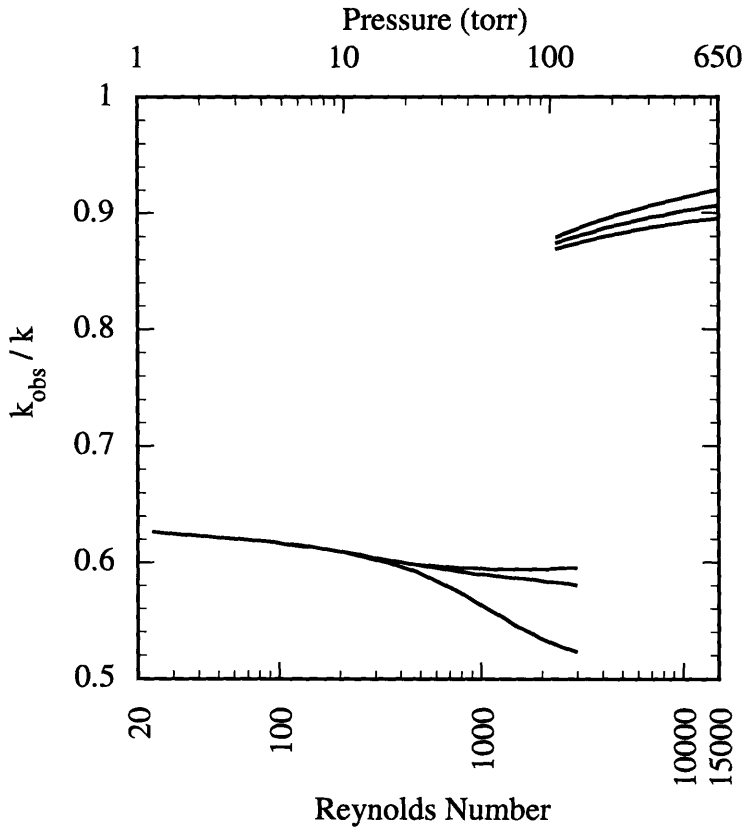

Figure 7. Relative rate constant determined using numerical model to simulate fully developed flow conditions with $\gamma = 1$. Curves in both the laminar and turbulent flow case represent radial averaging over the following regions: lowest curve $r = 0$; middle curve $0 < r < 0.5\ a$; highest curve $0 < r < a$.

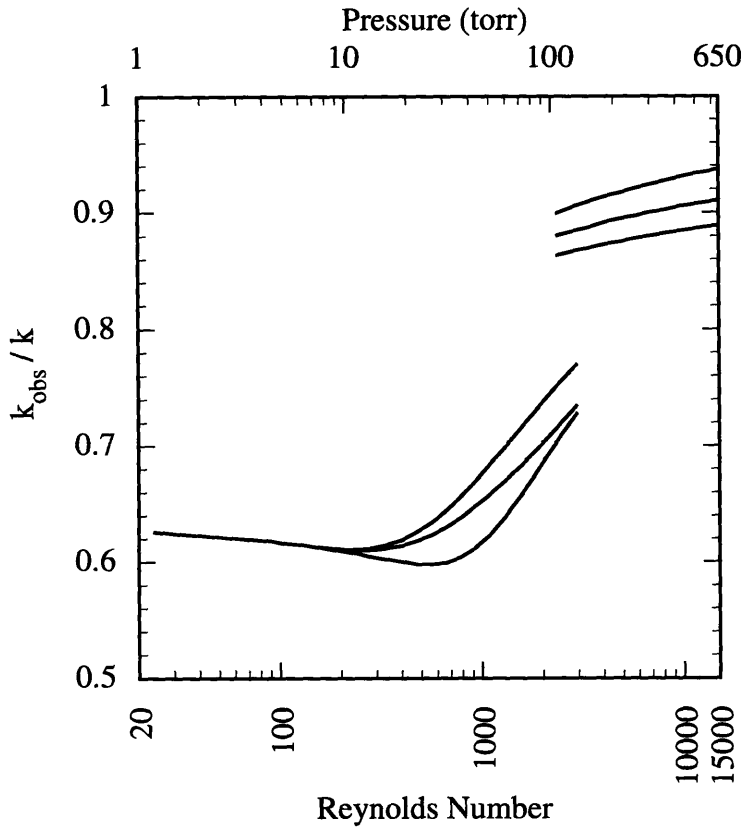

Figure 8. Relative rate constant determined using numerical model to simulate developing flow conditions with $\gamma = 1$. Curves in both the laminar and turbulent flow represent radial averaging over the following regions: lowest curve $r = 0$; middle curve $0 < r < 0.5\ a$; highest curve $0 < r < a$.

Within the low pressure laminar regime, the observed rate constants deviate substantially from the actual rate constants. As the pressure is increased the values of k_{obs} / k become similar to the non-reactive wall case. For pressures above 30 torr, the values of k_{obs} / k calculated for reactive and non-reactive wall conditions agree to within 10%.

II.4.3 Conclusions from Model Simulations

The model results indicate that operating in turbulent flow conditions allows the plug flow approximation to be used without incurring errors greater than 15% (regardless of wall reactivity, the state of flow development, and the radial averaging scheme). This level of error is similar to that found when operating in low pressure laminar flow with non-reactive wall conditions. Thus we conclude that operating a standard flow tube system in the turbulent flow regime represents a plausible approach for extending the pressure and temperature limitations of the flow tube technique.

References for Chapter II

Abbatt, J. P. D., K. L. Demerjian, and J. G. Anderson, A new approach to free radical kinetics: radially and axially resolved high-pressure discharge flow with results for OH + C_2H_6, C_3H_8, n-C_4H_{10}, n-C_5H_{12} → products at 297 K, *J. Phys. Chem., 94,* 4566, 1990.

Barbin, A. R., and J. B. Jones, Turbulent flow in the inlet region of a smooth pipe, *Trans. ASME, J. Basic Engng., 85,* 29, 1963.

Brown, R. L., Tubular flow reactors with first-order kinetics, *J. Res. Nat. Bur. Stand., 83,* 1, 1978.

Cambell, W. D., and J. C. Slattery, Flow in the entrance of a tube, *Trans. ASME, Ser. E, 85,* 41, 1963.

Davies, J. T., *Turbulence Phenomena,* Academic Press, New York, 1972.

Denbigh, K. G. and J. C. R. Turner, *Chemical Reactor Theory, 3rd ed.*, Cambridge University Press, Cambridge, 1984.

Fahien, R. W., *Fundamentals of Transport Phenomena*, McGraw-Hill, New York, 1983.

Ferguson, E. F., F. C. Fehsenfeld, and A. L. Schmeltekopf, Flowing afterglow measurements of ion-neutral reactions, *Advan. At. Mol. Phys., 5,* 1, 1969.

Finlayson-Pitts, B. J. and J. N. P. Pitts, *Atmospheric Chemistry*, Wiley, New York, 1986.

Fox, R. W. and A. T. McDonald, *Introduction to Fluid Mechanics, 2nd ed.,* John Wiley and Sons, New York, 1985.

Hochgreb, S. and F. L. Dryer, Decomposition of 1,3,5 - trioxane at 700-800 K, *J. Phys. Chem., 96,* 295, 1992.

Hoffman, J. D., *Numerical Methods for Engineers and Scientist,* McGraw-Hill, New York, 1992.

Howard, C. J., Kinetic measurements using flow tubes, *J. Phys. Chem., 83,* 3, 1979.

Hoyerman, K. H., "Interactions of Chemical Reactions, Transport Processes, and Flow" in *Physical Chemistry, An Advanced Treatise:Kinetics of Gas Reactions*, edited by H. Eyring, D. Henderson, and W. Jost, 6B, 931, Academic Press, 1984.

Kaufman, F., Kinetics of elementary radical reactions in the gas phase, *J. Phys. Chem. 88,* 4909, 1984.

Kaufman, F., Rates of elementary reactions: measurements and applications, *Science, 230,* 393, 1985.

Kay, J. M. and R. M. Nedderman, *Fluid Mechanics and Transfer Processes,* Cambridge University Press, Cambridge, 1985.

Keyser, L. F., High-pressure flow kinetics. A study of the OH + HCl reaction from 2 to 100 torr, *J. Phys. Chem., 88,* 4750, 1984.

Na, T. Y., and Y. P. Lu, Turbulent flow development characteristics in channel inlets, *Appl. Sci. Res., 27*, 425, 1973.

Pinho, M. D. and R. W. Fahien, Correlation of eddy diffusivities for pipe flow, *AIChE J, 27,* 170, 1981.

Poirier, R. V., and R. W. Carr, The use of tubular flow reactors for kinetic studies over extended pressure ranges, *J. Phys. Chem., 75,* 1593 (1971).

Reid, R. C., J. M. Prausnitz and T. K. Sherwood, *The Properties of Gases and Liquids, 4th ed.,* McGraw-Hill, New York, 1987.

Streeter, V. L., *Handbook of Fluid Dynamics, 1st ed.*, McGraw-Hill, 1961.

Walker, R. E., Chemical reaction and diffusion in a catalytic tubular reactor, *Phys. of Fluids., 4,* 1211, 1961.

Ward-Smith, A. J., *Internal Fluid Flow: The Fluid Dynamics of Flow in Pipes and Ducts*, Clarendon Press, Oxford, 1980.

Chapter III: Fluid Dynamics Experiments

III.1 Introduction

In the previous chapter, it was shown that operating a flow tube system in the turbulent flow regime is a plausible approach for extending the pressure limits of the flow tube technique. This chapter presents results which help characterize the fluid dynamics found in flow tubes under laminar and turbulent flow conditions. Four different studies were performed: flow visualization studies, velocity profile measurements, reactant wall loss measurements, and pulsed tracer studies.

III.2 Flow Visualization Studies

Reactants must be thoroughly mixed in order to have well defined experimental conditions. In conventional flow tube experiments, where the pressures are low ($P < 10$ torr), transport via molecular diffusion is often rapid enough to allow reactants to be well mixed shortly after being injected into the flow tube. At higher pressures, thorough mixing of reactants becomes a greater challenge due to the slowing of molecular diffusion.

In order to observe the mixing characteristics of reactants in flow tubes, we have performed a series of flow visualization studies. The chemiluminescent reaction $O + NO \rightarrow NO_2 + h\nu$ was used to visualize reactant flow patterns. Similar flow visualization studies have been performed by *Worsnop et al.* [1989].

III.2.1 Experimental Details

A schematic of the apparatus used for this study is depicted in figure 1. The flow tube was constructed from a Pyrex glass tube (100 cm long, 2.4 cm i.d.). The main carrier gas, argon from a liquid argon tank (Airco, 99.999%), was injected at the rear of the flow tube. The flow tube gas was pumped by an Edwards model EM2-80 vacuum pump (1500 L min^{-1}). The bulk velocity of the gas, $\bar{u}$, was approximately 1500 cm s^{-1}. All flows were monitored with calibrated Tylan mass flow meters and pressures were measured using 0-10 and 0-1000 torr MKS Baratron manometers. Readings from the pressure gauge and the flow meters were monitored using a microcomputer equipped with a National Instruments A/D board.

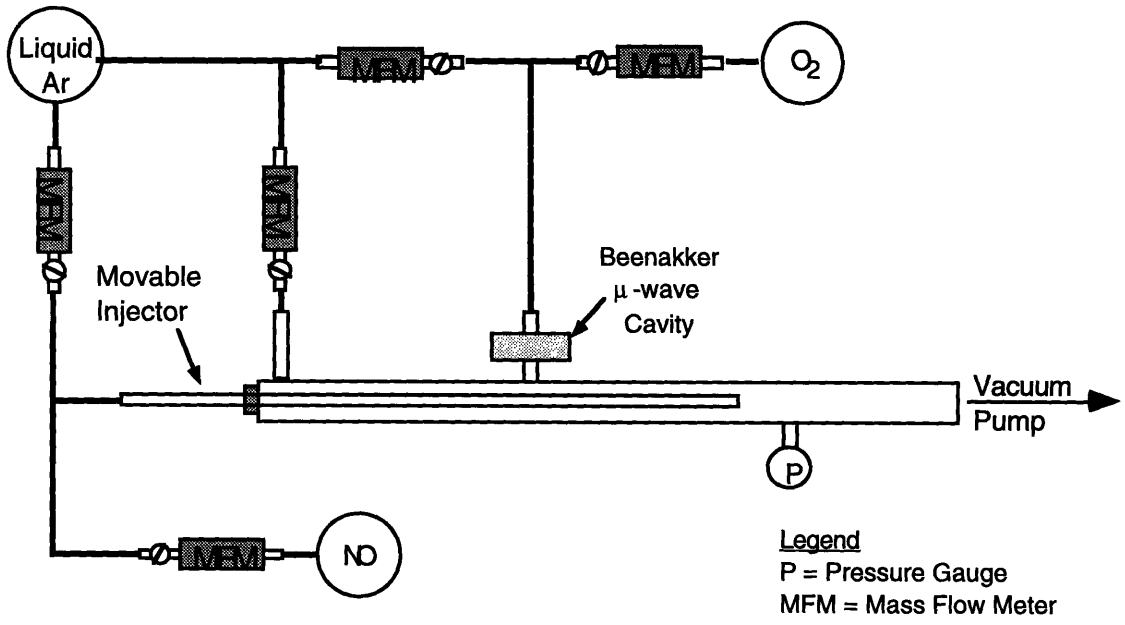

Figure 1. Schematic of apparatus used to perform flow visualization experiments.

Oxygen atoms were generated by passing Ar with a trace amount of O_2 through a Beenakker-type microwave discharge cavity [*Beenakker,* 1976]. Beenakker cavities were used because of their ability to maintain stable discharges at high pressures. Oxygen atoms were injected into the flow tube through a side arm inlet located 30 cm from the upstream end of the flow tube. Trace amounts of NO were injected into the flow through a movable glass inlet (6 mm o.d.) or through a side arm inlet at the rear of the flow tube.

III.2.2 Results and Discussion

The mixing of reactants injected through the movable inlet was investigated by injecting an NO mixture through this inlet. The tip of the movable inlet was located 50 cm downstream of the oxygen atom injection point. Reactant mixing was observed in the last 20 cm of the flow tube.

At a pressure of 1 torr, the green chemiluminescent glow resulting from the O + NO reaction extended radially outward from the tip of the movable injector to the walls of the flow tube. As the pressure was increased, the green glow became more confined to the center of the flow tube. At pressures above 10 torr the glow was contained within a narrow beam. Figure 2 qualitatively shows the glow patterns observed when using an open tube injector.

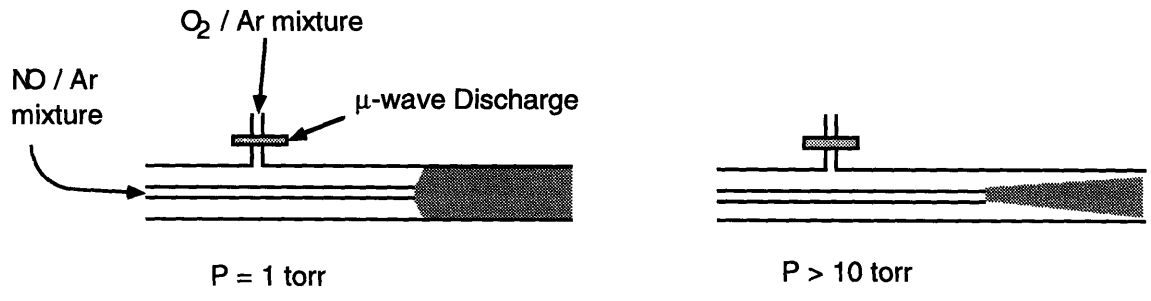

Figure 2. Flow visualization results with open tube movable injector. The shaded pattern represents the observed glow pattern.

The previously mentioned mixing results are in agreement with the theoretical prediction of *Taylor* [1952]. His studies indicated that the time necessary for diffusive mixing to reduce a radial concentration inhomogeneity to 5% of its initial value can be estimated by

$$t_{mix} = \frac{a^2}{5D} \tag{1}$$

where D is the diffusion coefficient of the species of interest. This relation can be converted to a mixing distance by using the plug flow approximation to give

$$z_{mix} = \frac{\bar{u}\, a^2}{5D} \tag{2}$$

In laminar flow conditions, the pressure dependence of the mixing distance in centimeters is calculated to be approximately $z_{mix} = 3.6\ P$ (in torr) for $D_{NO}\ P = 120\ cm^2\ s^{-1}$ torr, $\bar{u} = 1500\ cm\ s^{-1}$, and $a = 1.2$ cm. Thus, at 1 torr the glow is predicted to be well mixed after 3 cm. For pressures above 10 torr in the laminar flow regime, the glow is not predicted to be well mixed at distances less than 30 cm. Within the turbulent flow regime, the calculated mixing distance is still much larger than that of low pressure laminar flow: using a value of $10\ cm^2\ s^{-1}$ for the eddy diffusion coefficient (see chapter II equation 25) the mixing length is greater than 20 cm.

In order to enhance the rate of reactant mixing at higher pressures, we experimented with devices designed to promote intense turbulent mixing at the tip of the movable injector. It was found that when a fan-shaped Teflon piece was placed on the tip of the movable injector, the glow patterns observed at $Re > 700$ were radially homogeneous within 5 cm of the tip of the moveable inlet. This Teflon piece will be referred to as the "turbulizer". For $P > 5$ torr and $Re < 700$ the mixing was also improved when the turbulizer was placed at the tip of the movable inlet; however, the glow patterns were not

radially homogeneous within 5 cm of the tip of the movable inlet. Figure 3 qualitatively shows the glow patterns observed when using an open tube injector with the turbulizer placed at the tip.

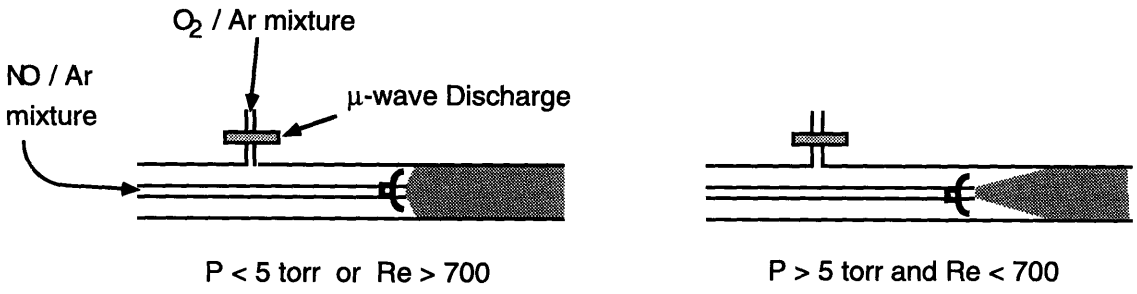

Figure 3. Flow visualization results obtained with open tube movable injector fitted with a turbulizer. The shaded pattern represents the are observed glow pattern.

In order to visualize the mixing of reactants injected through a side arm inlet, NO was injected at the rear of the flow tube (30 cm upstream of the O-atom side arm injection point). At $P < 5$ torr the observed glow became radially homogeneous within 5 cm downstream of the O-atom injection point. At $P > 5$ torr a significant portion of the glow remained confined to the region next to the wall of the flow tube, gradually diffusing inward. However, when this glow pattern reached the turbulizer it rapidly mixed across the cross section of the tube. Figure 4 qualitatively shows the observed glow patterns found for this configuration.

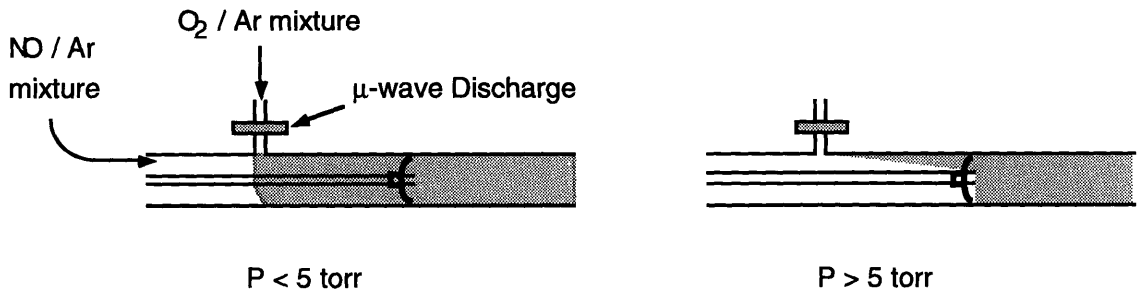

Figure 4. Flow visualization results with NO injected upstream of the O-atom inlet and the turbulizer on the end of the movable inlet.

III.2.3 Conclusions

The flow visualization studies lead to three main conclusions: (1) when a simple open tube movable injector is used, reactants are not well mixed when $P > 5$ torr; (2) when a device which promotes turbulent mixing is fixed to the end of the movable inlet, the reactants are well mixed when $P < 5$ torr or when $Re > 700$; and (3) even if the turbulizer is in place, when $P > 5$ torr and $Re < 700$ reactant mixing is poor.

III.3 Velocity Profile Measurements

The shape of the velocity profile often has a large impact on the concentration distribution of the limiting reactant. In fully developed flow conditions the velocity profile can be accurately predicted. In developing flow conditions (the conditions which will likely be present for high pressure flow tube systems), the form of the velocity profile is less certain. In this section we describe measurements of the velocity profiles found in a standard flow tube configuration in both laminar and turbulent flow conditions.

Velocity profiles were determined using a pitot tube which allows the difference between the static pressure and the impact pressure of a fluid to be determined. The

relationship between the fluid velocity and the difference between the impact and static pressures is given by

$$u = \sqrt{\frac{2\,\Delta p}{\rho}} \tag{3}$$

where ρ is the gas density and Δp is the difference between the impact and static pressures. Pitot tubes have been frequently used in the past to determine the velocities of fluids. There have been several monographs written which thoroughly outline their use [*Breyer and Pankhurst*, 1971; *Emrich,* 1981].

III.3.1 Experimental Details

Figure 5 contains a schematic of the apparatus used for this study. A Plexiglas tube (140 cm long, 1.905 cm i.d.) served as the flow tube. Nitrogen from a liquid nitrogen tank was used as the carrier gas. The flow tube gas was pumped by an Edwards model EM2-80 vacuum pump (1500 L min^{-1}). The bulk velocity of the gas, $\bar{u}$, ranged from 500 to 2000 cm s^{-1}. The flow was monitored with a calibrated Tylan mass flow meter. The temperature in the flow tube was determined using a thermocouple transducer.

Radially resolved gas velocities were determined by measuring the difference between the impact pressure and the static pressure of the gas. The impact pressure was determined using a 1 mm o.d. pitot tube held parallel to the direction of the flow. The static pressure was determined at the tube wall through four ports (1.6 mm i.d.) drilled perpendicular to the direction of the flow. The ports were located at an axial position approximately 20 cm from the downstream end of the flow tube. Each port was thoroughly inspected for burrs which could lead to erroneous pressure determinations; none were found. The tip of the pitot tube was approximately 2 cm downstream of the static pressure ports. The radial position of the tip of the pitot tube was controlled by a

translator. The static pressure was determine using a 0-1000 torr MKS capacitance manometer. The difference between the impact pressure and the static pressure was determined using a MKS differential pressure gauge (1 torr full scale).

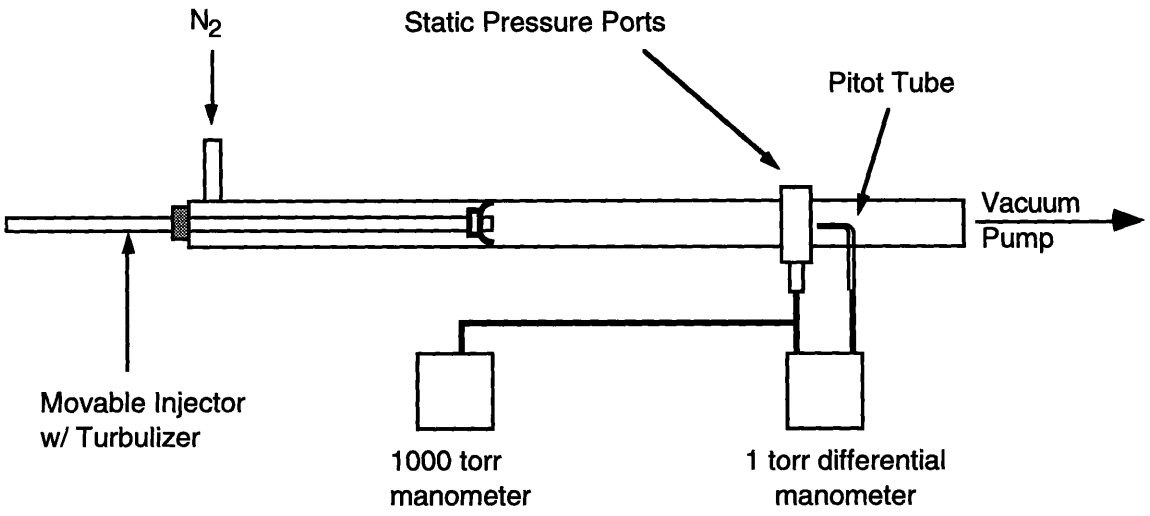

Figure 5. Schematic of apparatus used to make velocity profile measurements.

The tip of the movable inlet (with the turbulizer in place) was set at a known distance from the tip of the pitot tube. The velocity was then determined at 15 different radial positions. This procedure was repeated for several movable inlet positions ranging from 10 to 120 cm upstream of the pitot tube.

III.3.2 Results and Discussion

The results of this study have shown that the velocity profile changes when the position of the movable inlet is varied. When the tip of the movable inlet is close to the pitot tube the velocity profile is relatively flat. This result indicates that the turbulizer

essentially breaks up the boundary layer. As the distance between the pitot tube and the inlet tip is increased the velocity profile becomes more peaked, indicating that the boundary layer starts to reform downstream of the turbulizer. Figure 6 shows typical velocity profiles observed in the laminar flow regime at several movable inlet positions.

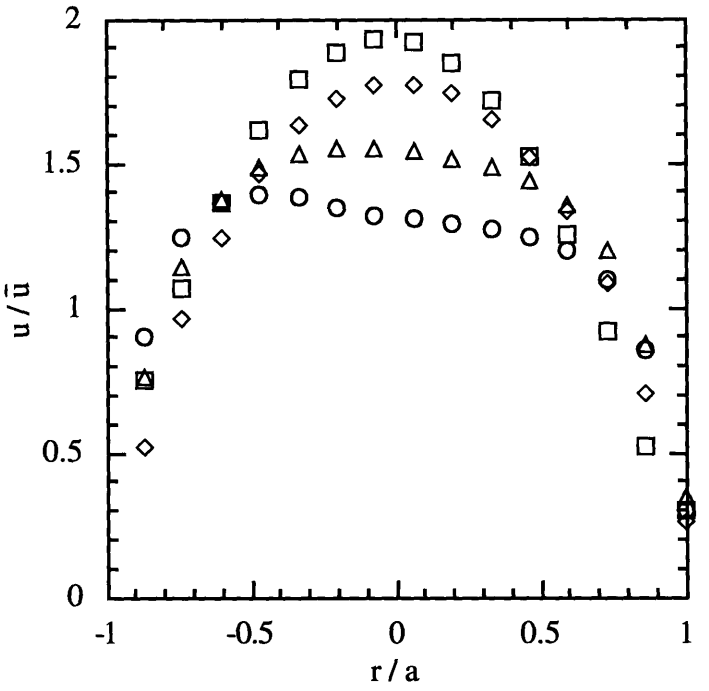

Figure 6. Velocity profiles observed in the laminar flow regime (P = 70 torr, $\bar{u}$ = 1000 cm s^{-1}, Re = 1200) at various distances between the pitot tube and the turbulizer: O - z = 15 cm; Δ - z = 30 cm; ◇ - z = 60 cm; □ - z = 120 cm.

The velocity profiles observed when the movable inlet was close (z < 50 cm) were often skewed. The side to which to the profile was skewed could be varied by rotating the

turbulizer. At large distances between the tip of the movable inlet and the pitot tube, rotation of the turbulizer produced little effect on the observed profile.

Within the turbulent flow regime, the observed velocity profiles were much flatter than those found in laminar flow. Figure 7 contains velocity profiles typical of those found in turbulent flow. Rotating the turbulizer had the same profile skewing effect that was observed in the laminar flow regime.

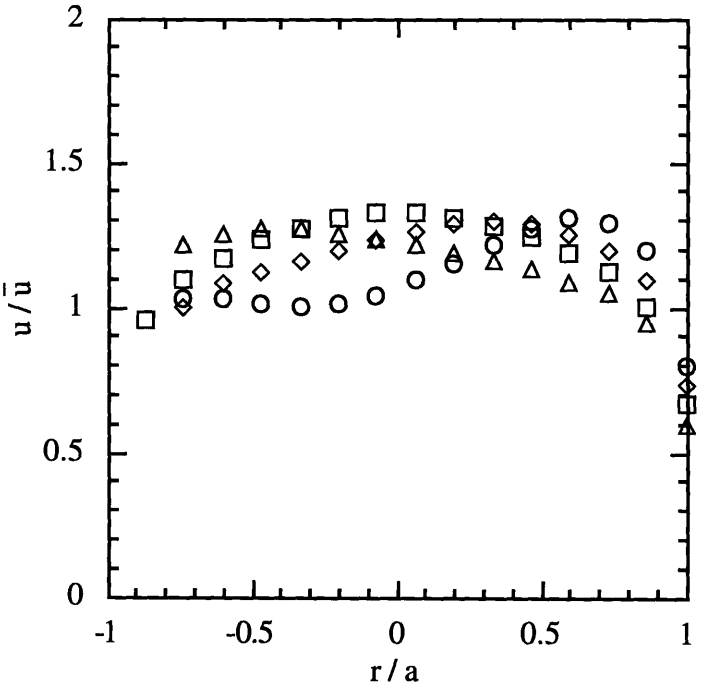

Figure 7. Velocity profiles observed in the turbulent flow regime (P = 300 torr, $\bar{u}$ = 1000 cm/s, Re = 5000) at various distances between the pitot tube and the turbulizer: O - z = 15 cm; Δ - z = 30 cm; ◇ - z = 60 cm; □ - z = 120 cm.

The dependence of the centerline velocity, u_{max}, on *Re* is depicted in figure 8. At the lowest *Re* of this study, the centerline velocity essentially reaches the fully developed value, $2\bar{u}$, at a distance less than 60 cm downstream of the turbulizer. As *Re* is increased, while still in the laminar flow regime, a greater distance is needed to establish the fully developed profile. As a result, the centerline velocity never reaches $2\bar{u}$. Within the transitional regime ($2000 < Re < 3000$), the centerline velocity decreases drastically with increasing *Re*. For $Re > 3000$ the centerline velocity slowly decreases with increasing *Re*. The curve in figure 8 represents the fully developed centerline velocity predicted by equations 17 and 18 in chapter II. The agreement between the predicted values and the experimentally observed values are excellent for $Re > 3000$.

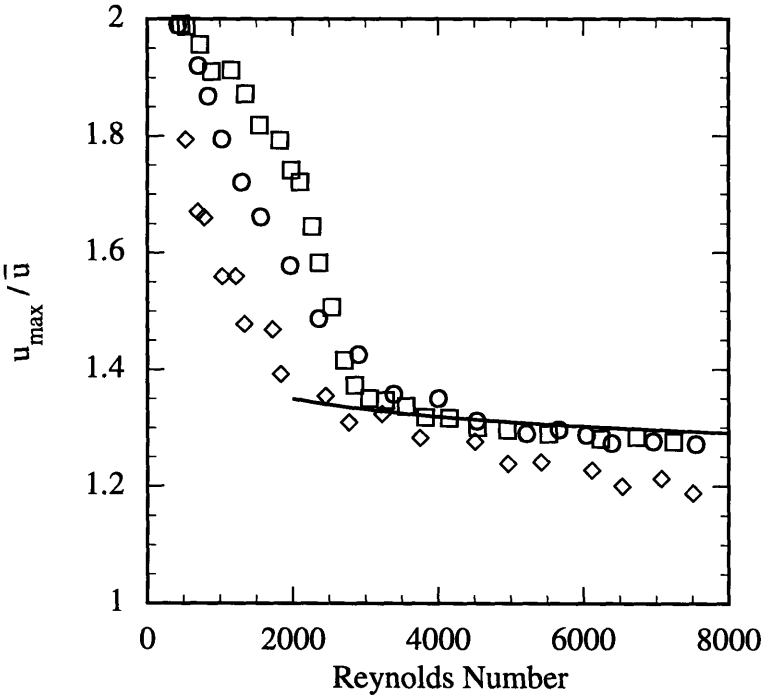

Figure 8. Relative centerline velocity ($u_{max}/\bar{u}$) as a function of Re for three different distances between the turbulizer and the pitot tube: ◇ - 30 cm; O - 60 cm; □ - 110 cm. The solid line represents the centerline velocity predicted using equation 17 and 18 from chapter II.

The evolution of the velocity profile as the movable inlet is withdrawn can be seen in figure 9 which contains centerline velocity as a function of distance between the tip of the movable inlet and the pitot tube.

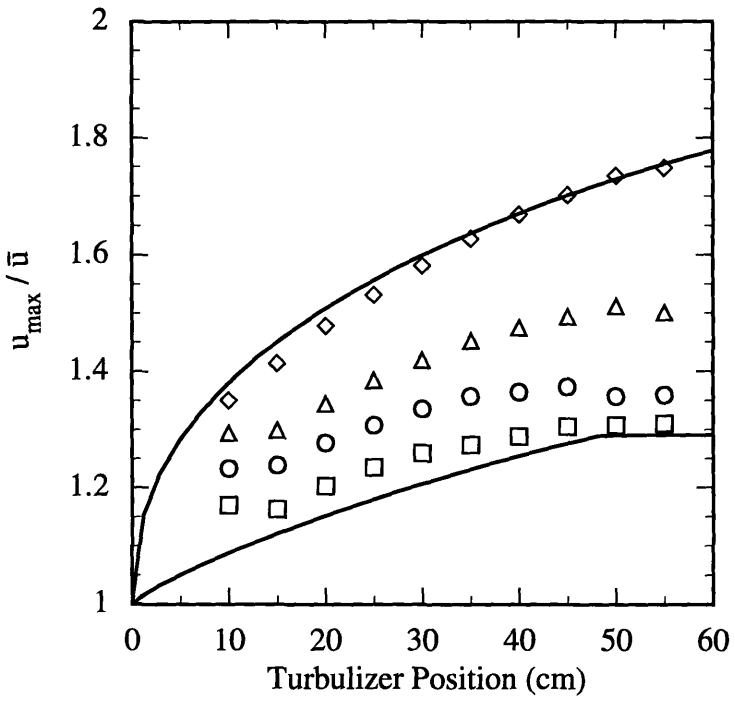

Figure 9. Variation of the centerline velocity as a function of distance between the turbulizer and the pitot tube. Measurements were performed with the average velocity roughly equal to 2000 cm s^{-1}. The symbols represent different sets of pressure and Reynolds number: ◇- P = 42 torr, Re = 1477; △ - P = 85 torr, Re = 2867; O - P = 140 torr, Re = 4757; □ - P = 232 torr, Re = 8035. The upper curve represents the centerline velocity predicted for P = 42 torr and Re = 1477 using equation 15 and 16 from chapter II with the boundary layer development determined using the method of *Cambell and Slattery* [1963]. The lower curve represents the centerline velocity predicted for P = 232 torr and Re = 8035 using equations 21 and 23 from chapter II.

Within the laminar flow regime, the dependence of $u(r=0)$ on the distance downstream of the turbulizer is well described by the model of *Cambell and Slattery* [1963]. This result indicates that the turbulizer breaks down the boundary layer in the laminar flow regime and that the developing laminar velocity profile used for the modeling studies is a good estimate of the actual velocity profile. Within the turbulent flow regime, the velocity profile is essentially fully developed after 50 cm. The evolution of the centerline velocity was well described by equation 21 in chapter II with the boundary layer thickness given by equation 23 in chapter II.

Figure 10 shows a comparison of two velocity profiles obtained in the laminar and turbulent flow regimes with the movable inlet pulled as far back as possible (120 cm between the turbulizer tip and the pitot tube). Also depicted in figure 10 are the theoretically predicted fully developed velocity profiles (see chapter II). The agreement between the observed and predicted velocity profiles is excellent in both laminar and turbulent flow. In the transitional regime ($2000 < Re < 3000$), the velocity profiles were more peaked than those observed in turbulent flow conditions and less peaked than those observed in laminar flow conditions.

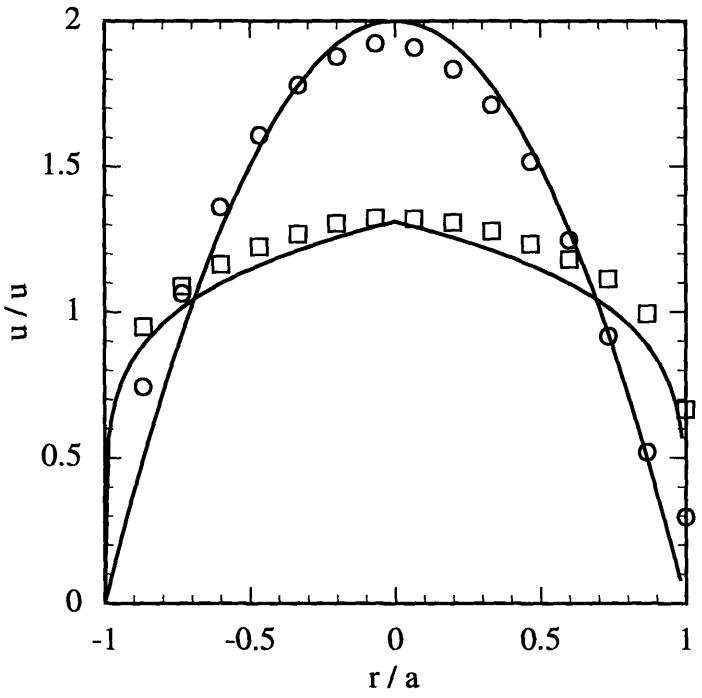

Figure 10. Comparison of velocity profiles observed in the laminar and turbulent flow regimes with 120 cm between the turbulizer and the pitot tube and $\bar{u}$ = 1000 cm s^{-1}: O - P = 70 torr, Re = 1200; □ - P = 300 torr, Re = 5000. The upper curves represent the fully developed velocity profiles for laminar flow calculated using equation 2 from chapter II. The lower curve represents the fully developed velocity profile for turbulent flow calculated using equations 3, 17, 18 from chapter II.

III.3.3 Conclusions

The results of the velocity profile measurements indicate that the boundary layer is broken down by the turbulizer. As a result, developing flow conditions will be present in most flow conditions. In laminar and turbulent flow, the evolution of the velocity profile is well described by the models presented in chapter II. As expected, within the transitional

regime ($2000 < Re < 3000$), the velocity profiles are more peaked than those predicted using the turbulent profiles described in chapter II.

III.4 Wall Loss Studies

Wall reactions are a leading interference in the determination of gas phase reaction rate constants. In low pressure flow systems, wall reactions often limit the temperature range a flow tube study can access. Results from the modeling studies described in chapter II predict that operating at higher pressures will reduce reactant-wall interactions. In this section we describe an experimental study designed to measure the reactant-wall interactions in a flow tube.

III.4.1 Experimental Details

Figure 11 contains a schematic of the apparatus used for the wall loss experiments. The flow tube was constructed from of a Pyrex tube (100 cm long, 2.2 cm i.d.) connected to a six-way cross that served as the mounting assembly for the optical detection system. Argon from a liquid argon tank was used as the main carrier gas (Airco, 99.999%). The flow tube gas was pumped by an Edwards model EM2-80 vacuum pump (1500 L min^{-1}). The bulk velocity of the gas, $\bar{u}$, ranged from 500 to 2200 cm s^{-1}. All flows were monitored with calibrated Tylan mass flow meters and pressures were measured using 0-10 and 0-1000 torr MKS Baratron manometers.

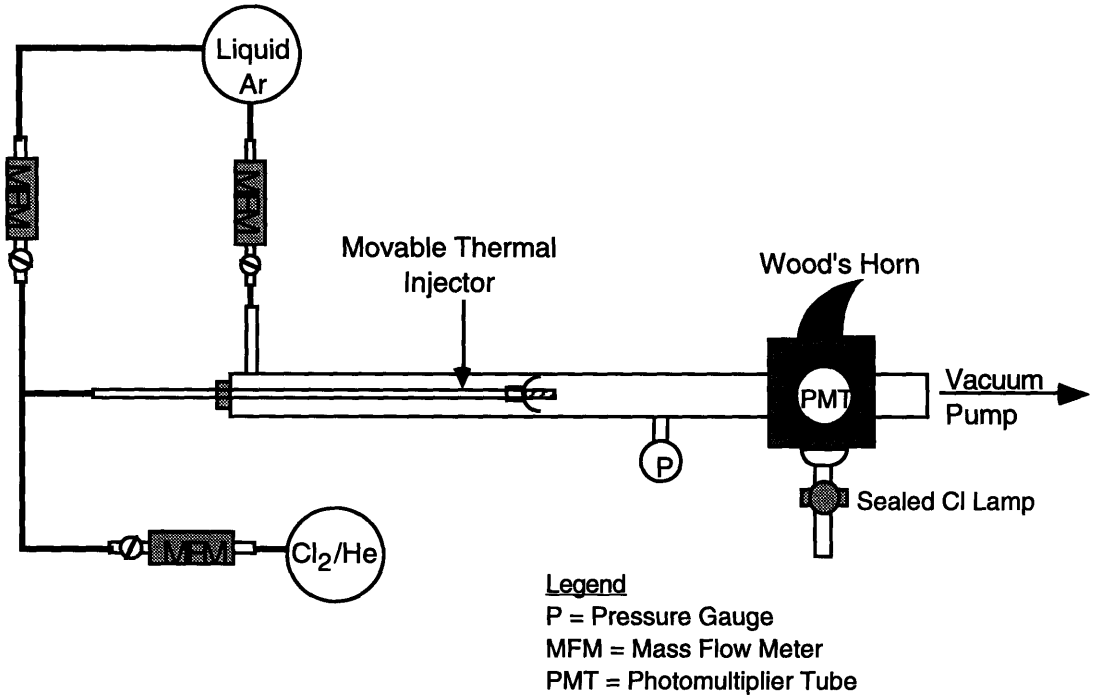

Figure 11. Schematic of the apparatus used to perform wall loss studies.

The reaction of chlorine atoms with untreated glass was used to investigate reactant-wall interactions. Chlorine atoms were continuously generated by thermally dissociating molecular chlorine. The thermal source was mounted on the tip of a 6 mm o.d. stainless steel movable injector. The source consisted of a coiled platinum wire (0.02 mm o.d., 20 cm in length when fully extended) housed inside a 6 cm long, 5 mm i.d. quartz tube. Trace quantities of Cl_2 were injected into the thermal source. When a current of approximately 300 mA was passed through the wire, a dull red glow (approximately 1000 K) was observed and chlorine atoms were detected. Similar thermal sources have been shown to generate halogen atoms free from H and O impurities [*Toohey et al.*, 1988]. A turbulizer was fixed to the end of the movable inlet. The Cl-atom concentration was monitored by resonance fluorescence at 134.7 nm. Excitation radiation was provided by a sealed Cl-atom lamp [*Schwab and Anderson*, 1982]. Fluorescing radiation was detected by a Hamamatsu 1459 photomultiplier tube (PMT) mounted perpendicular to the incident

radiation. Both the excitation radiation and the field of view of the PMT were confined to the central portion of the tube (approximately the region where $r < 0.5a$) using a series of 1 cm i.d. baffles. A $BaCl_2$ window was placed in front of the PMT to block the transmission of radiation with wavelengths shorter than about 130 nm. The intensity of the background scattered radiation, which was determined by averaging the PMT signal when only Ar was injected through the thermal source, was subtracted from the fluorescence signal. A more detailed description of the Cl-atom detection configuration can be found in chapter V.

III.4.2 Results and Discussion

For all of the studies presented here the fluorescent signal due to Cl-atoms was observed as a function of distance between the tip of the thermal injector and the middle of the optical detection region. A linear least squares fit was applied to plots of *ln* [Cl] *vs.* z, where *ln* [Cl] is the logarithm of the fluorescent signal due to Cl atoms. A first order wall loss rate constant, k_w, was obtained by multiplying the slope of the least squares fit by $-\bar{u}$.

The first set of studies was performed in an uncoated flow tube. Figure 12 shows three typical Cl-atom decays. The observed wall loss rates were found to decrease rapidly as the pressure was increased. A summary of the observed wall loss rate constants is listed in table I.

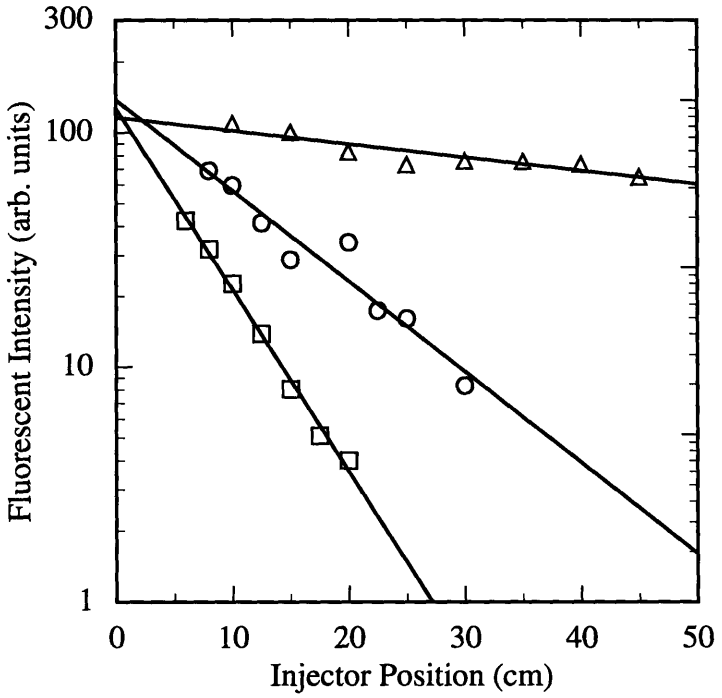

Figure 12. Plots of Cl signal vs. radical injector position in three different flow conditions: □ - P = 2.5 torr, $\bar{u}$ = 1170 cm s^{-1}, Re = 64; O - P = 6.2 torr, $\bar{u}$ = 1170 cm s^{-1}, Re = 158; Δ - P = 84 torr, $\bar{u}$ = 1180 cm s^{-1}, Re = 2151.

The wall losses observed in the uncoated tube were in reasonable agreement with the wall losses predicted by the numerical model. Figure 13 contains a comparison of our experimental results to the model predictions. The solid line in the figure represents the wall loss predicted by the model with a = 1.1 cm, $\bar{u}$ = 1100 cm s^{-1}, $D\,P$ = 140 cm^2 s^{-1} torr, and γ= 1. The model results shown in figure 13 were obtained using the core averaging scheme (i.e. concentrations were averaged in the region where $r \leq 0.5a$) in order to simulate our experimental detection method which preferentially sampled the center region of the flow. At low values of Re , the experimentally determined values of k_w are approximately 30% larger than the model predictions. The reason for this discrepancy is

most likely due to radial mixing or an over estimation of the level of background scattered radiation.

Table I. Wall loss rate constants on uncoated tube.

Pressure (torr)	$\bar{u}$ (cm s^{-1})	Re	$k_w \pm 2\sigma$ (s^{-1})
2.5	1170	64	208 ± 40
2.8	1110	66	242 ± 40
6.2	1170	158	104 ± 20
29.3	1120	716	8± 10
45	1160	1172	15± 10
84	1180	2151	11 ± 8
124	1160	3099	16 ± 10
89	1880	3566	19 ± 4
180	1150	4483	15 ± 6
356	650	4900	7 ± 2
250	922	4930	9 ± 4
152	1520	4944	13 ± 6
473	640	6500	5 ± 2
754	604	10443	4 ± 6
754	686	11871	7 ± 6

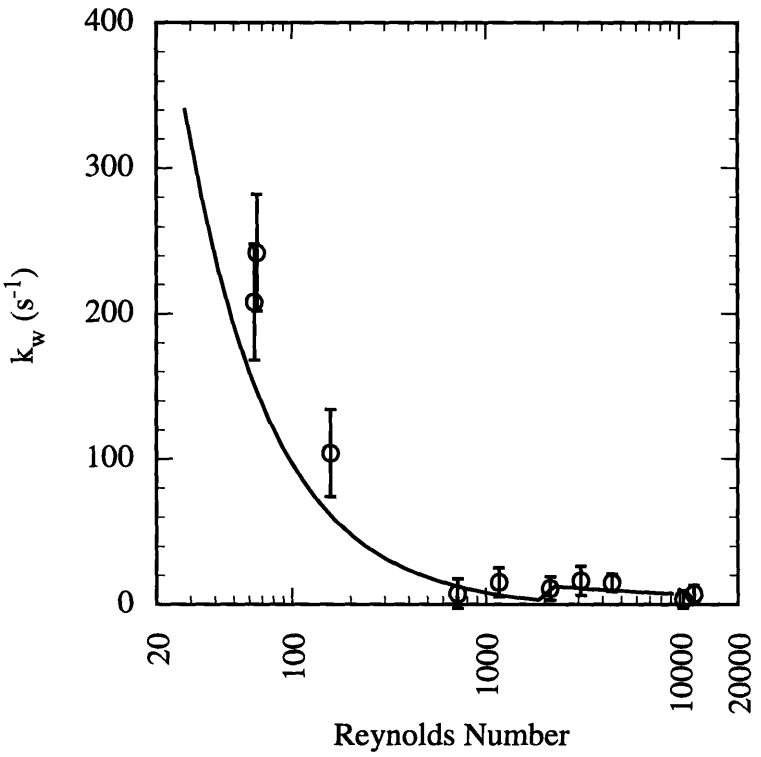

Figure 13. Observed wall loss of Cl atoms in an uncoated tube as a function of Reynolds number. The curve represents model results using a =1.1 cm, $\bar{u}$ =1100 cm s^{-1}, $D\,P$ = 140 cm^2 s^{-1} torr, γ =1.

In order to verify experimentally that the large decays observed in low pressure conditions were primarily due to wall loss and not mixing or homogenous depletion, we performed a set of experiments with a tube whose interior walls had been completely coated with Halocarbon wax. Table II contains a summary of our results. At low pressures the wall loss rate constants in the coated tube were approximately an order of magnitude less than those observed in the uncoated tube. At higher pressures (P > 10 torr) the decay rate of Cl atoms measured in the coated tube were roughly equal to that measured in the uncoated tube.

Table II. Wall loss rate constants in wax coated tube.

Pressure (torr)	$\bar{u}$ (cm s^{-1})	Re	$k_w \pm 2\sigma$ (s^{-1})
2.6	1110	63	29 ± 6
6.0	1150	148	55 ± 20
47	1080	1088	25 ± 6
94	1140	2328	6 ± 4
153	880	3080	6 ± 2
89	1510	3090	4 ± 6
63	2140	3100	12 ± 6
84	1980	3563	7 ± 6
345	670	4940	8 ± 2
250	920	4960	6 ± 2
152	1520	4970	2 ± 8
157	1600	5400	4 ± 4
508	650	7030	8 ± 2

III.4.3 Conclusions

The wall loss studies have led to several conclusions: (1) the frequency of reactant-wall interactions decreases rapidly as the pressure is increased; (2) within the turbulent flow regime, the wall losses are at least an order of magnitude smaller than those found in the low pressure laminar case; (3) coating a tube with Halocarbon wax reduces wall loss in the low pressure regime but has little effect at higher pressures; and (4) the wall loss results from the numerical model presented in the previous chapter are in reasonable agreement with experimental observations.

III.5 Tracer Pulse Studies

The model simulations described in chapter II indicated that operating in turbulent flow conditions will allow the plug flow approximation to be used at higher pressures with relatively little error (< 15%). In order to experimentally estimate the degree of deviation from plug flow conditions, we have observed tracer pulses passing down a flow tube. Although tracer pulse studies have been used extensively in the field of chemical engineering, only *Lambert et al.* [1985] have used pulses to characterize a flow tube system.

III.5.1 Experimental Details

The apparatus used for the pulsed studies is depicted in figure 14. The experiments in this study were carried out with a flow system consisting of a Pyrex tube (100 cm long, 2.4 cm i.d.) connected to a six-way cross that served as the mounting assembly for the optical detection system. Argon from a liquid argon tank was used as the main carrier gas (Airco, 99.999%). The flow tube gas was pumped by an Edwards model EM2-80 vacuum pump (1500 L min^{-1}). The bulk velocity of the gas, $\bar{u}$, was approximately 1100 cm s^{-1}. All flows were monitored with calibrated Tylan mass flow meters and pressures were measured using 0-10 and 0-1000 torr MKS Baratron manometers.

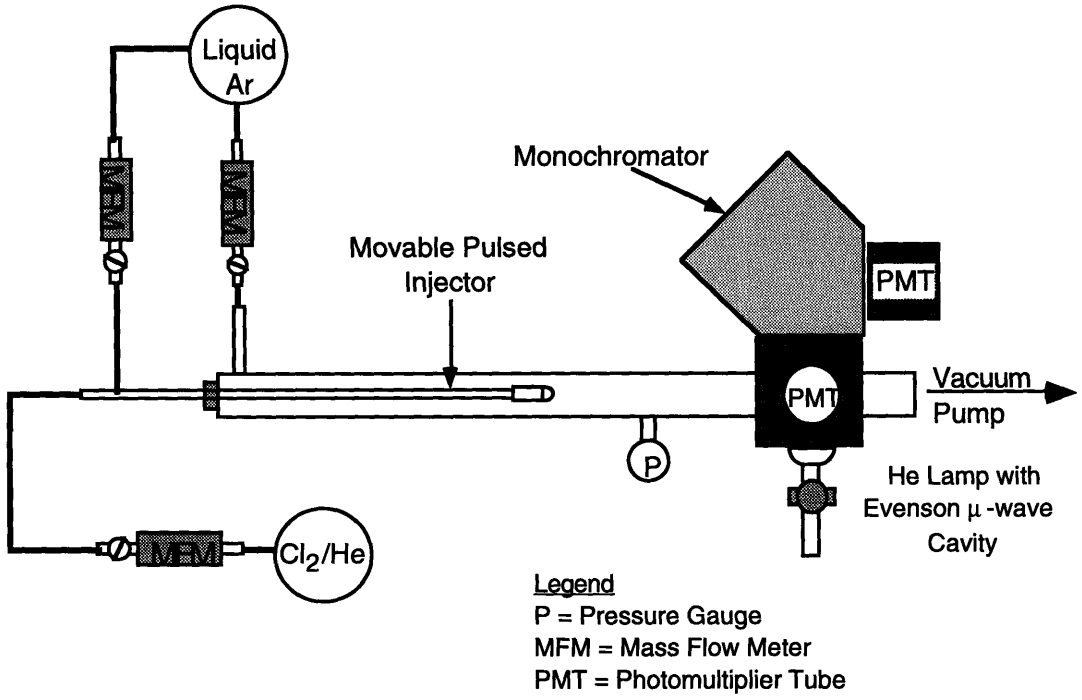

Figure 14. Schematic of apparatus used to perform flow pulsed injection studies.

Pulses were generated using a General Valve Series 9 solenoid valve with a modified orifice cap mounted on the end of a 6 mm o.d. stainless steel tube. The pulsed valve is shown in figure 15. The valve was controlled by a General Valve Iota One pulse driver. In order to promote rapid radial dispersion of the tracer, the pulses were injected through four ports located on the outer circumference of the solenoid valve. Argon gas was used to continuously sweep out the injection ports. The sweep gas was supplied via a 1.5 mm o.d. stainless steel tube that was fed through the 6 mm o.d. tube. A key feature of the pulse injector design was that the entire assembly could be moved along the axis of the flow tube, making it possible to determine the tracer concentration as a function of time for any given injector-detector distance. For several of the runs presented below the turbulizer was fixed to the end of the pulsed valve; however, the observed concentration distributions

did not differ greatly from those obtained without the turbulizer in place. This indicated that the valve itself introduced a similar level of turbulent mixing.

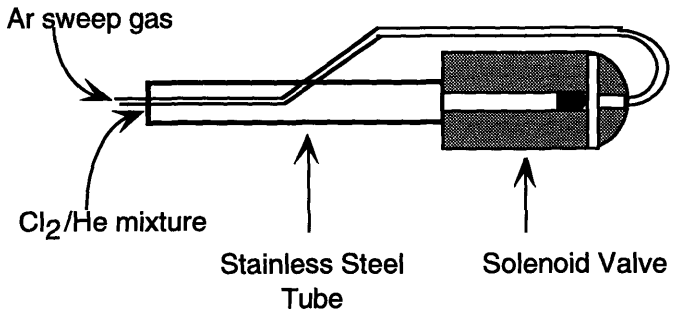

Figure 15. Schematic of pulsed valve assembly.

A 3.6% Cl_2/He mixture (Matheson Gas Co.) was used as the tracer. The pressure of the Cl_2 mixture behind the valve was approximately 1500 torr. The chlorine molecules injected into the flow were detected downstream using vacuum ultraviolet fluorescence. Excitation radiation was provided by a wide bore (1.3 cm o.d.) microwave discharge lamp operated at 70 watts and 1 torr He. The intensity of the fluorescing radiation was monitored by a Hamamatsu 1459 PMT mounted perpendicular to the incident radiation on the detection block. The same baffling of the light source and the PMT used for the wall loss studies was also employed in this study. Attenuation of the excitation light due to absorbance by the Cl_2 molecules was monitored at 135 nm by an additional PMT mounted at the exit of a monochromator (Acton Research Corp., model VM-350). The maximum attenuation of the incident radiation from the discharge lamp was found to be less than 1% for the Cl_2 pulse densities used in this work. The fluorescence intensity was linear with $[Cl_2]$ for concentrations smaller than 5×10^{14} molecule cm^{-3}; peak Cl_2 concentrations were kept below this value.

Typically, the valve was operated at a pulse rate between 1 and 3 Hz with an open time of 0.3 ms. Flow tube pressure changes due to pulsed injection of Cl_2 were not observable with the Baratron pressure gauges.

The tracer concentrations resulting from a pulse injection were monitored as a function of time at injector-detector distances starting at 10 cm and increasing up to 50 cm in 5 or 10 cm increments. Up to 200 individual pulses were signal-averaged at each position to obtain a final transient concentration distribution. The average background signal due to scattered light was subtracted from each concentration distribution.

III.5.2 Results and Discussion

Qualitative Description of Concentration Distributions

In low pressure laminar flow conditions ($P < 5$ torr, $Re < 200$) the transient concentration distributions were observed to change shape as the injector-detector distance was increased. At short distances, the concentration distributions were slightly skewed to the short times. At long distances, the concentration distributions were symmetric with a Guassian shape. The width of the distributions was observed to increase as the injector-detector distance was increased. Figure 16 contains two concentration distributions typical of those seen in low pressure laminar flow conditions. In this regime, the concentration distributions were well described by the Taylor-Aris dispersion model [*Aris*, 1956].

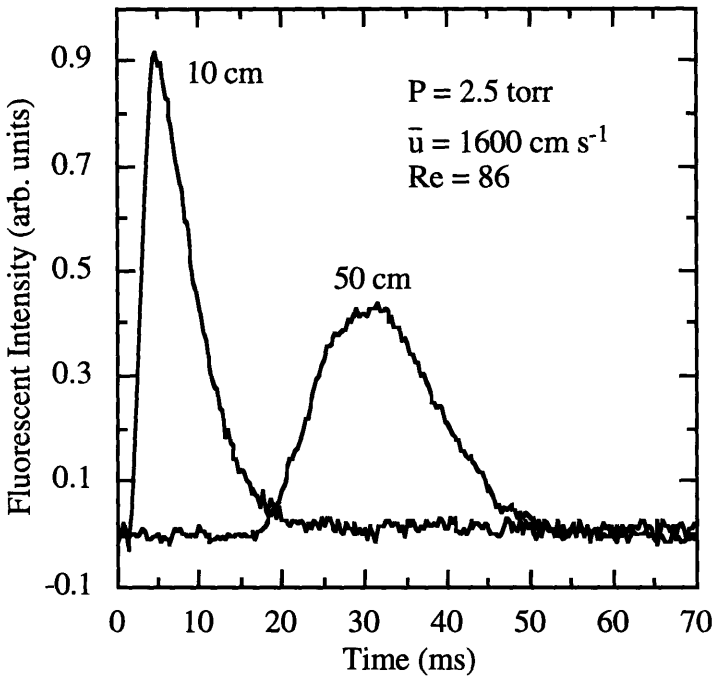

Figure 16. Plot of two concentration distributions typical of those found in the low pressure laminar flow regime.

In moderate pressure laminar flow conditions ($5 < P < 40$ torr and $200 < Re < 1000$), the transient concentration distributions were characterized by an abruptly rising front edge with a sharp peak and a slowly decaying tail. The width of the concentration distributions increased as the injector-detector distance was increased. The shape of the distributions often remained sharply skewed regardless of the injector-detector distance. Figure 17 contains two concentration distributions typical of those seen in moderate pressure laminar flow conditions.

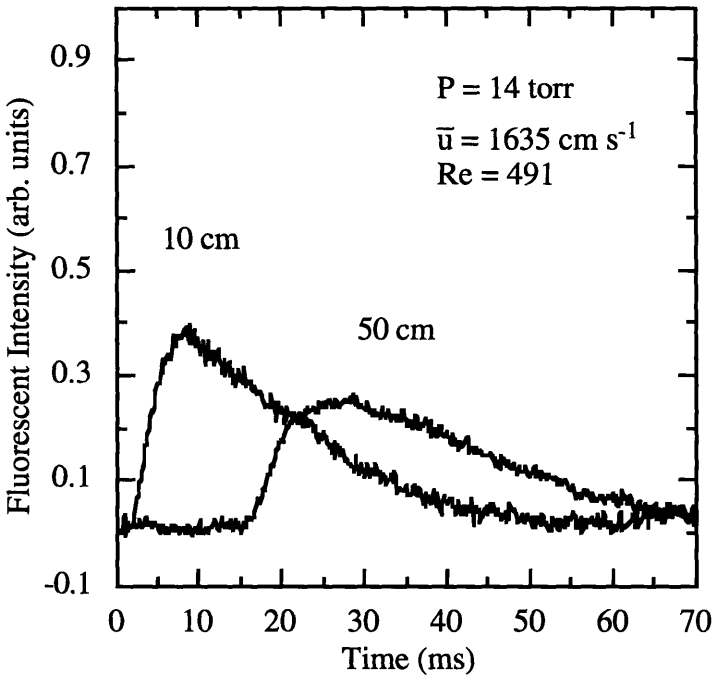

Figure 17. Plot of two concentration distributions typical of those found in the moderate pressure laminar flow regime.

For high pressure laminar flow and turbulent flow conditions ($P > 40$ torr, $Re >$ 1000), the transient concentration distributions were observed to be less dispersed and more symmetric in shape than those observed in moderate pressure laminar flow conditions. Increasing the injector-detector distance produced little effect on the shape of the concentration distributions. Figure 18 contains two concentration distributions typical of those seen when $Re > 1000$.

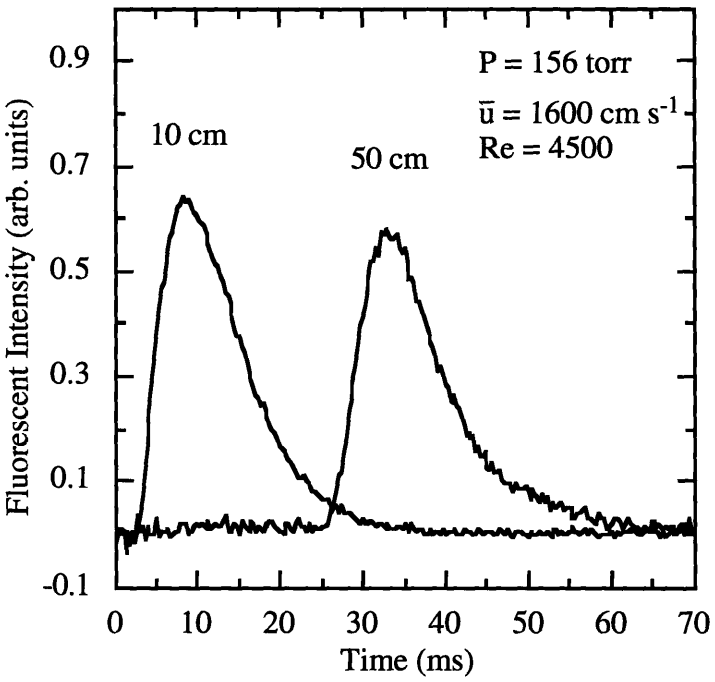

Figure 18. Plot of two concentration distributions typical of those observed for Re > 1000.

We have determined the average velocity of the concentration distributions (the pulse velocity), u_p, by plotting the arrival time of the concentration distributions as a function of the injector-detector distance, z, and fitting the points with a least-squares generated line. The arrival time was defined as the time which divides the total area beneath the observed concentration distribution in half (taking $t = 0$ as the time at which the pulse valve opens). Figure 19 contains a typical plot.

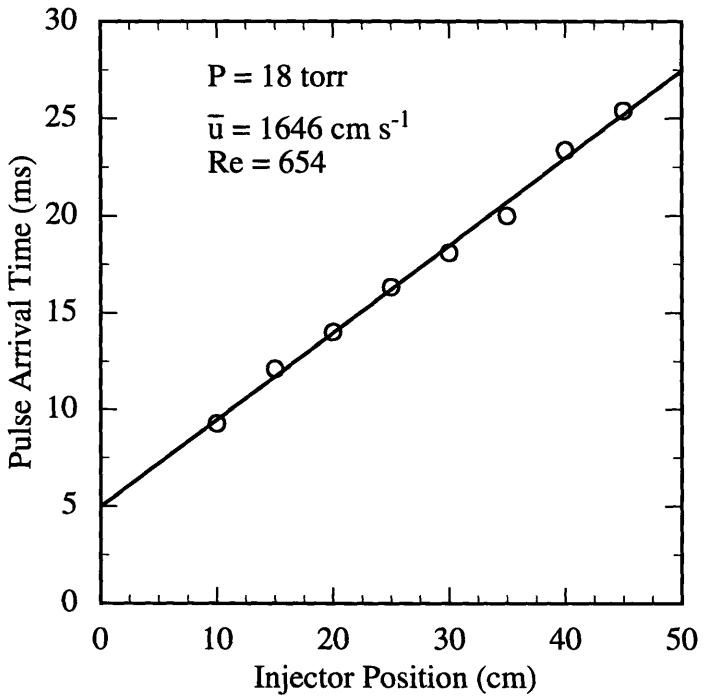

Figure 19. Typical plot of the pulse arrival time as a function of distance between the pulsed injector and the detection region.

The inverse of the slope of the linear fit is the pulse velocity. The intercept of the line represents the amount of time it takes for the pulse to be entrained into the flow. Table III contains a summary of these results.

Table III. Relative pulse velocity.

Pressure (torr)	$\bar{u}$ (cm s^{-1})	Re	$u_p / \bar{u} \pm 2\sigma$
1.8	915	36	1.02 ± 0.02
2.1	1000	46	1.04 ± 0.02
4.2	1600	140	0.96 ± 0.02
4.6	1530	150	1.12 ± 0.06
6.1	1540	201	1.25 ± 0.11
9.4	1635	330	1.16 ± 0.19
14	1635	491	1.27 ± 0.13
18	1646	654	1.36 ± 0.09
20	1625	688	1.12 ± 0.13
24	1720	893	1.24 ± 0.09
33	1656	1177	1.33 ± 0.06
68	1667	2430	1.21 ± 0.02
70	1730	2631	1.16 ± 0.08
90	1667	3244	1.18 ± 0.04
113	1667	4064	1.11 ± 0.04
146	1667	5233	1.06 ± 0.04
146	1677	5307	1.08 ± 0.02
217	1699	8010	1.08 ± 0.04
760	739	12059	1.02 ± 0.04

The relative pulse velocity ($u_p / \bar{u}$) is depicted in Figure 20 as a function of *Re*. At $Re < 200$ the relative pulse velocity is essentially equal to 1. For $Re > 200$ the relative pulse velocity increases with increasing *Re* until it reaches a maximum of 1.4 at $Re = 1000$. Within this regime, the uncertainty of the average tracer velocity is increased due to increased tracer dispersion. For $Re > 1000$ the relative pulse velocity decreases with increasing *Re*, asymptotically approaching 1.

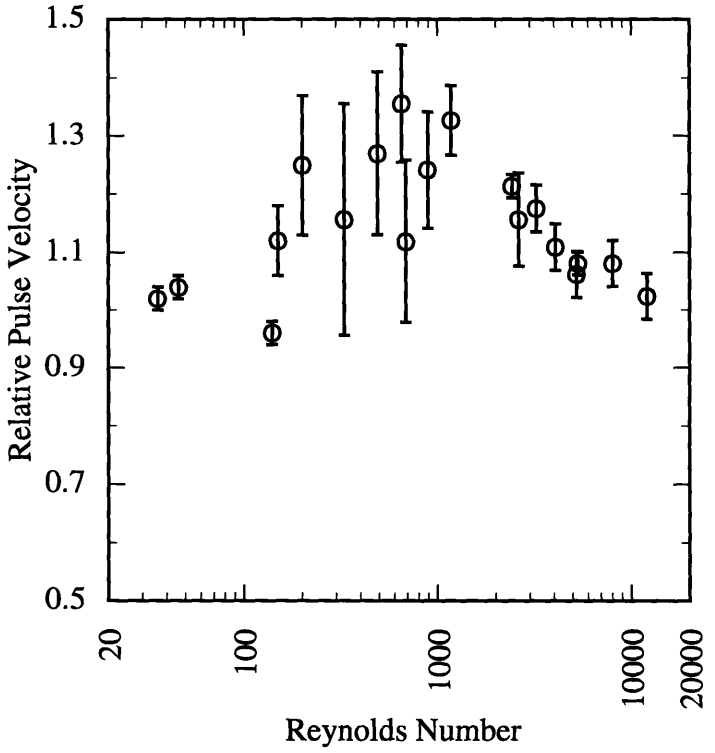

Figure 20. Relative pulse velocity (u_p / $\bar{u}$) as a function of *Re*.

The above observations can be easily explained in terms of the motion of the tracer molecules. In low pressure laminar flow conditions, transport via molecular diffusion is rapid. Because the time scale for lateral movement is much shorter than the time scale for convection, each tracer molecule visits many radial positions before entering the detection region. As a result, each tracer molecule has an average velocity near $\bar{u}$. Thus, the average velocity of the concentration distribution is approximately $\bar{u}$. The spreading of the observed distributions is largely a result of molecular diffusion in the axial direction.

In moderate pressure laminar flow conditions, transport via molecular diffusion is inhibited. Thus each tracer molecule visits a smaller range of radial positions. The peaked velocity profile of laminar flow causes tracer molecules which were injected into the center of the flow to be convected down the tube much faster than those injected near the walls. The disparity in tracer velocities causes the observed concentration distributions to become

increasingly dispersed as the injector-detector distance is increased. Under these conditions, the pulse velocity is equal to $\bar{u}$ only if the detection scheme evenly samples the entire tube cross section. Since the fluorescent detection scheme used in this study preferentially samples the central portion of the flow tube cross section, we detect tracer molecules which remain confined to the faster moving portion of the flow. Thus, the average velocities of the observed concentration distributions are larger than the bulk velocity.

When $1000 < Re < 2000$ the tracer molecules still remain confined to their original radial position, but the velocity profile is flattened due to the increased entrance length. Thus, dispersion is decreased and the average velocity of the pulse is closer to $\bar{u}$. In the turbulent regime ($Re > 2000$), the pulse velocity decreases even more due to the flattening of the velocity profile and an increase in radial transport via eddy diffusion.

Prediction of the Deviation from Plug Flow

In addition to qualitative information, pulsed tracer studies can be used to quantitatively estimate the deviation from plug flow conditions. The plug flow approximation maintains that all of the limiting reactant molecules travel down the tube with a velocity equal to $\bar{u}$. Thus in plug flow conditions, a tracer pulse injected into the flow should travel down the tube at velocity of $\bar{u}$. The error incurred when making the plug flow approximation can therefore be estimated by determing the ratio of $\bar{u}$ to the average pulse velocity. Unfortunately, in conditions where tracer spreading is substantial, this approach underestimates the deviation from plug flow. A more accurate method of estimating the deviation from plug flow conditions (which includes the effects of tracer spreading) has been derived in the appendix located at the end of this chapter. The final result of this derivation states that the concentration of a limiting reactant that would be observed in steady state pseudo-first-order conditions, $\overline{C}_A(z)$, can be predicted from an observed transient concentration distribution, $\overline{P}_A(z,t)$, using

$$\overline{C}_A(z,k^I) = \beta \int_0^\infty \overline{P}_A(z,t)\ exp\left(-k^I t\right) dt \qquad (4)$$

where β is a proportionality constant and k^I is the pseudo-first-order rate constant. Since only the relative value of the limiting reactant concentration is needed to determine the rate constant in a steady state experiment, the value of β does not affect the results and hence does not need to be determined. For this analysis, we will assume that $\beta = 1$.

The pulse attenuation analysis was performed in the following manner: The pseudo-first-order rate constant, k^I, was set at a value ranging from 0 s^{-1} to 200 s^{-1}. Each transient concentration distribution, $\overline{P}_A$, was then attenuated by a factor of $\exp(-k^I t)$. The value $\overline{C}_A$ was calculated by integrating the area beneath the attenuated concentration distribution. A line was then fit to a plot of $\ln\overline{C}_A(z)$ *vs.* z and the value of k^I_{obs} was taken from the slope of the fit multiplied by $-\bar{u}$. An example of the determination of k^I_{obs} is shown in figure 21 for pulses collected under the following conditions: P = 68 torr, $\bar{u}$ = 1667 cm s^{-1}, Re = 2430. The values of k^I_{obs} were plotted as a function of k^I. The slope of the line represents the ratio of the plug flow rate constant to the actual rate constant (k_{obs} / k). This process is demonstrated in figure 22 for the case of P = 68 torr, $\bar{u}$ = 1667 cm s^{-1}, Re = 2430. A summary of the pulse attenuation results are shown in table IV and figure 23.

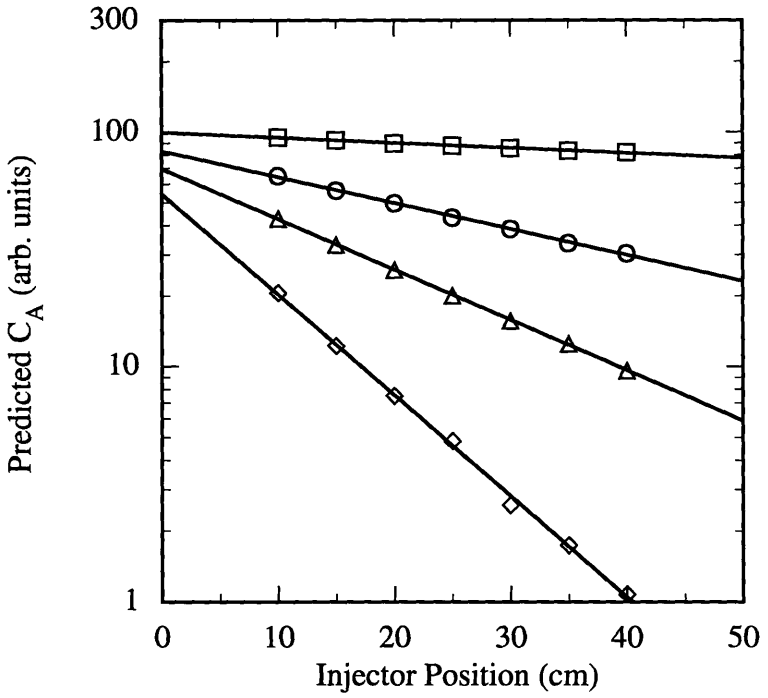

Figure 21. Plots of the $\overline{C}_A$ vs. injector. Values of $\overline{C}_A$ predicted using equation 4 with a set of pulses collected at P = 68 torr, $\bar{u}$ = 1667, Re = 2430. Symbols represent different values of k^I: □ - k^I = 10 s^{-1}; ○ - k^I = 50 s^{-1}; △ - k^I = 100 s^{-1}; ◇ - k^I = 200 s^{-1}.

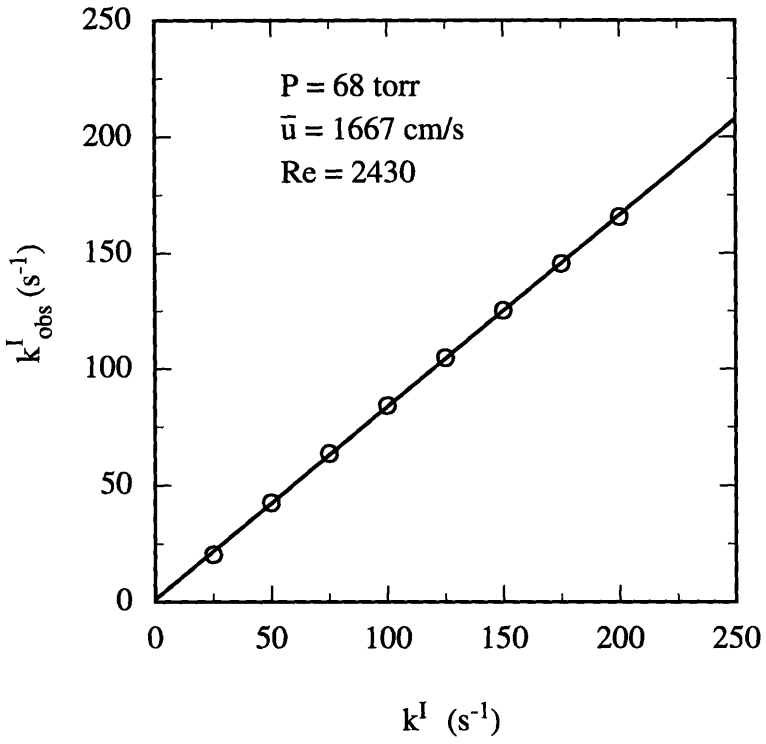

Figure 22. Typical plot for determining k_{obs} / k from the pulse attenuation analysis data.

Table IV. Values of k_{obs} / k from the pulse analysis.

Pressure (torr)	velocity (cm/s)	Re	$k_{obs} / k \pm 2\sigma$
1.8	915	36	0.865 ± 0.012
2.1	1000	46	0.828 ± 0.020
2.8	1250	76	0.812 ± 0.022
4.2	1600	140	0.767 ± 0.030
4.6	1530	150	0.724 ± 0.020
6.1	1540	201	0.635 ± 0.016
9.4	1635	330	0.678 ± 0.020
14	1635	491	0.651 ± 0.012
18	1646	654	0.735 ± 0.003
20	1625	688	0.703 ± 0.012
24	1720	893	0.739 ± 0.008
33	1656	1177	0.721 ± 0.007
68	1667	2430	0.824 ± 0.005
69	1656	2438	0.860 ± 0.008
70	1730	2631	0.828 ± 0.007
90	1667	3244	0.788 ± 0.010
113	1667	4064	0.843 ± 0.010
146	1667	5233	0.888 ± 0.006
146	1677	5307	0.907 ± 0.005
205	1667	7385	0.883 ± 0.001
760	739	12059	0.928 ± 0.005

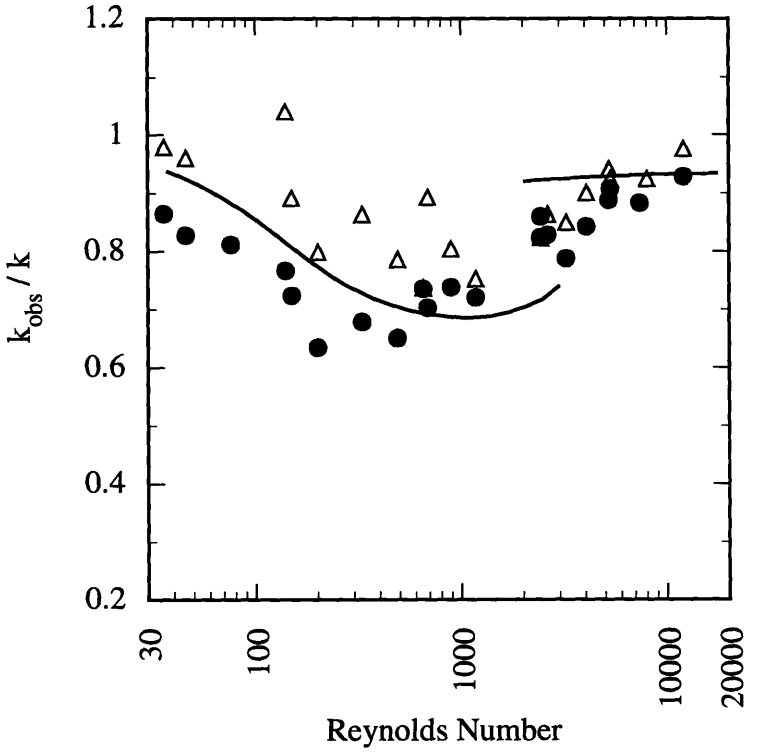

Figure 23. Values of k_{obs} / k predicted from pulse studies. Dots represent values predicted using the pulse attenuation analysis and the triangles represent values predicted considering only the average pulse velocity. The curve represents the values predicted using the numerical model described in chapter II.

As can be seen from figure 23, the deviation from plug flow increases with increasing pressure until $Re = 500$. For $Re > 500$ the deviation decreases with increasing pressure. Also plotted in figure 23 is the value of $\bar{u} / u_p$ (the inverse of the values displayed in figure 20). Under conditions where there is no tracer spreading, the deviation from plug flow and the inverse of the relative tracer velocity should be identical. Notice that at $Re < 1000$ there is a large difference between the deviation predicted by the pulse attenuation analysis and the values of $\bar{u} / u_p$. This is due to the large amount of tracer spreading that occurs under

these conditions. For $Re > 1000$ the inverse of the relative pulse velocity and the predicted deviations are very similar, indicating that spreading is minimized.

Also displayed in figure 23 is the deviation from plug flow calculated by the numerical model described in chapter II. The following conditions were used for the calculation: Cl_2 limiting reactant, $\bar{u} = 1630$ cm s^{-1}, $D_A P = 90$ cm^2 s^{-1} torr, $a = 1.2$ cm, $\gamma = 0$, Ar carrier gas, developing flow conditions. The value of the molecular diffusion coefficient of Cl_2 in Ar was calculated using the method recommended by *Reid et al* [1987]. In general, the results from both analyses are in good agreement: the deviations from plug flow predicted by the model and by the pulse analysis agree to within approximately 10% in all flow conditions. In the laminar flow regime, the deviation predicted by the pulsed analysis is approximately 5–10% greater than the model prediction. In the transitional regime ($2000 < Re < 3000$), the pulsed analysis data lies between the model deviations predicted using laminar and turbulent flow parameters. In the turbulent flow regime, the pulsed analysis predictions are slightly larger (~5%) than the model predictions.

III.5.3 Conclusions

The pulsed tracer studies have been used to estimate the error incurred when the plug flow approximation is made. Results from these studies have indicated that the magnitude of the error in turbulent flow conditions is similar to the magnitude within the low pressure laminar regime (< 15%). The deviations from plug flow predicted by the pulsed tracer studies are in good agreement with those predicted by the numerical model described in chapter II.

III.6 Chapter Conclusions

The results from the fluid dynamic experiments described in this chapter have supported the hypothesis that operating a standard flow tube system in the turbulent flow regime will allow rate constants to be determined at high pressures and low temperatures. Flow visualization studies have shown that reactants are rapidly mixed in the turbulent flow regime if a simple device which promotes turbulent mixing is placed on the tip of the movable inlet. Pitot-tube measurements have shown that velocity profiles are relatively flat in turbulent flow conditions. Results from wall loss studies have shown that reactant-wall interactions are drastically reduced in turbulent flow conditions. Pulsed tracer studies have indicated that in turbulent flow the plug flow approximation should be reasonably accurate. The results from all of these studies have led to conclusion that a turbulent flow tube technique should be capable of measuring rate constants using the plug flow approximation without incurring systematic errors greater than 15%. In addition, each study reported in this chapter has shown that the numerical model presented in chapter II accurately describes the fluid dynamical state of the flow tube. Thus, correction factors can potentially be numerically generated to compensate for non-plug flow conditions and thereby increase the accuracy of a turbulent flow tube method.

III.7 Appendix: Derivation of Equation 4

Lambert et al. [1985] have derived a mathematical relationship between the transient concentration of a tracer pulse and the concentration of the limiting reactant under steady state reactive conditions. Unfortunately, their paper contains several mathematical errors which make their final result incorrect. Consequently, we have performed our own mathematical derivation which shows how the transient input of tracers can be used to diagnose the effects of reactant transport .

Consider a flow tube reactor in which the limiting reactant is injected at an upstream point in a continuous fashion. Using the notation of the previous chapter, the continuity equation for a species in an isothermal, constant density reactor with a first order chemical depletion is given by

$$\nabla\left(E_A \nabla C_A\right) - \nabla(u C_A) - k^I C_A = 0 \tag{5}$$

where E_A and C_A are respectively the diffusivity and the concentration of the limiting reactant, u is the convective velocity and k^I is the pseudo-first-order rate constant. The boundary conditions for equation 5 are

$$\left(\frac{\partial C_A}{\partial r}\right)_{r=a} = -\left(\frac{\gamma_A \bar{\omega}_A}{4 E_A} C_A\right)_{r=a} \tag{6}$$

$$(C_A)_{z=0} = \chi(r,\varphi) \tag{7}$$

where a is the internal radius of the flow tube, γ_A is the reactive collision efficiency, ω_A is the average thermal velocity of the limiting reactant, and χ is the concentration distribution at $z = 0$.

Imagine that the steady flow of the limiting reactant is replaced by the injection of a transient pulse and that the first order chemical removal mechanism is no longer present (i.e. $k^I = 0$). Due to the time dependence of this scenario the steady state continuity equation needs to replaced by the corresponding time dependent equation. For clarity, the time dependent concentration of the limiting reactant will be denoted as P_A. The time dependent equations are

$$\frac{\partial P_A}{\partial t} = \nabla\left(E_A \nabla P_A\right) - \nabla(u P_A) \tag{8}$$

$$\left(\frac{\partial P_A}{\partial r}\right)_{r=a} = -\left(\frac{\gamma_A \, \bar{\omega}_A}{4 \, E_A} P_A\right)_{r=a} \tag{9}$$

$$(P_A)_{z=0} = \chi(r,\varphi) \, \psi(t) \tag{10}$$

were ψ is the time dependence of the pulsed input at $z = 0$. Note that equation 10 asserts that the reactant pulse has the same radial concentration distribution as is found for the steady state case except the amplitude is a function of time. For the time dependent case, there are two additional boundary conditions: $P_A = 0$ at $t = 0$ and $P_A = 0$ at $t = \infty$. The Laplace transform of equation 8 is given by

$$\int_0^\infty e^{-st} \frac{\partial P_A}{\partial t} \, dt = \int_0^\infty e^{-st} \, \nabla\left(D \nabla P_A\right) dt - \int_0^\infty e^{-st} \, \nabla(u P_A) \, dt \tag{11}$$

When the integrals are evaluated and the boundary conditions are applied, equation 11 becomes

$$\nabla\left(E_A \nabla G_A\right) - \nabla(u \, G_A) - s G_A = 0 \tag{12}$$

where G_A is the Laplace transform of P_A

$$G_A = \int_0^\infty e^{-st} P_A \, dt \tag{13}$$

The boundary conditions of equation 12 are found by taking the Laplace transforms of equations 9 and 10

$$\left(\frac{\partial G_A}{\partial r}\right)_{r=a} = -\left(\frac{\gamma_A \, \overline{\omega}_A}{4 \, E_A} G_A\right)_{r=a} \tag{14}$$

$$(G_A)_{z=0} = \beta \, \chi(r,\varphi) \tag{15}$$

where β is the Laplace transform of ψ.

By comparing equations 5-7 to equations 12,14,15 it is obvious that $C_A = \beta \, G_A$ when $s = k^I$. Thus

$$C_A(r,\varphi,z,k^I) = \beta \int_0^\infty P_A(r,\varphi,z,t) \, exp\left(-k^I t\right) dt \tag{16}$$

If a detection scheme is used which samples over a finite range of positions centered at an axial position z, it can be easily shown by integrating both sides of equation 16 over the detection region that

$$\overline{C}_A(z,k^I) = \beta \int_0^\infty \overline{P}_A(z,t) \, exp\left(-k^I t\right) dt \tag{4}$$

where $\overline{C}_A(z)$ and $\overline{P}_A(z,t)$ are the observed average concentrations.

References for Chapter III

Aris, R., On the dispersion of a solute in a fluid flowing through a tube, *Proc. R. Soc. London, A235,* 67, 1956.

Beenakker, C. I. M., A cavity for microwave-induced plasmas operated in helium and argon at atmospheric pressure,*Spectrochimica Acta, 31B,* 483, 1976.

Breyer, D.W., and R. C. Pankhurst, *Pressure-probe Methods for Determining Wind Speed and Flow Direction*, Her Majesty's Stationery Office, London, 1971.

Cambell, W. D., and J.C. Slattery, Flow in the entrance of a tube, *Trans. ASME, Ser. E, 85,* 41, 1963.

Emrich, R. J. (Ed.), *Methods of Experimental Physics, 18A,* Academic Press, New York, 1981.

Lambert, M., C. M. Sadowski, and T. Carrington, Uses of the transit time distribution in kinetic flow systems, *Int. J. Chem. Kinet., 17,* 685, 1985.

Reid, R. C., J. M. Prausnitz and T. K. Sherwood, *The Properties of Gases and Liquids, 4th ed.,* McGraw-Hill, New York, 1987.

Schwab, J. J., and J. G. Anderson, Oscillatior strengths of Cl(I) in the vacuum ultraviolet, *J. Quant. Spectorsc. Radiat. Transfer., 27,* 445, 1982.

Taylor, G., Dispersion of soluble matter in solvent flowing slowly through a tube, *Proc. R. Soc. London. Ser. A, 219,* 186, 1952.

Toohey, D. W., Wm. H. Brune, and J. G. Anderson, Rate constant for the reaction Br + $O_3 \rightarrow BrO + O_2$ from 248 to 418 K kinetics and mechanism, *Int. J. Chem. Kinet., 20,* 74, 1988.

Worsnop, D. R., M. S. Zahniser, C. E. Kolb, J. A. Gardner, L. R. Watson, J. M. VanDoren, J. T. Jayne, and P. Davidovits, Temperature dependence of mass accommodation of SO_2 and H_2O_2 on aqueous Surfaces, *J. Phys. Chem., 93,* 1159, 1989.

Chapter IV: Kinetic Studies of H-atom Reactions

IV.1 Introduction

In this chapter we describe the implementation of the turbulent flow tube technique to measure the rate constants of two H-atom reactions:

$$H + O_3 \rightarrow OH + O_2 \quad (1)$$

$$H + Cl_2 \rightarrow HCl + Cl \quad (2)$$

These particular reactions were chosen because they have well established rate constants and are relatively simple to experimentally characterize.

IV.2 Experimental Details

IV.2.1 Flow Tube Construction

The apparatus used for measuring the rate constant for the reactions of $H + O_3$ and $H + Cl_2$ is shown in figure 1. Experiments were carried out with a flow system consisting of a Pyrex tube (100 cm long, 2.4 cm i.d.) connected to a six-way cross that served as the mounting assembly for the optical detection system. Argon from a liquid argon tank was used as the main carrier gas (Airco, 99.999%). The flow tube gas was pumped by an Edwards model EM2-80 vacuum pump (1500 L min^{-1}). All flows were monitored with calibrated Tylan mass flow meters and pressures were measured using 0-10 and 0-1000 torr MKS Baratron manometers. In order to inhibit heterogeneous reactant loss, the inner wall of the flow tube was coated with Halocarbon wax. The average velocity of the carrier gas ranged from 800 to 2200 cm s^{-1} and the pressure ranged from 1.5 to 300 torr.

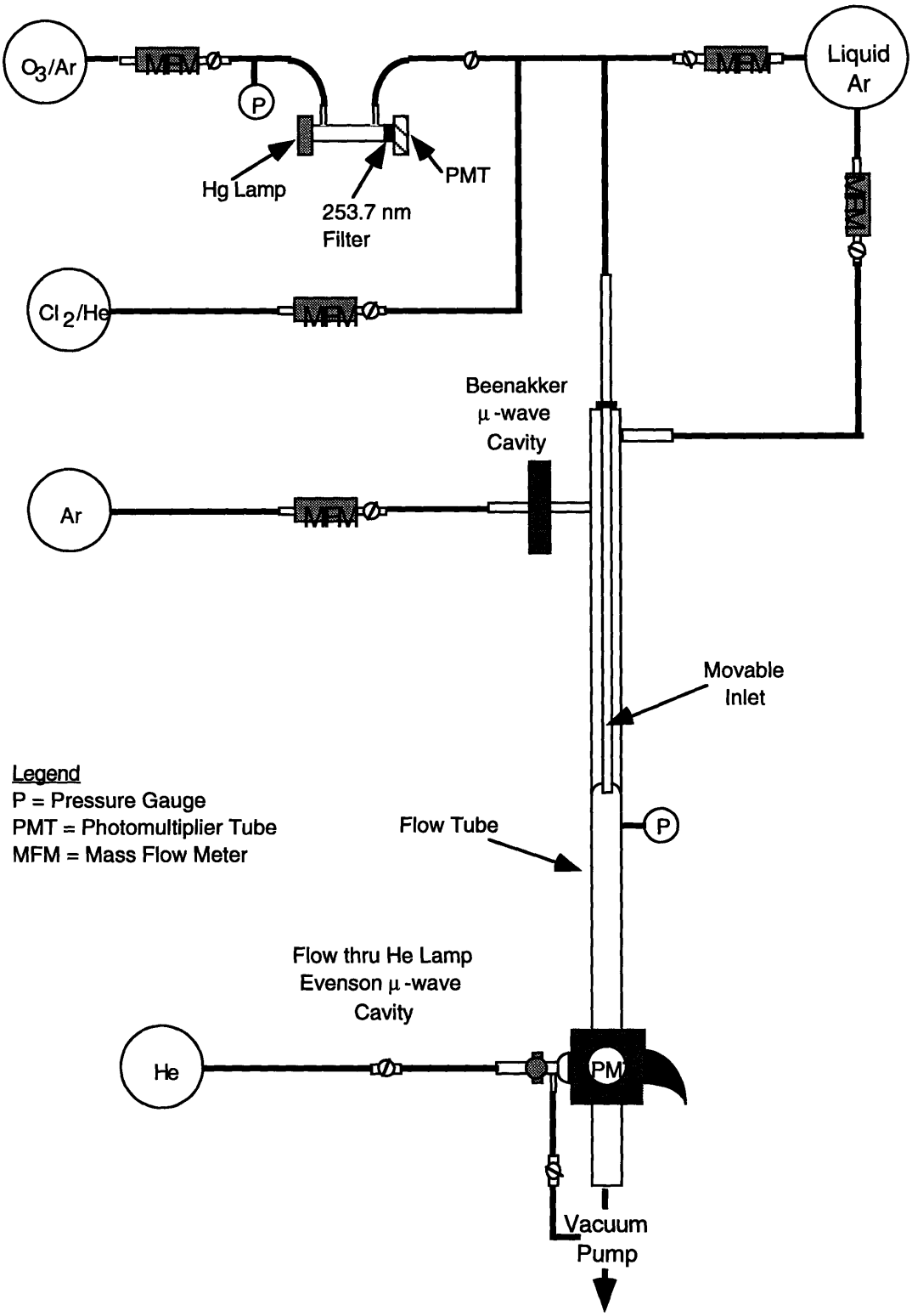

Figure 1. Schematic of the apparatus used to determine H-atom reaction rate constants.

All H-atom experiments were conducted under pseudo-first-order conditions with the excess reagent (O_3 or Cl_2) added through a movable injector (a 6 mm o.d. Pyrex glass tube). An additional flow of Ar was also passed through the movable inlet. The total flow through the movable injector was kept below 10% of the main carrier gas flow. A thin coat of Halocarbon grease was applied to the outer surface of the movable inlet to allow for easy repositioning and to minimize removal of radical species on its surface. A turbulizer was fixed to the end of the movable inlet for all kinetics experiments unless otherwise noted.

IV.2.2 Reactant Preparation and Detection

H-atoms

Ground-state H-atoms were produced by flowing argon (Airco, 99.998%) through a 2.45 GHz high-pressure microwave discharge (Beenakker type) operated at 25 watts. The H-atoms originated from trace impurities in the argon (H_2O and hydrocarbons). The microwave cavity and the discharge tube were cooled by a flow of compressed air.

The detection scheme used for the hydrogen atom kinetics studies is depicted in figure 2. Hydrogen atoms were detected by resonance fluorescence at the $2p\ ^2P - 1s\ ^2S$ Lyman-α line (121.6 nm). The excitation radiation was supplied by a wide bore (1.3 cm) microwave discharge lamp operated at 40 watts. The fluorescing radiation was detected with a Hamamatsu R1459P solar blind photomultiplier tube (PMT). The lamp and microwave cavity were cooled by a flow of compressed air. The maximum fluorescence signal was obtained by flowing UHP helium through the lamp at a total pressure of 1.5 torr. Adding trace amounts of H_2 to the helium flow did not increase the fluorescent signal. A purge of O_2 gas was passed between the resonance lamp and the detection region in order attenuate radiation which could promote fluorescence of other species (especially oxygen atoms). The baffling of the light source and the PMT was the same that was used for the wall loss studies reported in chapter III. A purge of Ar was passed between the

PMT and the detection region. The PMT signal was linear with H-atom concentration for [H] < 10^{12} molecule cm^{-3}; [H] was measured by titration with NO_2 (see *Wagner et al.* [1976] for details on the use of titration reactions). In all the kinetics experiments reported here, the flow through the discharge was less than 1% of the total carrier gas flow and [H] was kept below 2×10^{11} molecule cm^{-3}.

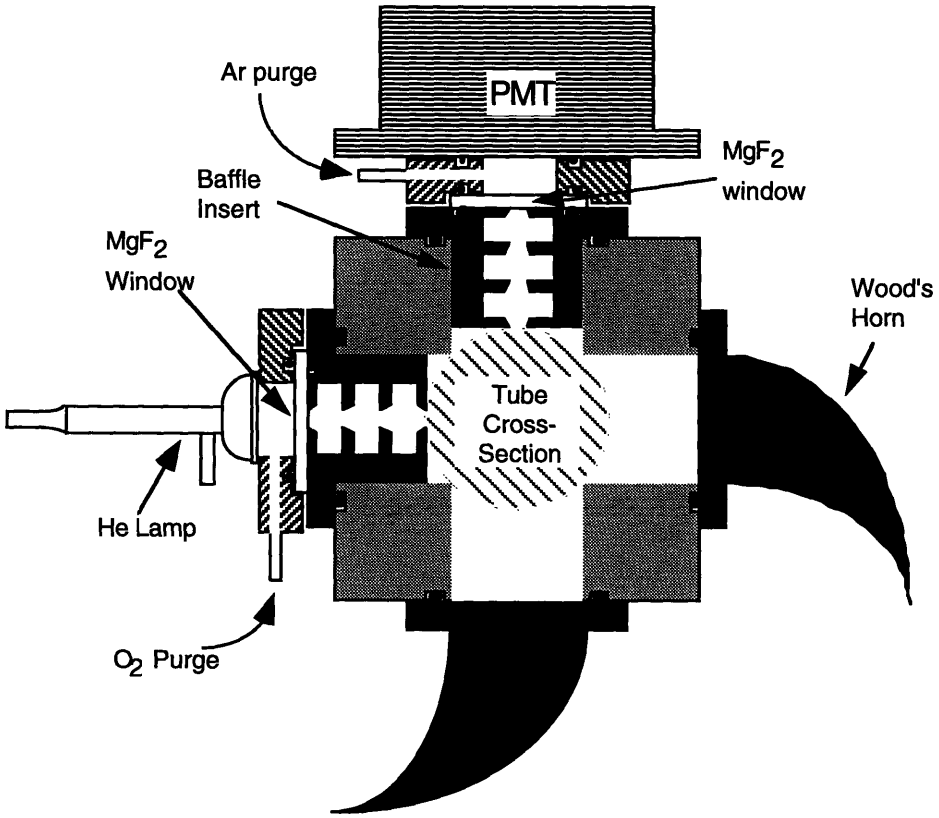

Figure 2. Schematic of detection block used to monitor H-atoms.

At a dark count rate of 2-3 s^{-1}, the sensitivity of this system to hydrogen atoms was about (1000 counts s^{-1}) / (10^{11} molecule cm^{-3}) at 2 torr total pressure. As the total pressure in the flow tube was raised from 2 to 300 torr, the count rate dropped by about a factor of four for the same initial [H] (measured by titration with NO_2). The decrease in

sensitivity is mainly due to the loss of fluorescence by collisional quenching of excited H-atoms. Reduced sensitivity at the higher pressures made it impractical to measure rate constants accurately above 300 torr.

Ozone

Mixtures of ozone were prepared via a multistep process. Ozone was initially generated by flowing O_2 through a Welsbach ozonator and then stored on a silica gel trap at about 195 K. Excess oxygen was removed from the trap by pumping it down to about 5 torr. The trap was allowed to warm slightly to increase the O_3 partial pressure. Mixtures of O_3 in He were prepared as needed in a 3 liter glass bulb. The partial pressure of O_3 was determined by UV absorbance at 253.7 nm ($\sigma = 1.15 \times 10^{-17}$ cm^2 molecule^{-1} taken from *DeMore et al.* [1992]) in a 0.98 cm flow-through quartz cell with light provided by a Pen-ray Hg lamp. Downstream of the absorption cell, the ozone mixture was exposed only to glass or Teflon surfaces in order to reduce heterogeneous losses. Ozone concentrations in the reaction zone were controlled by varying the flow rate of the O_3 / He mixture. The ozone concentration in the flow tube ranged from 1-10 $\times 10^{12}$ molecule cm^{-3}. Ozone concentrations were also determined downstream of the H-atom detection region by a second UV absorption measurement. The effluent of the flow tube was directed into a 50 cm long flow-through absorption cell with quartz windows. The two determinations of ozone concentration agreed to within 10%, indicating that decomposition within the flow tube was negligible. Bimolecular rate constants were calculated using the ozone density determined at the upstream absorption cell.

Chlorine

Chlorine gas was taken from a 3.60% mixture in UHP helium (Matheson Gas Co.). The concentration of Cl_2 in the flow tube was determined by its flow rate, the total

flow rate, and the total flow tube pressure. The densities of Cl_2 were in the range of 1 – 15 x 10^{12} molecule cm^{-3}.

IV.2.3 Data Acquisition and Processing

The output voltages from each of the flowmeters, photomultiplier tubes, and manometers were monitored by a PC equipped with a National Instruments A/D board.

IV.2.4 Procedure for Determination of Reaction Rate Constants

In order to determine a bimolecular rate constant we proceeded through several experimental steps. First, the injection rate of the excess reactant was set at a known value. The concentration of the excess reactant was calculated assuming that it was evenly mixed in the region downstream of the movable inlet. Next, the signal intensity of the limiting reactant detector was recorded for several different movable injector positions. The logarithm of signal intensity was then plotted as a function of injector-detector distance. After a linear least squares fit was made to the data points, the value of the observed pseudo-first-order rate constant, k^I_{obs}, was determined by multiplying the resulting slope by $-\bar{u}$. This process was repeated for several different excess reactant concentrations. A plot was then made of k^I_{obs} *vs.* excess reactant concentration. A linear least squares fit was applied to the data points. The slope of the fit was considered to be the observed bimolecular rate constant, k_{obs}.

IV.3 Model Results

The numerical model described in chapter II was used to simulate a flow tube study of H-atom reactions. The following parameters were used: $\bar{u}$ = 1500 cm s^{-1}, a = 1.2 cm, T = 298 K, Ar carrier gas, μ = 0.000227 cm g s^{-1}, $D_A P$ = 1140 cm^2 s^{-1} torr, γ = 0, developing flow conditions, radial averaging of C_A

over the region of $r < 0.5a$. Predictions of the error incurred when using the plug flow approximation are depicted in figure 3.

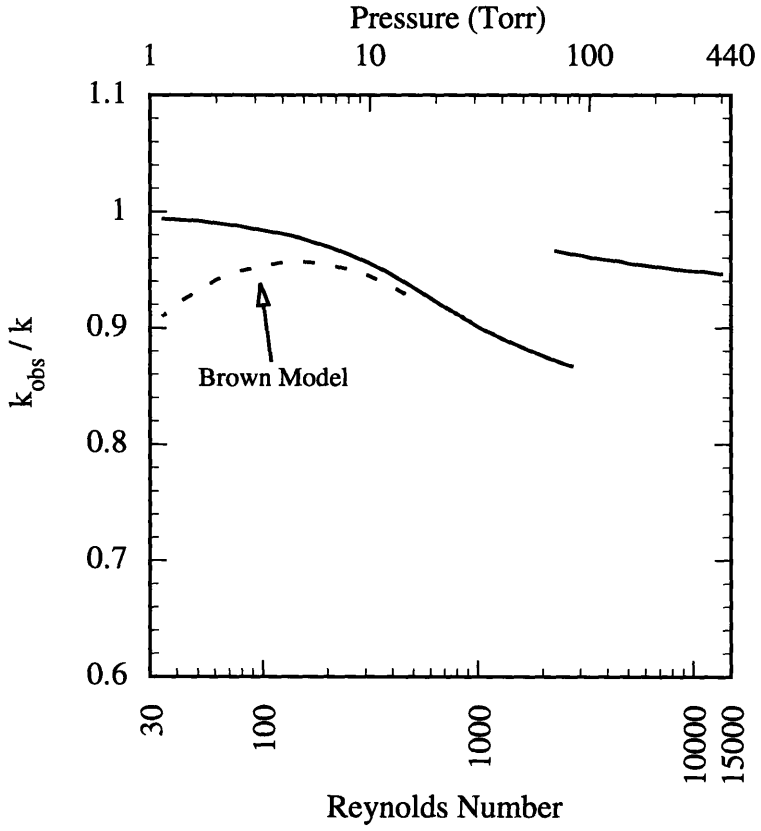

Figure 3. Relative observed rate constants for H-atom reactions as predicted using the numerical model (solid line) and the model of *Brown* [1978] (dashed line).

Comparison of figure 3 with figure 6 of chapter II shows that according to our model, the error incurred when using the plug flow approximation is much less for the case of H-atom reactions than for Cl-atom reactions. This result is largely due to the fact that the molecular diffusion coefficient of H-atoms is almost an order of magnitude larger than that of Cl; thus radial concentration gradients are minimized. For H-atom reactions in the laminar flow

regime, the numerical model predicts that the plug flow approximation will be accurate to within 5% for pressures less than 5 torr. The maximum deviation (approximately 15%) occurs at the laminar-turbulent transition. Within the turbulent flow regime the deviations are between 3 and 5%.

Because the H-atom molecular diffusion coefficient is very large, the assumption that axial diffusion can be neglected is less accurate; especially in low pressure laminar flow conditions ($P < 10$ torr). Fortunately, the fully developed laminar flow model of *Brown* [1976], which includes axial diffusion, produces accurate predictions of the deviation from plug flow in low pressure laminar flow conditions. The results from Brown's model are also depicted in figure 3. At 1 torr Brown's model predicts that the deviation is approximately 10%. As the pressure is increased the deviation decreases due to the slowing of axial diffusion. At approximately 5 torr, the deviation begins to increase due to the formation of radial concentration gradients. At pressures above 30 torr, axial diffusion is sufficiently restricted that Brown's model and our model agree to within 1%.

IV.4 Results and Discussion

IV.4.1 Reaction with Ozone

Experimental Results

Within the laminar flow regime, the observed kinetics appeared to be well behaved when the total pressure was below 5 torr. Plots of $\ln[H]$ vs. z were linear indicating that reactants were well mixed and that side reactions were minimized. Figure 4 shows a series of pseudo-first-order H-atom decays obtained in the low pressure laminar flow regime. Plots of k^I_{obs} vs. $[O_3]$ were also linear in low pressure conditions. Figure 5 shows a typical plot of k^I_{obs} *vs.* $[O_3]$ found in low pressure laminar flow. Values of k_{obs} determined for $P < 5$ torr ranged from 2.4×10^{-11} cm^3 molecule^{-1} s^{-1} to 3.2×10^{-11} cm^3 molecule^{-1} s^{-1}.

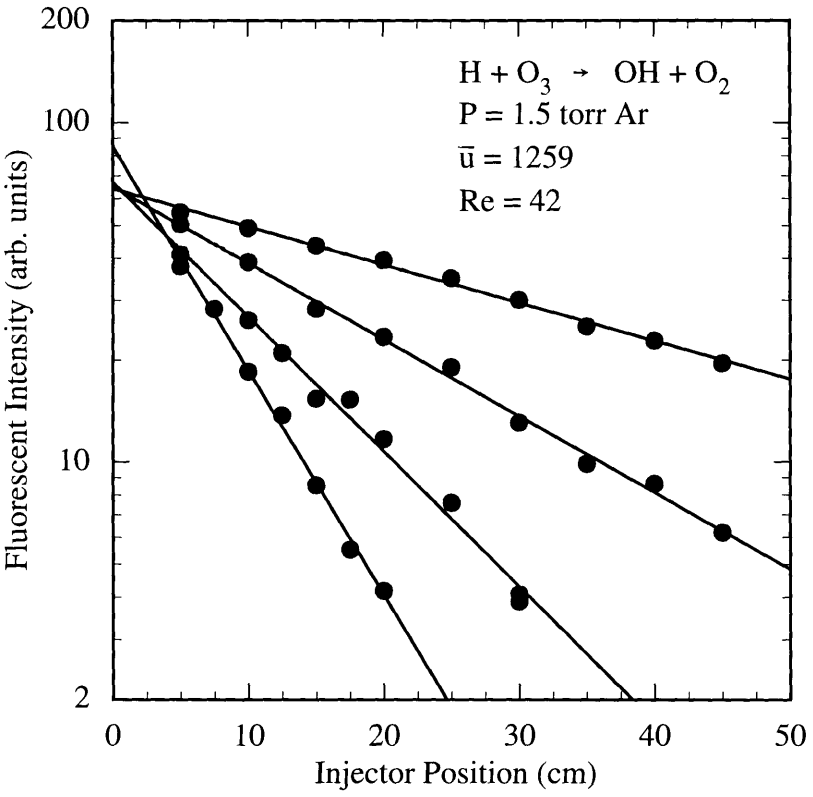

Figure 4. Typical H-atom decays observed for $P < 5$ torr.

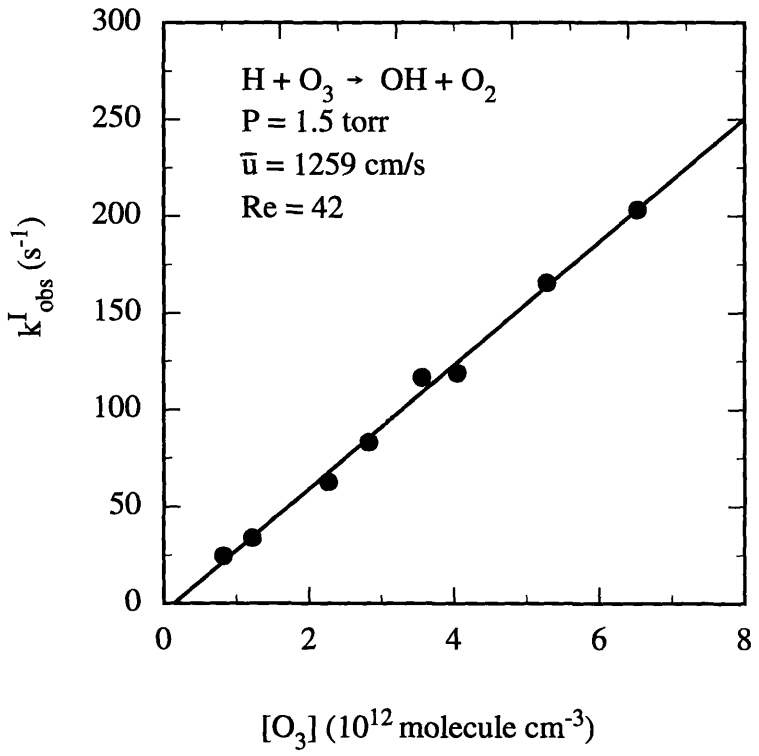

Figure 5. Typical plot of k^I_{obs} vs. [O_3] at pressures less than 5 torr.

At pressures above 5 torr and $Re < 1000$, the axial decays were frequently observed to be non-linear; an example is shown in Figure 6. The non-linearity in this flow regime is probably due to poor mixing of the excess reactant. In spite of their non-linearity, lines were fit to the axial decays so that values of k_{obs} could be calculated. The rate constants determined were typically lower that those obtained at $P < 5$ torr.

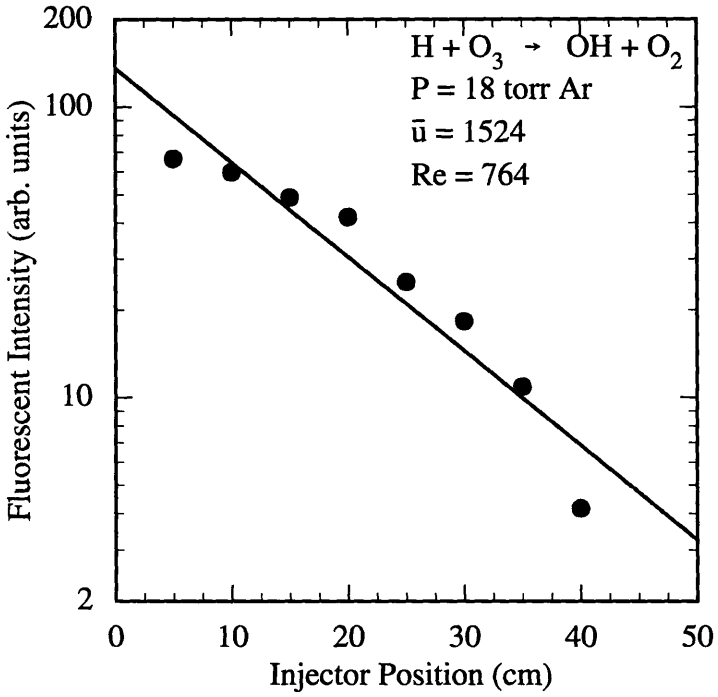

Figure 6. Typical H-atom decay for $P > 5$ torr and $Re < 1000$.

For $Re > 1000$, plots of $ln\ [H]$ vs. z were linear. The re-establishment of linearity is likely to be a result of increased reactant mixing and the flattening of the velocity profile. A typical example of the axial decays observed under these conditions are displayed in figure 7. Plots of k^I_{obs} *vs.* $[O_3]$ were also reasonably linear for $Re > 1000$ (see figure 8). The values of k_{obs} determined at Re > 1000 ranged from 2.4×10^{11} cm^3 molecule^{-1} s^{-1} to 2.8×10^{11} cm^3 molecule^{-1} s^{-1}.

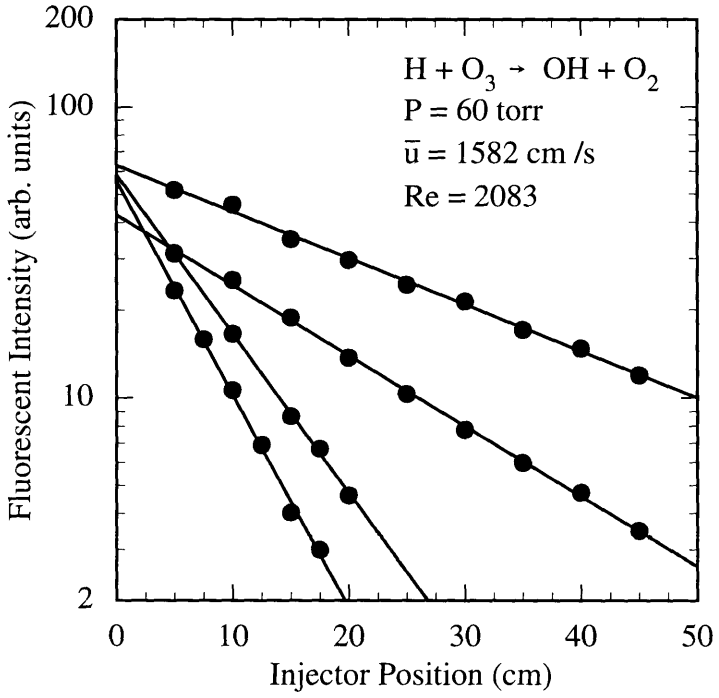

Figure 7. Typical axial decays of H-atoms for *Re* > 1000.

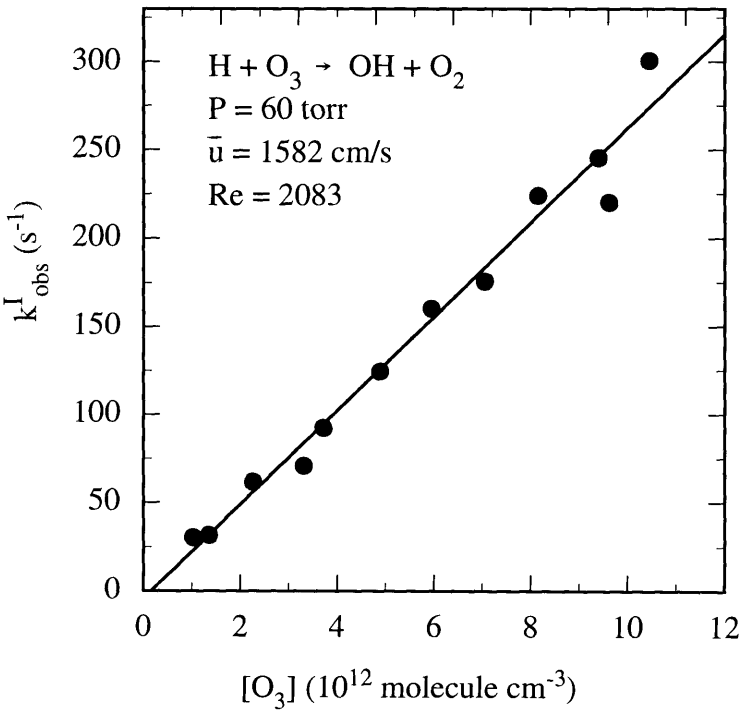

Figure 8. A typical plot of k^{I}_{obs} *vs.* [O3] for *Re* > 1000.

An additional series of experiments was performed with the turbulizer removed from the tip of the movable inlet. In the low pressure laminar regime the results obtained agree well with those obtained with the turbulizer in place. When the pressure was greater than 5 torr, the observed rate constants were significantly smaller than those obtained with the turbulizer in place. This finding agrees well with the flow visualization results (see section III.2) which indicated that the turbulizer is essential for rapid reactant mixing at all but the lowest pressures.

A collection of all of the values of k_{obs} obtained for reaction 1 with the turbulizer in place are listed in table I and plotted as a function of flow tube pressure in figure 9 and as a function of *Re* in figure 10. Averaging the results obtained below 5 torr gives a rate constant of 2.69×10^{-11} cm^3 $molecule^{-1}$ s^{-1}. If this value were to be corrected for axial diffusion, it would approximately be increased by 7% (see figure 3) giving a value of 2.90×10^{-11} cm^3 $molecule^{-1}$ s^{-1}. At intermediate pressure ($5 < P < 30$ torr), the measured rate constants generally have smaller values. However, the deviations are much larger than those predicted by our model and by Brown's model. This large negative deviation is probably primarily due to a lack of thorough mixing of the excess reactant. Rate constants determined at pressures above 30 torr and $Re > 1000$ are similar to those obtained in low pressures. The average value of k_{obs} in turbulent conditions ($Re > 2000$) is 2.56×10^{-11} cm^3 $molecule^{-1}$ s^{-1}. If k_{obs} is multiplied by a correction factor based on the results from our turbulent flow model, the value is increased by approximately 5% to give a value of 2.68×10^{-11} cm^3 $molecule^{-1}$ s^{-1}.

Table I. Observed bimolecular rate constants for $H + O_3 \rightarrow OH + O_2$

Pressure (Torr)	$\bar{u}$. (cm/s)	Reynolds Number	$k_{obs} \pm 2\sigma$ (10^{-11} cm^3 s^{-1})
1.5	1259	42	3.19 ± 0.08
1.6	1224	43	2.79 ± 0.08
1.6	1277	45	2.65 ± 0.07
2.0	1431	62	2.59 ± 0.11
2.1	1539	71	2.99 ± 0.09
2.6	1490	84	2.58 ± 0.21
2.9	1674	106	2.63 ± 0.18
3.0	1787	114	2.45 ± 0.16
3.4	1614	120	2.38 ± 0.16
3.4	1762	132	2.63 ± 0.08
5.5	1445	172	2.50 ± 0.36
5.1	1763	196	2.17 ± 0.22
8.2	1469	262	1.51 ± 0.12
8.2	1618	289	2.07 ± 0.12
13	1360	359	2.68 ± 0.22
12	1603	410	1.98 ± 0.16
11	1790	419	2.04 ± 0.08
13	2623	739	2.76 ± 0.18
13	2579	741	2.67 ± 0.18
18	1524	764	2.30 ± 0.10
38	1427	1180	2.53 ± 0.20
60	1582	2083	2.67 ± 0.14
69	1813	2723	2.55 ± 0.11
82	1652	2929	2.50 ± 0.07
110	1690	4079	2.47 ± 0.14
101	2139	4704	2.50 ± 0.15
108	2047	4842	2.78 ± 0.13
300	834	5421	2.58 ± 0.20
181	1374	5437	2.65 ± 0.09
136	1897	5633	2.46 ± 0.12
151	1759	5790	2.39 ± 0.10

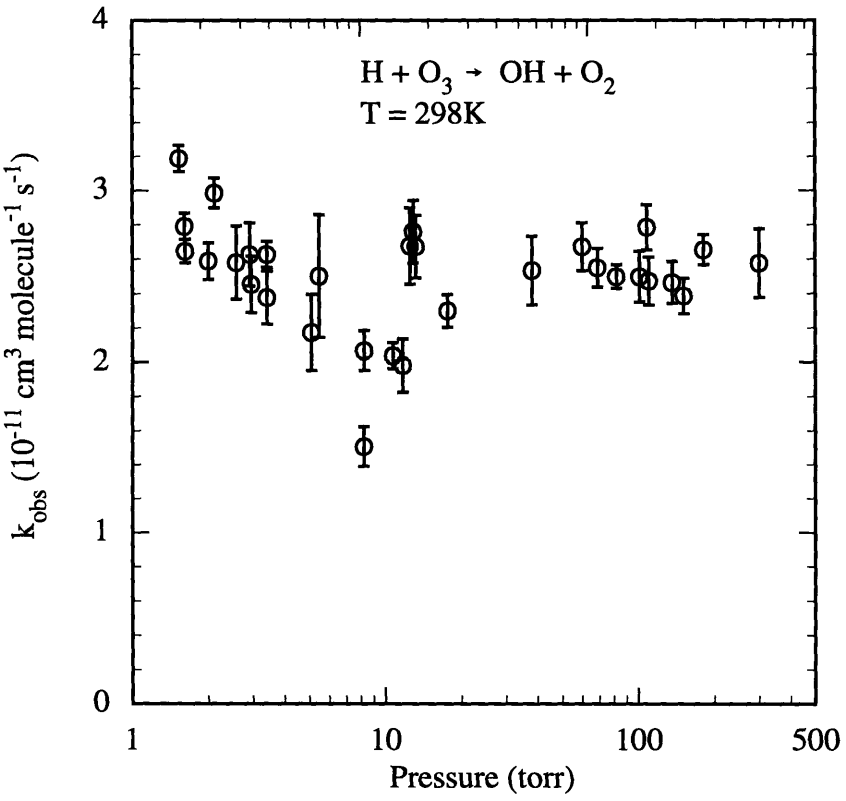

Figure 9. Plot of k_{obs} as a function of P for the reaction $H + O_3 \rightarrow OH + O_2$.

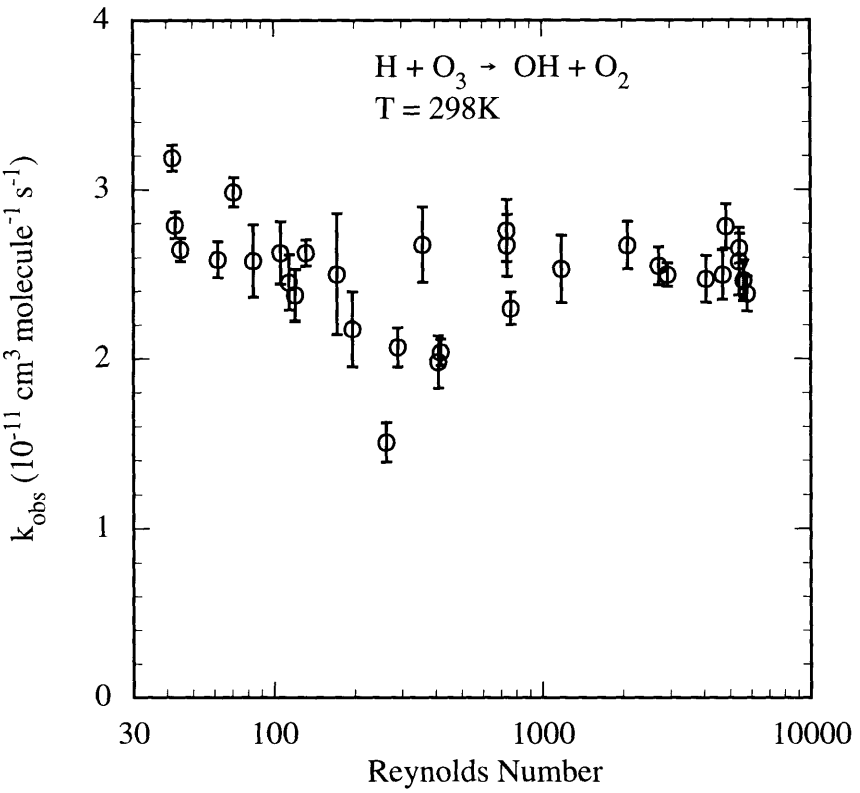

Figure 10. Plot of k_{obs} as a function of *Re* for the reaction $H + O_3 \rightarrow OH + O_2$.

Comparison with Previous Results

The rate constant of reaction 1 has previously been determined in four different studies (see table II). These studies have produced four similar values for the rate constant near room temperature. Upon review of these results *Atkinson et al.* [1989] have recommended 2.8 x 10^{-11} cm^3 $molecule^{-1}$ s^{-1} as the rate constant at 298 K and *DeMore et al.* [1992] have recommended a value of 2.9 x 10^{-11} cm^3 $molecule^{-1}$ s^{-1}.

Table II. Summary of previous investigations of the H + O_3 reaction.

$k \pm 2\sigma$ (10^{-11} cm^3 s^{-1})	Temperature (K)	Pressure Range (Torr)	Method	Reference
2.6 ± 0.5	300	0.5 torr Ar	Flow Tube	Phillips and Schiff [1962]
2.80 ± 0.20	300	10-40 torr Ar	Flash Photolysis	Lee et al. [1978]
2.79 ± 0.18	298	1.5-4 torr He	Flow Tube	Keyser [1979]
3.0	298	10-20 torr He	Flash Photolysis	Force and Wiesenfeld [1981]
2.8	298		Review Evaluation	Atkinson et al. [1989]
2.9	298		Review Evaluation	DeMore et al. [1992]

In low pressure laminar flow conditions, our corrected value of the rate constant is in excellent agreement with the recommended literature values. In turbulent flow conditions, our result is slightly lower (~5%) than the recommended value. The source of this discrepancy is uncertain. It is possible that the correction factors generated from our numerical model are too small. Another potential cause of this discrepancy is that the temperature within the flow tube might have been lower in turbulent flow conditions. For these studies we assumed that the temperature in the flow tube was equal to the room temperature which was between 293 and 300 K. After these results were collected we

checked this assumption by inserting a Cu-constantan thermocouple into the flow. Within the low pressure regime, the observed temperature was within 2 K of the room temperature. In the turbulent regime, the temperature was consistently lower than room temperature, sometimes as much as 8 K lower. The drop in temperature was presumably due to cooling of the gas upon expansion from the liquid Ar tank and the low rate of heat transfer in turbulent flow conditions. According to our calculations (using the Arrhenius parameters of *DeMore et al.*[1992]) a drop of 8 K would lead to a 5% lowering of the recommended rate constant, putting the turbulent flow value in good agreement with the recommended value.

IV.4.2 Reaction with Molecular Chlorine

Experimental Results

The determinations of the rate constant for the reaction of H + Cl_2 yielded results which were virtually identical to those found for H + O_3. Plots of *ln* [H] vs. z and k^I_{obs} vs. [Cl_2] were linear in low pressure laminar conditions and turbulent flow conditions. Table III contains a summary of the observed bimolecular rate constants obtained for H + Cl_2.

Table III. Observed bimolecular rate constants for H + $Cl_2 \rightarrow$ HCl + Cl

Pressure (Torr)	$\bar{u}$. (cm/s)	Reynolds Number	$k_{obs} \pm 2\sigma$ (10^{-11} cm^3 s^{-1})
1.5	1075	35	1.64 ± 0.05
1.7	1145	42	1.72 ± 0.03
1.8	1449	57	1.76 ± 0.12
6.5	1202	170	1.59 ± 0.08
7.1	1033	160	1.61 ± 0.24
9.3	1770	355	1.58 ± 0.16
61	1519	2009	1.59 ± 0.21
81	1790	3148	1.50 ± 0.13
107	1827	4232	1.63 ± 0.19
160	1496	5204	1.58 ± 0.11

The above results are plotted as a function of pressure and Re in figures 11 and 12 respectively.

In low pressure laminar flow conditions ($P < 5$ torr), the average value of the rate constant is 1.71 x 10^{-11} cm^3 $molecule^{-1}$ s^{-1}. If a correction is made using Brown's model, the average value is increased by approximately 7% giving a value of 1.83 x 10^{-11} cm^3 $molecule^{-1}$ s^{-1}. In turbulent conditions ($Re > 2000$), the average observed rate constant is 1.58 x 10^{-11} cm^3 $molecule^{-1}$ s^{-1}. If a correction based on our model results is applied, this average value increases by approximately 5% giving 1.65 x 10^{-11} cm^3 $molecule^{-1}$ s^{-1}.

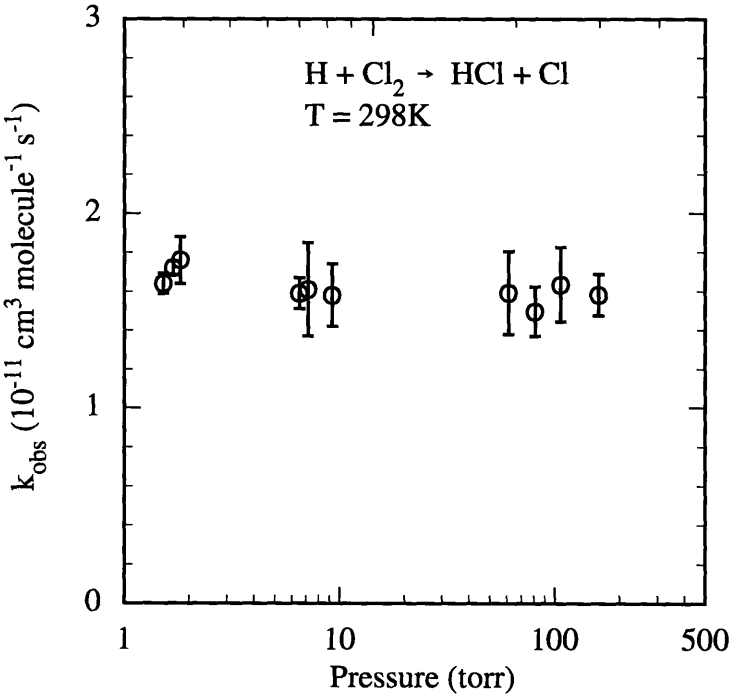

Figure 11. Plot of k_{obs} as a function of P for the reaction H + Cl_2 → HCl + Cl.

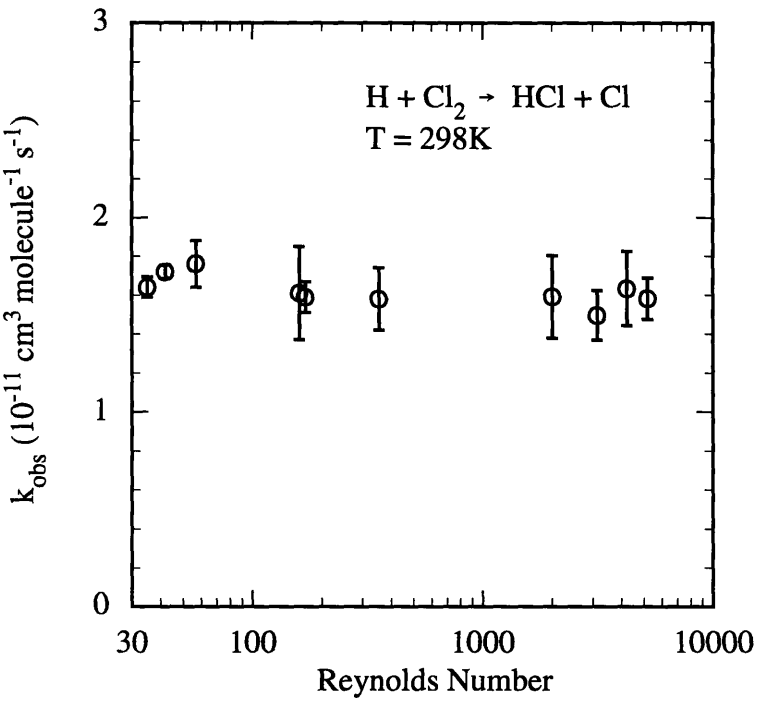

Figure 12. Plot of k_{obs} as a function of *Re* for the reaction $H + Cl_2 \rightarrow HCl + Cl$.

Review of Previous Investigations

The rate constant of reaction 2 has previously been determined in five different studies (see table IV). All of these studies have been performed using flow tube systems at low pressures and are in reasonable agreement with one another. The possibility of a pressure dependent rate constant has not been explicitly ruled out. However, several of the studies have determined that the rate constant has a positive temperature dependence well described by the Arrhenius equation; thus indicating a simple atom abstraction mechanism which should be pressure independent. In order to determine the accepted literature value at 295 K, we have averaged all the values except *Jaffe and Clyne*'s (because of large uncertainty of their result) and found the mean value to be $(1.80 \pm 0.36) \times 10^{-11}$ cm^3 molecule^{-1} s^{-1}.

Table IV. Summary of previous investigations of the reaction H + Cl_2.

$k \pm 2\sigma$ (10^{-11} cm^3 s^{-1})	Temperature (K)	Pressure Range (Torr)	Method	Reference
1.88 ± 0.25	295	1-3 torr He	Flow Tube	Wagner et al. [1976]
2.01 ± 0.32	295	1 torr Ar	Flow Tube	Bemand and Clyne [1977]
1.60 ± 0.20	295	1.8 torr	Flow Tube	Michael and Lee [1977]
2.13 ± 0.78	295	1 torr He & Ar	Flow Tube	Jaffe and Clyne [1981]
1.70 ± 0.26	295	1 torr He & Ar	Flow Tube	Kita and Stedman [1982]

In low pressure laminar flow conditions our corrected value of the rate constant is in excellent agreement with the recommended literature values. In turbulent flow conditions our corrected result is slightly lower (~8%) than the recommended value. Once again, the source of this discrepancy is uncertain. According to our calculations (using the Arrhenius parameters of *Bemand and Clyne* [1977]) a drop of 8 K would lead to a 5% lowering of the rate constant which would bring literature values in good agreement with the our turbulent flow result.

IV.5 Chapter Conclusions

There are several conclusions from our studies of H-atom reactions. As expected, for conditions within the conventional flow tube regime ($P < 5$ torr) we are able to obtain rate constants in good agreement with literature values if a correction is made for deviations from plug flow. This result indicates that our measurements of excess reactant density, average velocity, and flow tube pressure are reasonably accurate. At higher pressures within the laminar flow regime, we obtain lower values than those found in the literature. We believe that this is due to a combination of poor mixing of the excess reactant and

deviation from plug flow conditions. In the turbulent flow regime, we obtain observed bimolecular rate constants that are approximately 10 to 15% lower than the accepted literature values. When a small correction factor (~5%), based on our numerical model calculations, is applied to the observed bimolecular rate constants we get rate constants that are still slightly lower than the accepted literature values. The source of this small negative deviation is not known with certainty; however, it is likely that it is mainly caused by an over estimation of the flow tube temperature. Despite this slight discrepancy, we believe our results demonstrate that the plug flow approximation is accurate to within 15% in turbulent flow conditions.

References for Chapter IV

Atkinson, R., D. L. Baulch, R. A. Cox, R. F. Hampson, J. A. Kerr, and J. Troe, Evaluated kinetic and photochemical data for atmospheric chemistry: supplement III, *J. Phys. Chem. Ref. Data, 18*, 881, 1989.

Bemand, P. P., and M. A. A. Clyne, Atomic resonance fluorescence for rate constants of rapid bimolecular reactions, *J. Chem. Soc., Faraday Trans. 2, 72*, 783, 1977.

Brown, R. L., Tubular flow reactors with first-order kinetics, *J. Res. Nat. Bur. Stand., 83*, 1, 1978.

DeMore, W. B., S. P. Sander, C. J. Howard, A. R. Ravishankara, D. M. Golden, C. E. Kolb, R. F. Hampson, M. J. Kurylo, and M. J. Molina, *Chemical kinetics and photochemical data for use in stratospheric modeling, JPL Publication 92-20*, 1992.

Force, A. P., and J. R. Wiesenfeld, Laser photolysis of O_3 / H_2 mixtures: the yield of the $H + O_3 \rightarrow HO_2 + O$ reaction, *J. Chem. Phys., 74*, 1719, 1981.

Jaffe, S., and M. A. A. Clyne, Reactions of atomic hydrogen and deuterium with Cl_2 and Br_2, *J. Chem. Soc., Faraday Trans. 2, 77*, 531, 1981.

Keyser, L. F., Absolute rate constant and temperature dependence of the reaction between hydrogen (^2S) atoms and ozone, *J. Phys. Chem., 83*, 645, 1979.

Kita, D. and D. H. Stedman, Kinetic studies of reactions of hydrogen atoms with HCl, Cl_2 and NOCl, and chlorine atoms with H_2 and NOCl, *J. Chem. Soc., Faraday Trans. 2, 78*, 1249, 1982.

Lee, J. H., J. V. Michael, W. A. Payne, and L. J. Stief, Absolute rate of the reaction of hydrogen atoms with ozone from 219–360 K, *J. Chem. Phys., 69*, 350, 1978.

Michael, J. V., and J. H. Lee, Selected rate constants for H, O, N, and Cl atoms with substrates at room temperatures, *Chem. Phys. Lett., 51*, 303, 1977.

Phillips, L. F., and H. I. Schiff, Mass spectrometric studies of atomic reactions. III. Reactions of hydrogen atoms with nitrogen dioxide and with ozone, *J. Chem. Phys., 37*, 1233, 1962.

Wagner, H. G., U. Welzbacher, and R. Zellner, Rate measurements for the reaction $H + Cl_2 \rightarrow HCl + Cl$ by Lyman-α fluorescence, *Ber. Bunsenges. Physik. Chem., 76*, 518, 1976.

Chapter V: Kinetic Studies of Cl-atom Reactions

V.1 Introduction

In the previous chapter, the turbulent flow tube method was found to be capable of determining the rate constants of two H-atom reactions at pressures well above those available to conventional laminar flow tube methods. In this chapter we describe studies designed to verify that the turbulent flow tube method can be used to accurately determine rate constants as a function of pressure and temperature. The results from the studies of the following three chlorine atom reactions will be presented:

$$Cl + NO_2 + M \rightarrow ClNO_2 + M \quad (1)$$

$$Cl + CH_4 \rightarrow HCl + CH_3 \quad (2)$$

$$Cl + O_3 \rightarrow ClO + O_2 \quad (3)$$

V.2 Experimental Details

V.2.1 Flow Tube Construction

The apparatus used to determine the rate constants of the Cl-atoms with NO_2, CH_4, and O_3 is depicted in figure 1. The carrier gas source, vacuum pump, pressure gauges and mass flow meters used for this study are the same as those used for the H-atom reactions. A double jacketed Pyrex tube (1.2 cm i.d., 60 cm long) was used as the flow tube for these studies. The interior of the flow tube was left uncoated. The injection configuration for ozone (not shown in figure 1) is the same as that shown in figure 1 of chapter IV.

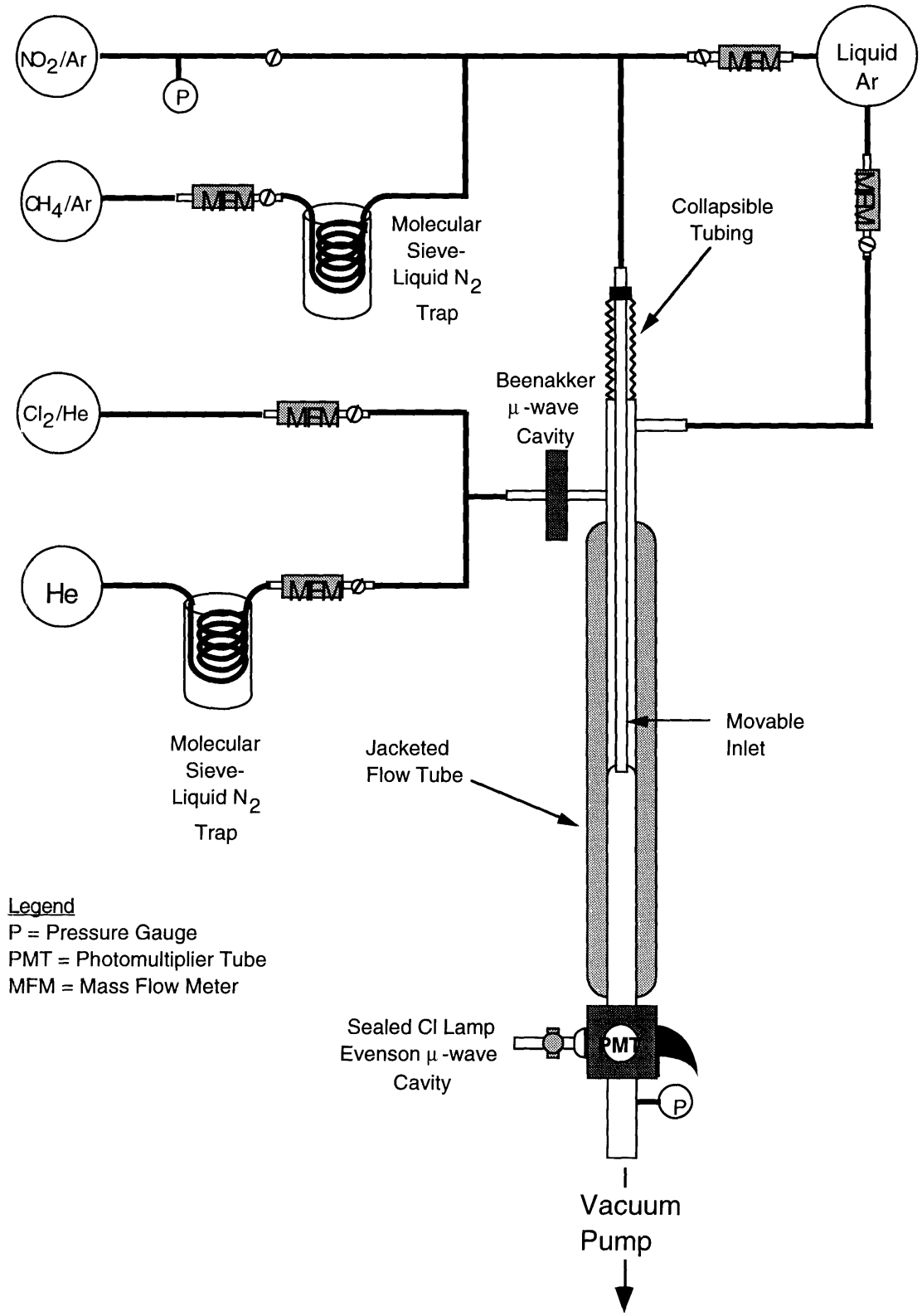

Figure 1. Schematic of apparatus used to study Cl-atom reactions.

The movable inlet was constructed from 4 mm o.d. Pyrex tubing which was coated with Halocarbon wax to reduce heterogeneous reactant removal. One of the problems associated with operating at low temperatures is that rubber o-rings no longer seal very well. This is especially true for seals on moving pieces such as reactant injectors. In order to avoid leaks, the movable inlet was encased in collapsible tubing which was sealed to the entrance of the flow tube and to the upstream end of the movable injector. This configuration allowed the injector to be repositioned without causing any leaks. A fan shaped Teflon "turbulizer" was attached to the end of the flow tube.

All rate constant determinations were performed under pseudo-first-order conditions with the molecular reactant (NO_2, CH_4, and O_3) added through the movable inlet. Observed rate constants, k_{obs}, were determined using the steps outlined in section IV.2.4.

V.2.2 Reactant Preparation and Detection

Chlorine atoms

Atomic chlorine was produced by passing UHP helium with a trace of Cl_2 through a microwave discharge. The majority of the helium that was passed through the discharge was pre-purified by passage through a molecular sieve trap at 77 K. A small amount of a 3.60% Cl_2 / He mixture was mixed in with the purified He before passing through the microwave discharge. The Cl-atoms were monitored by resonance fluorescence at 134.7 nm . The detection block used for this study is depicted in figure 2. Excitation radiation was provided by a sealed Cl-atom resonance lamp [*Schwab and Anderson*, 1982]. The lamp had a quartz body with two side arms. One of the side arms contained $PtCl_4$ which released Cl_2 into the lamp when heated with a nichrome wire wrapped around the exterior of the side arm. The other side arm contained barium metal which acted as a radical getter which lowered the background radiation due to impurity species. Radiation from the lamp was passed through a MgF_2 window located on the detection block. The fluorescing

radiation was detected with a Hamamatsu R1459P solar blind photomultiplier tube (PMT). A $BaCl_2$ window was placed in front of the PMT to block the transmission of wavelengths shorter than approximately 130 nm. This measure was taken to ensure that any trace quantities of atomic hydrogen or atomic oxygen would not interfere with our detection of Cl-atoms. The same baffling of the light source and the PMT used for the pulse studies were employed in this study. Argon was used to purge the area between the PMT and the $BaCl_2$ window and the area between the lamp and the MgF_2 window. The best signal to noise ratio was obtained when 250 mA was passed through the nichrome heating wire. At this setting, injecting 1.4×10^{11} molecule cm^{-3} of Cl_2 through the discharge gave 6000 counts and 100 background. The detection sensitivity was not greatly affected by pressure or temperature. We estimate that the starting [Cl] was less than 1×10^{11} molecule cm^{-3}.

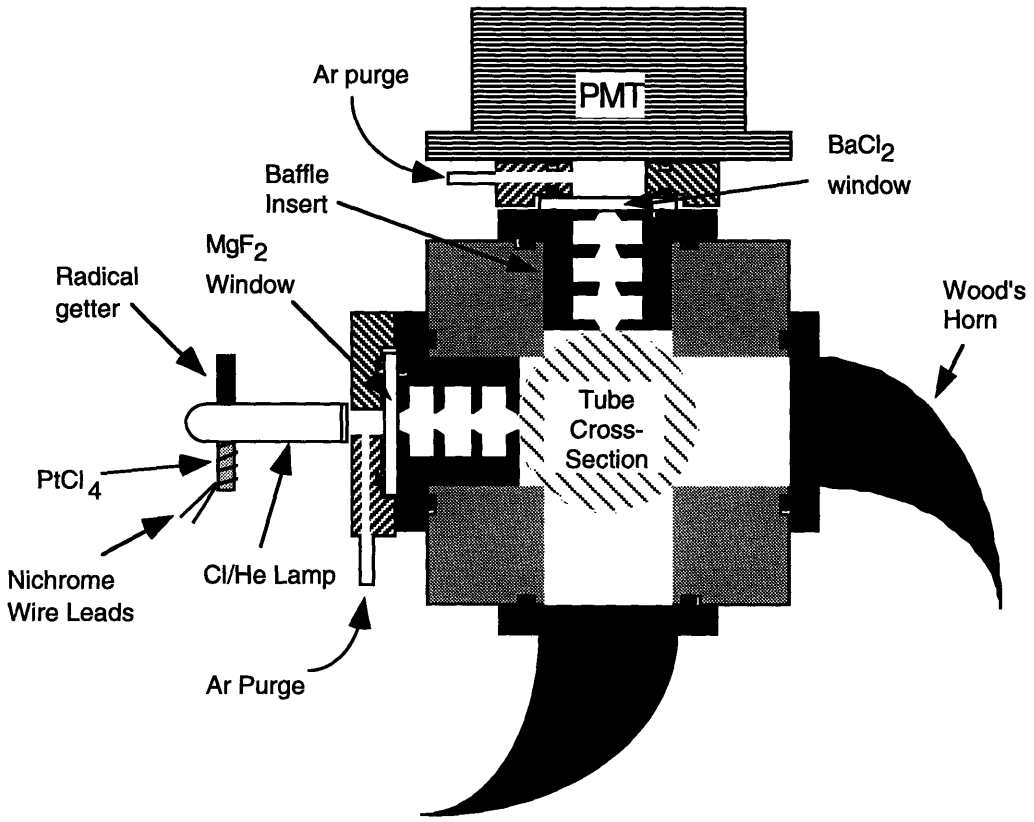

Figure 2. Schematic of detection block used for Cl-atom reaction studies.

Nitrogen Dioxide

Purified mixtures of NO_2 in argon were prepared through a multi-step process. First, the NO_2 was condensed at liquid nitrogen temperature (77 K) and then pumped on at 196 K to removed any volatile impurities. The NO_2 was then allowed to warm to room temperature and expand into a glass bulb. The pressure of pure NO_2 was noted and then diluted with Ar to approximately 700 torr. The flow rate of NO_2 into the system was determined by measuring the pressure drop in the bulb as a function of time with a correction made for N_2O_4 [*Zahniser et al.*, 1977]. Within the flow tube, the density of NO_2 ranged from $7x10^{12}$ to $1.7x10^{14}$ molecule cm^{-3}.

Methane

Methane was obtained from the Airco Gas Company as Grade 4 (99.99% Ultra Pure). According to manufacturer's specifications the ethane content is less than 20 ppm. Before injection into the flow tube, the methane was passed through a molecular sieve trap immersed in liquid nitrogen to remove any impurities (especially non-methane hydrocarbons). Similar measures have been shown to reduce non-methane hydrocarbon levels to approximately 1 ppm [*Keyser*, 1978]. The rate of methane injection was determined using a mass flow meter. Methane densities in the flow tube ranged from 3×10^{14} to 8×10^{15} molecule cm^{-3}.

Ozone

Ozone was prepared and injected into the flow tube in a manner identical to that described in the previous chapter for the study of $H + O_3$. Ozone densities in the flow tube ranged from 2×10^{12} to 20×10^{12} molecule cm^{-3}.

V.2.3 Temperature Control

In order to study the temperature dependence of a rate constant, the region downstream of the reactant mixing point must have a fairly constant temperature. For conventional low pressure flow tube studies, the rate of heat transfer is sufficiently high that the temperature in the reaction region can be assumed to be equal to the temperature of the flow tube walls. Thus, the reaction temperature can be set by circulating a refrigerated (or heated) fluid around the exterior of the flow tube. Control of the reaction temperature is a greater challenge at higher pressures because heat transfer between the flow tube wall and the gas in the interior of the tube decreases with increasing pressure [*Fahien*, 1983]. For low temperature studies we have found that near isothermal conditions can be created by cooling the carrier gas to the desired temperature before injecting it into the flow tube.

Figure 3 shows the temperature controlling portion of our apparatus. The main carrier gas flow was cooled by passing it through a 10 m length of copper tubing immersed in an ethanol bath. The ethanol bath was cooled with liquid nitrogen. After cooling, the gas was then injected into the flow tube. A double jacketed flow tube was used for variable temperature studies. The outside jacket of the flow tube was evacuated. A coolant liquid of ethanol or pentane was circulated through the inner jacket. The ethanol or pentane was cooled in a brass bucket that had copper pipe lengths fixed to its bottom. The cooper pipe lengths were immersed into a bath of liquid nitrogen. The temperature of the coolant liquid was measured using a Cu-constantan thermocouple. Within the flow tube the temperature was monitored at three points: at the entrance of the flow tube, at the end of the movable injector, and at a point immediately in front of the detection block. All of the thermocouple measurements were fed into an A/D board. Preliminary studies showed that the temperature was constant to within ~2 K throughout the reaction region if the wall coolant was within 5 K of the carrier gas temperature measured at the flow tube entrance.

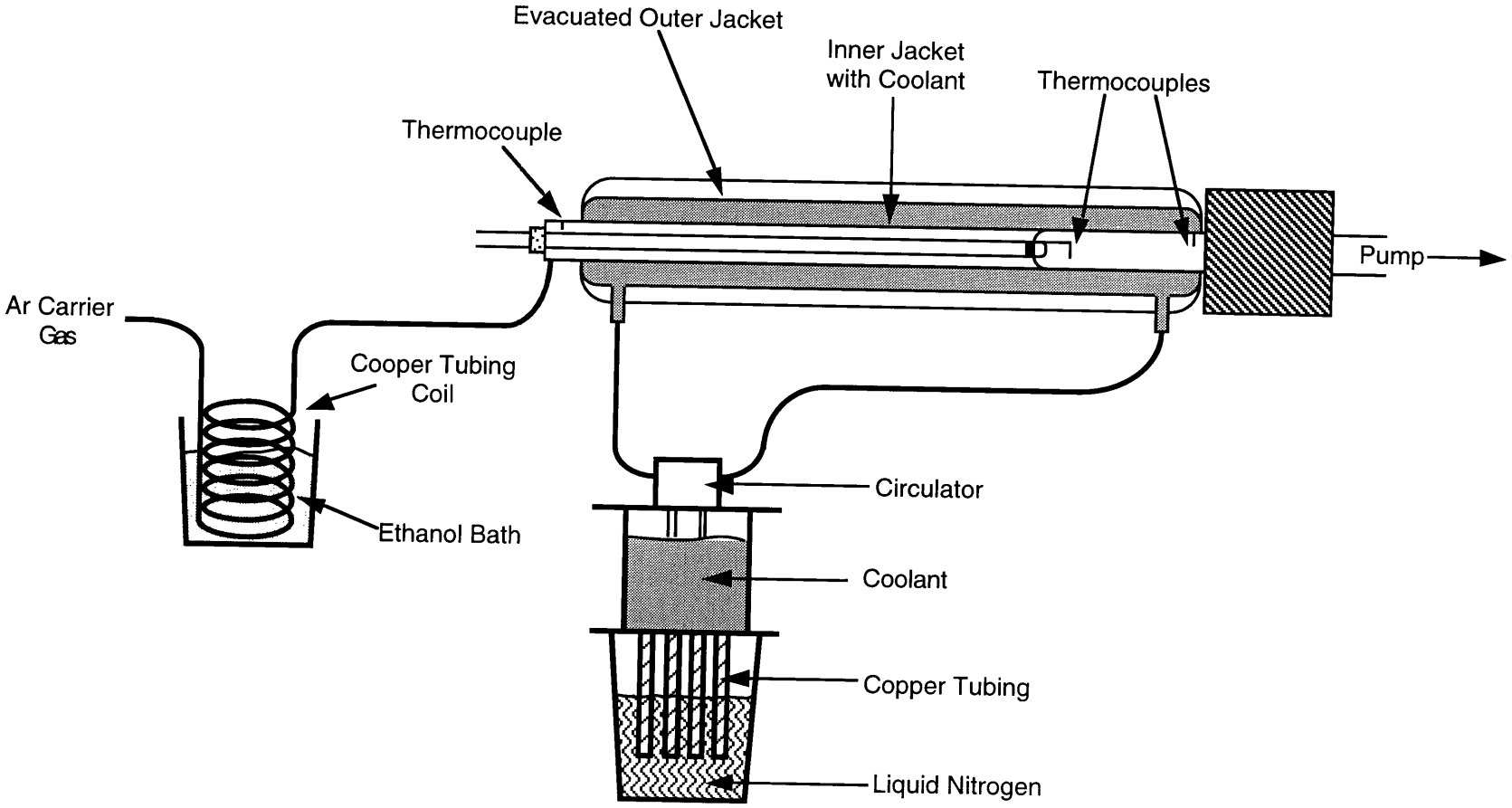

Figure 3. Schematic of the flow tube temperature controlling system

V.3 Model Results

The numerical model described in chapter II was used to predict the error incurred when using the plug flow approximation with the Cl-atom reactions in turbulent flow conditions. For simulating measurements at room temperature the following parameters were used: $\bar{u}$ = 1500 cm s^{-1}, a = 1.2 cm, T = 298 K, Ar carrier gas, μ = 0.000227 cm g s^{-1}, $D_A P$ = 140 cm^2 s^{-1} torr, γ = 1, developing turbulent flow conditions, radial averaging of C_A over the region of $r < 0.5a$. The model results are depicted in figure 4. Notice the predicted deviation is approximately 12% at Re = 2000 and slowly decreases to approximately 9% at Re = 10,000.

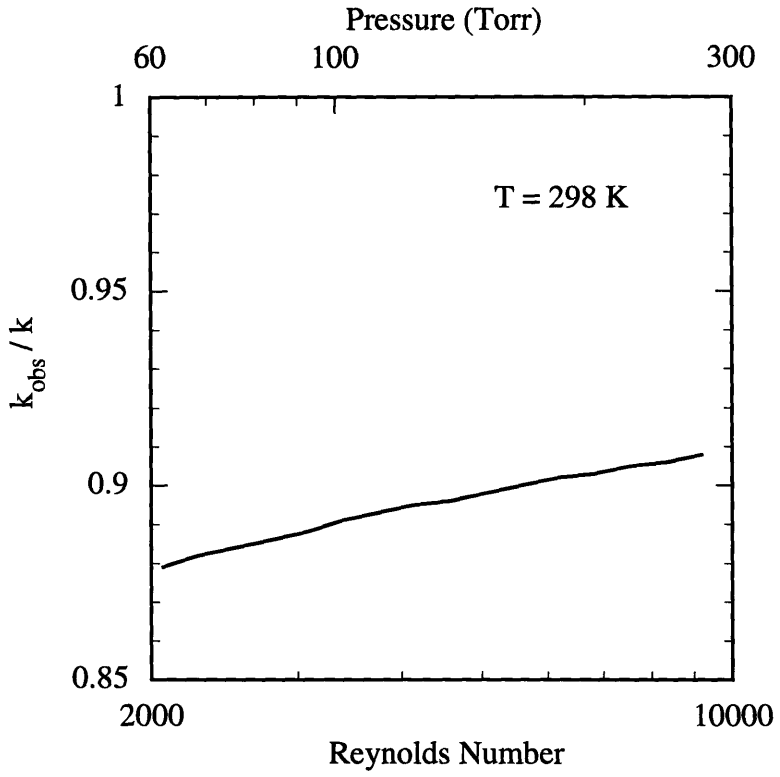

Figure 4. Relative observed rate constant for Cl-atom reactions predicted using the numerical model for developing turbulent flow conditions at room temperature.

In order to predict the effect of operating at lower temperatures, we used the model to simulate conditions at 180 K. The following parameters were used for the simulation: $\bar{u}$ = 1500 cm s^{-1}, a = 1.2 cm, T = 180 K, Ar carrier gas, μ = 0.000146 cm g s^{-1}, $D_A P$ = 58 cm^2 s^{-1} torr, γ= 1, developing flow conditions, radial averaging of C_A over the region of $r < 0.5a$. At both temperatures the molecular diffusion coefficient was calculated according to the procedure recommended by *Reid et al.* [1987]. Results from the model showed that the correction factors computed for T = 298 K and T = 180 K at a given *Re* agreed to within 0.1% despite the fact that the pressure at 180 K was less than 50% of the pressure at 298 K. Thus, we concluded that the deviation from plug flow was primarily dependent upon the Reynolds number and not greatly affected by the temperature.

V.4 Results and Discussion

V.4.1 Reaction with Nitrogen Dioxide

Experimental Results

The bimolecular rate constant for reaction 1 was determined at temperatures near 298 K and pressures between 50 and 250 torr. At each pressure, plots of *ln* [Cl] *vs.* injector position were linear indicating that secondary reactions were minimized (see figure 5). Plots of k^I_{obs} *vs.* NO_2 concentration were also linear (see figure 6). The observed bimolecular rate constants calculated from such plots are summarized in table I.

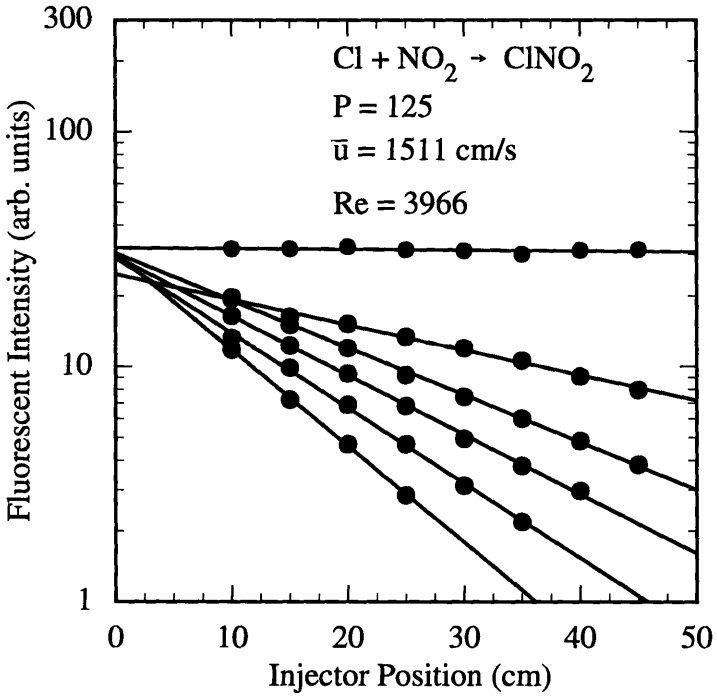

Figure 5. Typical plots of *ln* [Cl] vs. injector position for reaction 1.

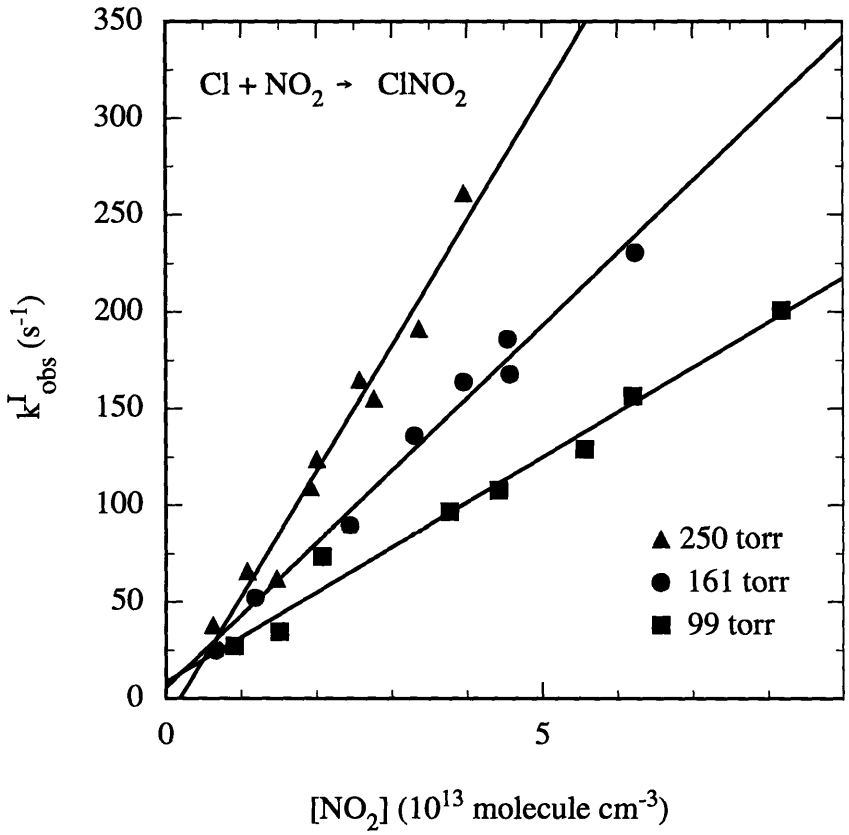

Figure 6. Typical plots of k^I_{obs} vs. [NO_2] for reaction 1.

Table I. Observed bimolecular reaction rate constants for Cl + NO_2 + M.

Temp. (K)	Pressure (torr)	Velocity (cm/s)	Re	$k^{II}_{obs} \pm 2\sigma$ (10^{-12} cm^3s^{-1})	Correction Factor	$k^{II} \pm 2\sigma$ (10^{-12} cm^3s^{-1})
297	50	2239	2410	1.07 ± 0.15	1.13	1.21 ± 0.18
301	68	1621	2318	1.61 ± 0.20	1.13	1.82 ± 0.23
298	78	1720	2857	1.70 ± 0.17	1.13	1.91 ± 0.20
297	99	1815	3842	2.13 ± 0.20	1.12	2.39 ± 0.23
298	113	1146	2781	1.94 ± 0.51	1.13	2.19 ± 0.57
302	125	1511	3966	2.73 ± 0.25	1.12	3.05 ± 0.28
296	161	1673	5773	3.38 ± 0.30	1.11	3.76 ± 0.33
302	223	1676	7846	4.36 ± 0.56	1.10	4.82 ± 0.62
296	250	1628	8755	5.67 ± 0.66	1.10	6.24 ± 0.72

Each observed bimolecular rate constant, k^{II}_{obs}, was multiplied by the numerically predicted ratio of k / k_{obs} to obtain the corrected bimolecular rate constant, k^{II}.

In order to calculate the termolecular rate constant, the corrected bimolecular rate constants were plotted as a function of total gas density (see figure 7). As can be seen from figure 7, the data points are essentially linear for the entire pressure range of this study. This linearity indicates that the highest pressure of this study (250 torr) is below the termolecular fall-off point. The slope of the linear least squares fit of the data points represents the termolecular rate constant. We have determined the termolecular rate constant to be $(7.2 \pm 0.8) \times 10^{-31}$ cm^6 molecule^{-2} s^{-1}. Note that the linear fit nearly passes through the origin indicating that pressure dependent secondary reactions were negligible.

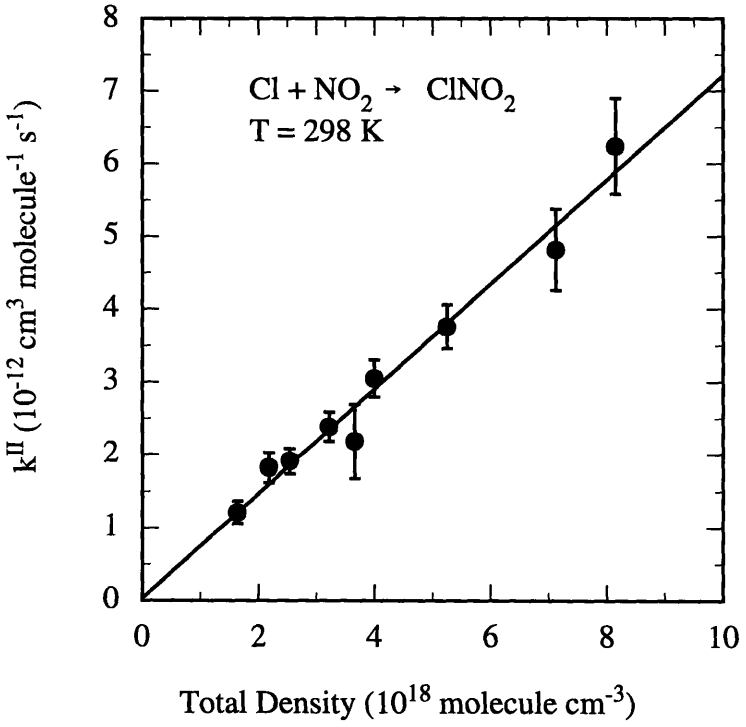

Figure 7. Plot of k^{II} vs. [M] for reaction 1.

Comparison with Previous Results

There have been four separate studies of reaction 1. Table II contains a summary of these experimental investigations. *Clyne and White* [1981] have performed the only study in Ar. Unfortunately their results have never been published; however, several compilations list their result as 7.2×10^{-31} cm^6 $molecule^{-2}$ s^{-1}. This result is in excellent agreement with our value. The value of k in He and N_2 has been determined by *Leu* [1984] using a conventional flow tube and by *Ravishankara et al.* [1988] using flash photolysis. The exact relationship between their results and ours is unknown due to the differing bath gases. However, the values for similar reactions such as Cl + NO +M, and OH + NO_2 + M, have been determined in He, Ar, and N_2 [*Anastasi and Smith*, 1976; *Lee et al.*, 1978] and have yielded room temperature rate constants in Ar which are only 5 to 20% larger than the values obtained in He. Thus we predict that the rate constant in Ar should be slightly larger than the values observed in He. Using this assumption, we believe that our results are in good agreement with those of *Ravishankara et al.* [1988] and slightly lower than those of *Leu* [1984].

Table II. Summary of previous experimental results for Cl + NO_2 + M.

$k \pm 2\sigma$ (10^{-31} $cm^6 s^{-1}$)	Temp (K)	Pressure Range (Torr)	Bath Gas	Method	Reference
7.2	298		Ar	Flow Tube	Clyne and White [1981]
8	300	1–7 torr	He	Flow Tube	Zahniser et al. [1977]
10.0 ± 1.2	296	1–7 torr	He	Flow Tube	Leu [1984]
14.8 ± 1.4	296	1–7 torr	N_2	Flow Tube	Leu [1984]
6.7 ± 0.32	298	15–500 torr	He	Flash Photolysis	Ravishankara et al. [1988]
13.0 ± 0.8	298	5–200 torr	N_2	Flash Photolysis	Ravishankara et al. [1988]
7.2 ± 0.8	298	50–250 torr	Ar	Turbulent Flow	This work

V.4.2 Reaction with Methane

Experimental Results

The rate constant of reaction 2 was determined for temperatures between 180 and 291 K. In all of these conditions plots of *ln* [Cl] vs. *z* were linear (see figure 8). We observed the Cl detection sensitivity to decrease slightly as the concentration of methane was increased. This result is presumably a result of increased collisional quenching of excited state Cl atoms or absorption of some of the excitation and fluorescing radiation by methane. Plots of k^{I}_{obs} vs. [CH_4] were linear at all the temperatures of this study. Figure 9 contains three typical plots. The values of k_{obs} were multiplied by a correction factor generated using our numerical model (see section V.3). It was assumed that the magnitude of the correction factor was a function of *Re* only. Table III contains a summary of the bimolecular rate constants determined at various temperature settings.

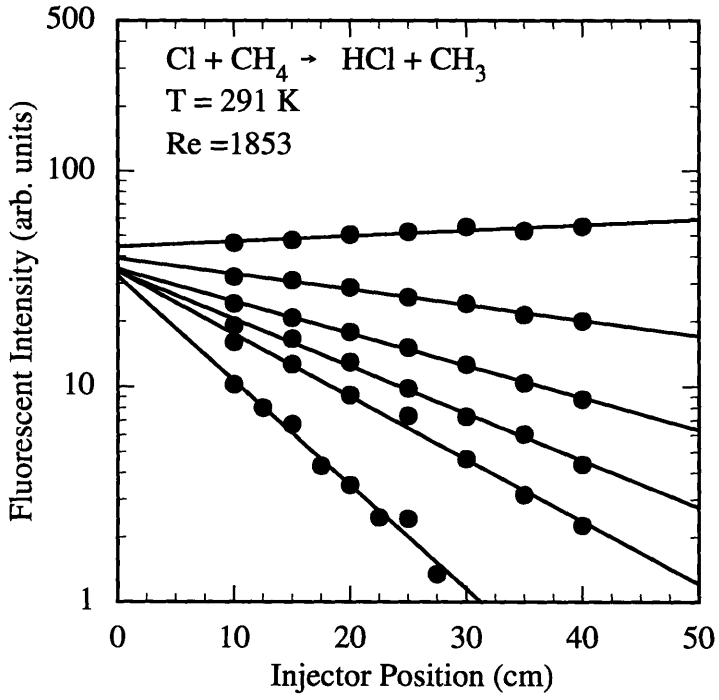

Figure 8. Typical plots of *ln* [Cl] vs. injector position for reaction 2.

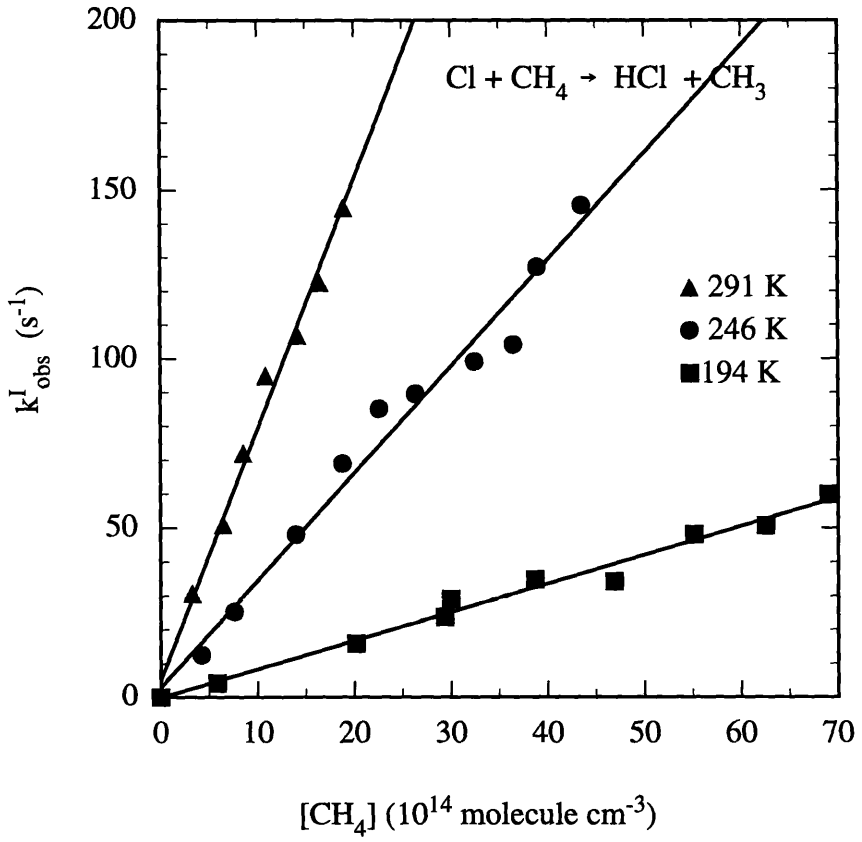

Figure 9. Typical plots of k^{I}_{obs} vs. [CH_4] for reaction 2.

Table III. Summary of experimentally determined bimolecular rate constants for Cl + CH_4.

Temp. (K)	Pressure (torr)	Velocity (cm/s)	Re	$k_{obs} \pm 2\sigma$ (10^{-14} cm^3s^{-1})	Correction Factor	$k \pm 2\sigma$ (10^{-14} cm^3s^{-1})
291	68	1257	2037	7.42 ± 0.60	1.14	8.42 ± 0.68
283	62	1281	1993	8.38 ± 0.75	1.14	9.52 ± 0.85
260	66	1247	2413	4.87 ± 0.25	1.13	5.51 ± 0.28
246	54	1143	2005	3.17 ± 0.31	1.14	3.60 ± 0.35
241	62	1224	2559	3.01 ± 0.29	1.13	3.40 ± 0.33
213	59	1159	2907	1.59 ± 0.23	1.13	1.79 ± 0.25
209	57	1168	2935	1.45 ± 0.19	1.13	1.63 ± 0.21
205	59	1040	2807	0.96 ± 0.23	1.13	1.09 ± 0.26
194	63	1164	3725	0.89 ± 0.07	1.12	1.00 ± 0.08
192	63	1148	3749	1.00 ± 0.14	1.12	1.12 ± 0.16
181	46	1246	3327	0.59 ± 0.05	1.12	0.66 ± 0.06

The Arrhenius parameters for reaction 2 were determined by plotting ln k vs. $1/T$ (see figure 10). The Arrhenius equation is given by $k(T) = A \exp(E / RT)$, where A is the pre-exponential factor, E is the activation energy, R is the gas constant. Thus the slope of the linear fit equals E / R and the intercept equals A. For the case of reaction 2, we have determined that $A = (7.0 \pm 1.6) \times 10^{-14}$ cm^3 molecule^{-1} s^{-1} and that $E / R = 1271 \pm 60$ K.

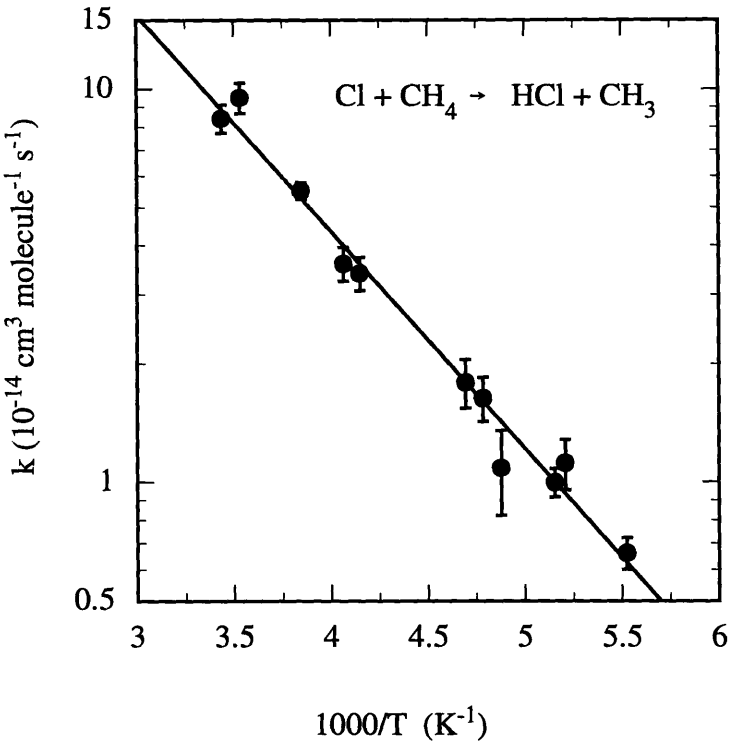

Figure 10. Arrhenius plot for Cl + CH_4. The line represents a least-squares fit to the data points.

Comparison with Previous Results

The rate constant of reaction 2 has previously been well characterized over most of the temperatures employed in this study. Detailed evaluations of these investigations can be

found in the literature [*Atkinson et al.*, 1989; *DeMore et al.*, 1992]. Table IV contains a summary of recently reported Arrhenius parameters for reaction 2.

Table IV. Summary of previous experimental results for Cl + CH_4.

k at 298 K ($10^{-14}cm^3s^{-1}$)	A ± 1σ ($10^{-12}cm^3s^{-1}$)	E / R ± 1σ (K)	Temp. Range (K)	Method	Reference
11.4 ± 0.6	7.94 ± 0.70	1260 ± 35	218–401	Flash Photolysis	Watson et al. [1976]
10.4 ± 1.0	7.93 ± 1.53	1272 ± 50	218–322	Flash Photolysis	Manning and Kurylo [1977]
11.3 ± 0.7	6.51 ± 0.79	1229 ± 27	200–299	Flash Photolysis	Whytock et al. [1977]
9.8 ± 0.4	8.2 ± 0.6	1320 ± 20	200–300	Flow Tube	Zahniser et al. [1978]
10.1 ± 0.4	7.4 ± 2.0	1291 ± 68	220–298	Flow Tube	Keyser [1978]
9.50 ± 0.40			221–375	Flash Photolysis	Ravishankara and Wine [1980]
10	9.6	1350	200–300	Review Evaluation	Atkinson et al. [1989]
10	11	1400 ± 150		Review Evaluation	Demore et al. [1992]
9.9	7.0 ± 1.6	1271 ± 60	181–291	Turbulent Flow	This Study

Table IV shows that our values of the rate constant at room temperature, pre-exponential factor, and activation energy are all in excellent agreement with those determined in previous studies. Figure 11 contains a comparison of our rate constants along with the rate constants recommended by *DeMore et al.* [1992]. The agreement is excellent at temperatures greater than 200 K. Below 200 K our results are approximately 10% higher than the recommended values.

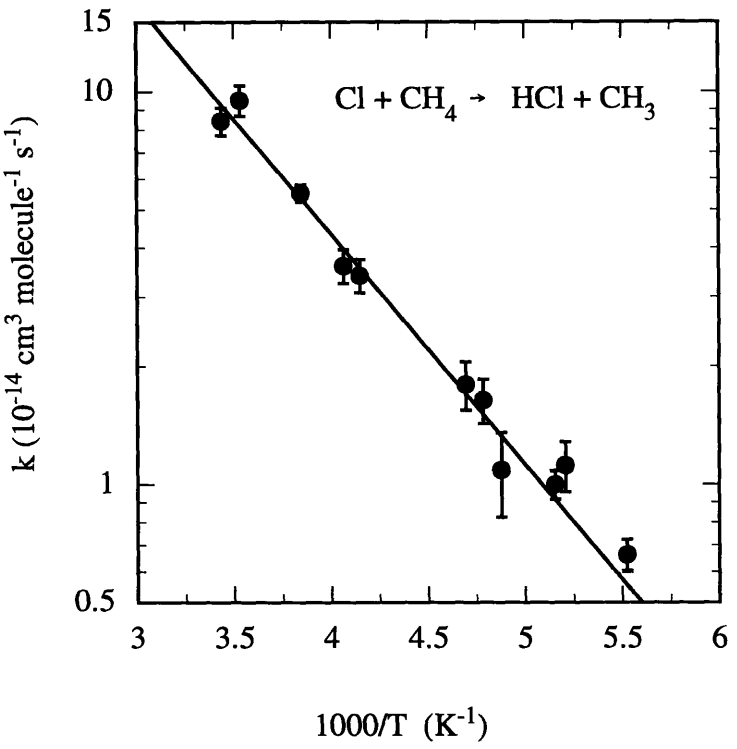

Figure 11. Comparison of our experimentally determined reaction rate constants (circles) for Cl + CH_4 with the values recommended by *DeMore et al.* [1992] (line).

V.4.3 Reaction with Ozone

Experimental Results

The reaction rate of Cl-atoms with ozone was observed in temperatures ranging from 206 to 296 K. The observed axial decays of Cl for reaction 3 were well described by a single exponential indicating that side reactions were unimportant. Plots of k^I_{obs} vs. [O_3] were linear at all temperatures (see figure 12).

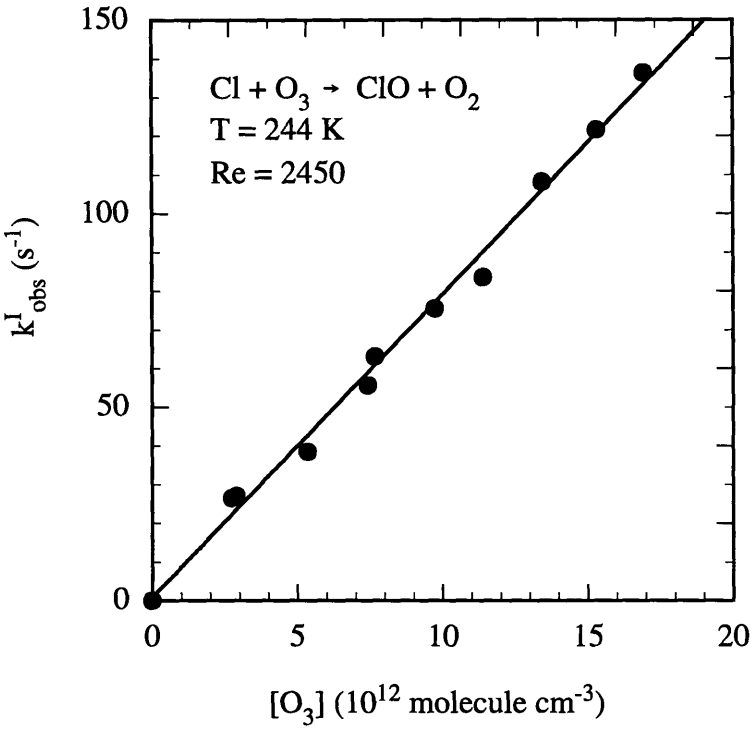

Figure 12. Typical plots of k^I_{obs} vs. [O3] for reaction 3.

The experimentally determined values of k_{obs} were corrected for errors resulting from non-plug flow conditions using the results of the numerical simulation described in section V.3. Table V contains a summary of our results. Notice that the magnitude of the experimentally determined rate constants are nearly independent of temperature and that the scatter in the values is much larger than has been observed in previous studies. The source of the increase in scatter is not known with certainty. An average of the rate constants near room temperature (T > 293 K) gives a mean value of (1.21 ± 0.26) x 10^{-11} cm^3 $molecule^{-1}$ s^{-1}. The Arrhenius parameters were determined to be A = 1.63 x 10^{-11} cm^3 $molecule^{-1}$ s^{-1} and E/R = 91 ± 61 K (see figure 13).

Table V. Summary of experimentally determined bimolecular rate constants for Cl + O_3.

Temp. (K)	Pressure (torr)	Velocity (cm/s)	Re	$k_{obs} \pm 2\sigma$ (10^{-11} cm^3s^{-1})	Correction Factor	$k \pm 2\sigma$ (10^{-11} cm^3s^{-1})
296	57	1648	2163	1.00 ± 0.14	1.13	1.13 ± 0.16
296	56	1524	1964	1.28 ± 0.09	1.14	1.45 ± 0.10
296	102	1605	3799	0.98 ± 0.06	1.12	1.10 ± 0.07
296	64	1582	2338	1.20 ± 0.12	1.13	1.36 ± 0.14
296	51	1735	2043	1.04 ± 0.09	1.14	1.18 ± 0.10
295	117	1427	3894	1.02 ± 0.11	1.12	1.14 ± 0.12
294	148	1129	3919	0.95 ± 0.13	1.12	1.06 ± 0.15
293	42	2094	2041	1.08 ± 0.11	1.14	1.23 ± 0.12
260	57	1594	2664	1.34 ± 0.11	1.13	1.51 ± 0.12
253	48	1564	2287	0.85 ± 0.12	1.13	0.96 ± 0.14
252	30	1696	1582	0.99 ± 0.14	1.14	1.13 ± 0.16
245	53	1585	2763	1.08 ± 0.15	1.13	1.22 ± 0.17
244	48	1557	2450	0.78 ± 0.04	1.13	0.88 ± 0.05
223	30	1745	2018	1.04 ± 0.13	1.14	1.18 ± 0.15
216	67	1649	4570	1.10 ± 0.16	1.12	1.23 ± 0.18
214	59	1264	3116	0.79 ± 0.12	1.13	0.89 ± 0.14
214	69	1561	4559	0.97 ± 0.07	1.12	1.08 ± 0.08
206	138	1320	8277	1.00 ± 0.06	1.10	1.10 ± 0.07

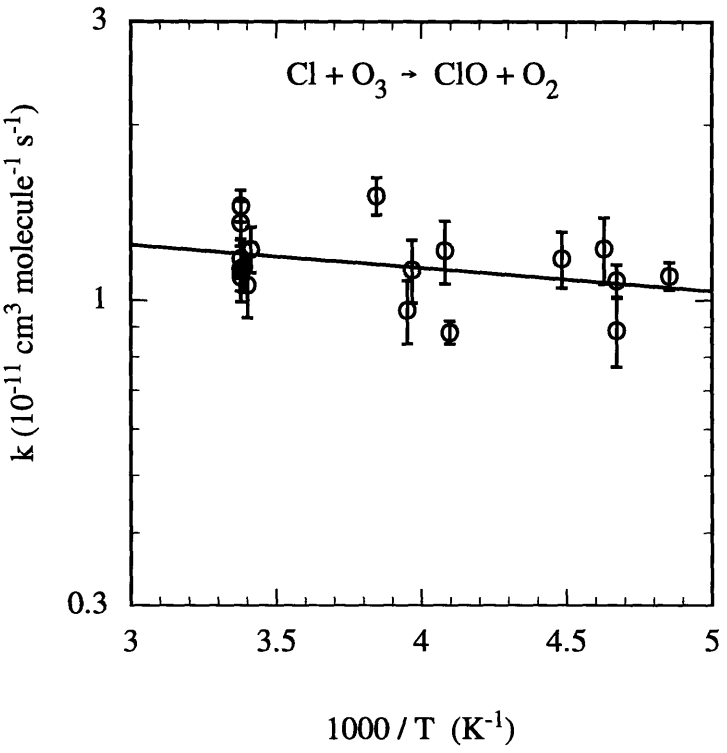

Figure 13. Arrhenius plot for Cl + O_3. The line represents a least-squares fit to the data points.

Comparison with Previous Results

There have been several previous investigations of reaction 3. Table VI contains a summary of these investigations. Notice that the room temperature values from the previous studies are in reasonably good agreement, but the values of the Arrhenius parameters are conflicting. Our room temperature value is in good agreement with the values recommended by *Atkinson et al.* [1989] and *DeMore et al.* [1992]. At low temperatures our values are larger than the recommended values (at T = 220 K our Arrhenius parameters predict that the rate constant is 1.08 where the parameters recommended by *DeMore et al.* predicts a value of 0.88). However, at all temperatures our results are in excellent agreement with *Nicovich et al.*[1990] – the most recent investigation of reaction 3. They observed rate constants at temperatures below 273 K that were larger

than those found in previous studies. In figure 14 we have plotted our data along with the lines used by *Nicovich et al.* [1990] to fit their data.

Table VI. Summary of previous experimental results for $Cl + O_3$.

k at 298 K ($10^{-11}cm^3s^{-1}$)	A ± 1σ ($10^{-11}cm^3s^{-1}$)	E / R ± 1σ (K)	Temp. Range (K)	Method	Reference
1.33 ± 0.26	5.18	418 ± 28	221–629	Flow Tube	Clyne and Nip [1976]
1.09 ± 0.04	2.94 ± 0.49	298 ± 39	213–298	Flash Photolysis	Kurylo and Braun [1976]
1.16 ± 0.06	3.08 ± 0.30	290 ± 30	220–350	Flash Photolysis	Watson et al. [1976]
1.30 ± 0.13	2.35 ± 0.50	171 ± 30	210–360	Flow Tube	Zahniser et al. [1977]
1.14 ± 0.05	2.49 ± 0.38 1.19 ± 0.20	233 ± 46 33 ± 37	264–385 189–263	Flash Photolysis	Nicovich et al. [1990]
1.2	2.7	257	205–298	Review Evaluation	Atkinson et al. [1989]
1.2	2.9	260 ± 100		Review Evaluation	Demore et al. [1992]
1.21 ± 0.26	1.63 ± 0.34	91 ± 61	206–296	Turbulent Flow	This Work

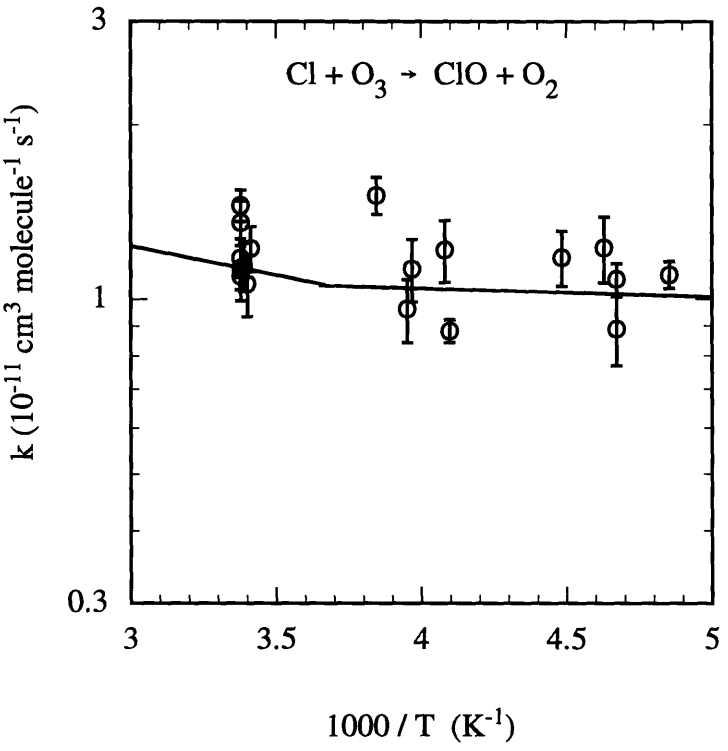

Figure 14. Comparison of our experimentally determined reaction rate constants (circles) for Cl + O_3 with the Arrhenius expressions of by *Nicovich et al.* [1990] (lines).

V.5 Chapter Conclusions

There are several conclusions that can be drawn from our studies of Cl-atom reactions. The results from of our investigation of the reaction of Cl + NO_2 have shown that the turbulent flow tube technique can be used to accurately characterize the pressure dependence of a reaction. The results from of our investigations of the chlorine atom reactions with methane and ozone have shown that the turbulent flow tube technique can be used to accurately characterize a reaction over a wide range of temperatures without heterogeneous interferences. We believe that we have experimentally validated the turbulent flow tube technique as a versatile method for determining the reaction rate constants of elementary gas phase reactions.

References for Chapter V

Anastasi, C., and I. W. M. Smith, Rate measurements of reactions of OH by resonance absorption, *J. Chem. Soc. Faraday Trans. 2, 72*, 1459, 1976.

Atkinson, R., D. L. Baulch, R. A. Cox, R. F. Hampson, J. A. Kerr, and J. Troe, Evaluated kinetic and photochemical data for atmospheric chemistry: supplement III, *J. Phys. Chem. Ref. Data, 18*, 881, 1989.

Clyne, M. A. A., and W. S. Nip, Study of elementary reactions by atomic resonance absorption with a non-reversed source, *J. Chem. Soc. Far. Trans. II, 72*, 838, 1976.

Clyne, M. A. A., and I. F. White, as reported by Baulch, D. L., J. Duxbury, S. J. Grant, D. C. Montague, Evaluated kinetic data for high temperature reactions, *J. Phys. Chem. Ref. Data, 10, supplement 1*, 1981.

DeMore, W. B., S. P. Sander, C. J. Howard, A. R. Ravishankara, D. M. Golden, C. E. Kolb, R. F. Hampson, M. J. Kurylo, and M. J. Molina, *Chemical kinetics and photochemical data for use in stratospheric modeling, JPL Publication 92-20*, 1992.

Fahien, R. W., *Fundamentals of Transport Phenomena*, McGraw-Hill, New York, 1983.

Kurylo, M. J., and Braun, W., Flash photolysis resonance fluorescence study of the reaction $Cl + O_3 \rightarrow ClO + O_2$ over the temperature range 213–298 K, *Chem. Phys. Lett.*, 37, 232, 1976.

Keyser, L. F., Absolute rate and temperature dependence of the reaction between chlorine (^2P) atoms and methane, *J. Chem. Phys., 69*, 214, 1978.

Lee, J. H., J. V. Michael, W. A. Payne, and L. J. Stief, The temperature dependence of the rate constant for $Cl + NO + N_2 \rightarrow NOCl + N_2$, *J. Chem. Phys., 68*, 5410, 1978.

Leu, M. T., Kinetics of the reaction $Cl + NO_2 + M$, *Int. J. Chem. Kinet., 16*, 1311, 1984.

Manning, R. G., and M. J. Kurylo, Flash photolysis resonance fluorescence investigation of the temperature dependencies of the reactions of Cl atoms with CH_4, CH_3Cl, CH_3F, and C_2H_6, *J. Phys. Chem., 81*, 291, 1977.

Nicovich, J. M., K. D. Kreutter, and P. H. Wine, Kinetics of the reactions of Cl and Br with O3, Int. J. Chem. Kinet., 22, 399, 1990.

Ravishankara, A. R., and P. H. Wine, A laser flash photolysis-resonance fluorescence kinetics study of the reaction $Cl + CH_4 \rightarrow CH_3 + HCl$, *J. Chem. Phys., 72*, 25, 1980.

Ravishankara, A. R., G. J. Smith, and D. D. Davis, A kinetics study of the reaction of Cl with NO_2, *Int. J. Chem. Kinet., 20*, 811, 1988.

Reid, R. C., J. M. Prausnitz and T. K. Sherwood, *The Properties of Gases and Liquids, 4th ed.*, McGraw-Hill, New York, 1987.

Schwab, J. J., and J. G. Anderson, Oscillator strengths of Cl(I) in the vacuum ultraviolet, *J. Quant. Spectrosc. Radiat. Transfer., 27*, 445, 1982.

Watson, R., G. Machado, S. Fischer, and D. D. Davis, A temperature dependence kinetics study of the reactions of Cl with O_3, CH_4, and H_2O_2, *J. Chem. Phys., 65*, 2126, 1976.

Whytock, D. A., J. H. Lee, J. V. Michael, W. A. Payne, and L. J. Stief, Absolute rate of the reaction of Cl with methane form 200-500 K, *J. Chem. Phys., 66*, 2690, 1977.

Zahniser, M. S., F. Kaufman, and J. G. Anderson, Kinetics of the reaction $Cl + O_3 \rightarrow ClO + O_2$, Chem. Phys. Lett., 37, 226, 1976.

Zahniser, M. S., J. S. Chang, and F. Kaufman, Chlorine nitrate: kinetics of formation by $ClO + NO_2 + M$ and of reaction with OH, *J. Chem. Phys., 67,* 997, 1977.

Zahniser, M. S., B. M. Berquist, and F. Kaufman, Kinetics of the reaction $Cl + CH_4 \rightarrow CH_3 + HCl$ from 200 to 500 K, *Int. J. Chem. Kinet., 10*, 15, 1978.

Chapter VI: Kinetic Studies of OH Reactions

VI.1 Introduction

In this chapter we describe the kinetic studies of two reactions involving the hydroxyl radical. The hydroxyl radical (OH) plays an important role in the chemistry of the earth's atmosphere. In the troposphere, OH is chiefly responsible for the initiation of catalytic cycles which lead to the oxidation and ultimately the removal of many trace species including carbon monoxide, sulfur dioxide, and methane. In the stratosphere, OH participates in the HO_x ozone destruction cycle and also leads to the interconnection of several other catalytic cycles.

Our first study focused on the reaction of hydroxyl radicals with hydrogen peroxide

$$OH + H_2O_2 \rightarrow HO_2 + H_2O \qquad (1)$$

Reaction 1 plays an important role in the HO_x cycle because when coupled with

$$HO_2 + HO_2 \rightarrow H_2O_2 + O_2$$

it leads to the loss of odd hydrogen in the atmosphere. Reaction 1 has previously been characterized in several studies; however, the temperature dependence remains uncertain.

The second reaction studied was

$$OH + HNO_3 \rightarrow H_2O + NO_3 \qquad (2)$$

Reaction 2 plays an important role in the atmosphere because it leads to the loss of odd hydrogen and the conversion of nitric acid into the highly reactive NO_3.

VI.2 Experimental Details

VI.2.1 Flow Tube Construction

A schematic of the apparatus used in this study is depicted in figure 1 . The flow tube, pressure gauges, mass flowmeters, cooling system and vacuum pump are identical to those described in chapter V for the study of chlorine atom reactions.

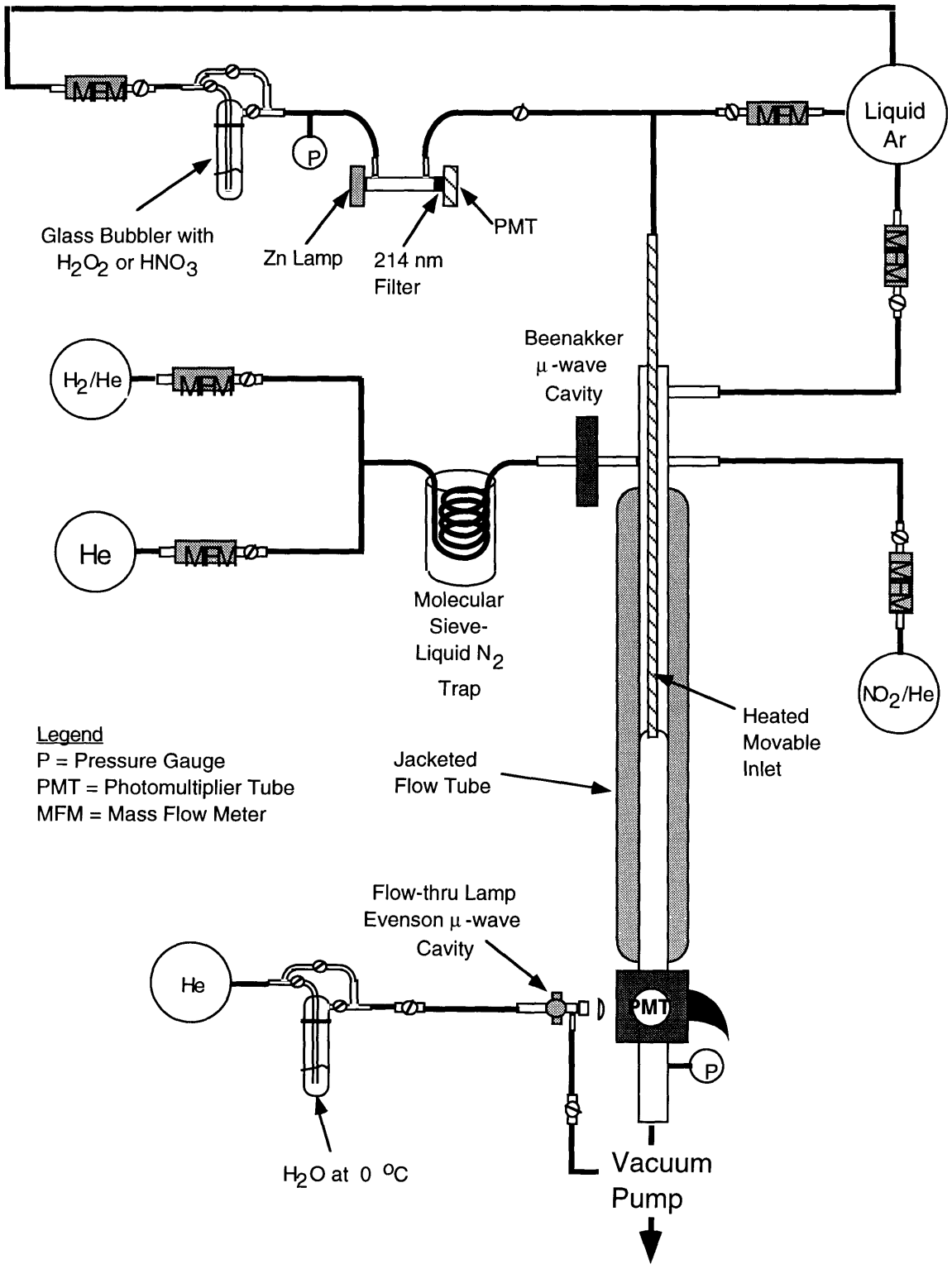

Figure 1. Schematic of apparatus used for the study of OH reactions.

The movable inlet was constructed from two concentric 80 cm long Pyrex tubes (5 mm o.d. and 9 mm o.d.). A nichrome heating wire was wrapped around the exterior of the 5 mm tube. The tubes were then sealed together creating a jacketed inlet. For studies at $T < 273$ K, the interior of the movable inlet was heated to approximately room temperature by applying a voltage (< 50 V) across the wire. This measure was taken to avoid reactant condensation in the movable inlet. Due to the small amount of flow which passed through the movable inlet, this heating had only a slight effect ($\Delta T < 5$ K) on the temperature downstream of the movable inlet.

All rate constant determinations were performed under pseudo-first-order conditions with the molecular reactant (C_2H_6, H_2O_2, and HNO_3) added through the movable inlet. Observed rate constants, k_{obs}, were determined using the steps outlined in section IV.2.4.

VI.2.2 Reactant Preparation and Detection

Hydroxyl Radicals

Hydroxyl radicals were produced by the reaction

$$H + NO_2 \rightarrow OH + NO$$

NO_2 was taken from a 2% NO_2 / Ar mixture made in the laboratory. Hydrogen atoms were produced by passing He with a trace of H_2 through a microwave discharge. The discharge was typically operated at a power level of 75 W. Trace levels of H_2 were produced by mixing a flow of UHP helium with a flow of a 1% H_2 / He mixture. In order to minimize the production of impurity radicals, the mixture was passed through a molecular sieve trap at 77K before being passed through the μ-wave discharge. Hydrogen atoms and NO_2 were injected at the rear of the flow tube approximately 40 cm upstream of the reaction region. The concentration of NO_2 was kept in excess of the H-atom concentration with the following typical values; $[NO_2] = 6 \times 10^{11}$ molecule cm^{-3} and

$[H_2] = 2 \times 10^{11}$ molecule cm^{-3}. Production of OH was estimated to go to greater than 90% completion before entering the reaction region. A typical starting concentration of OH was $[OH]_o = 2 \times 10^{11}$ molecule cm^{-3}. This value was varied to check for interfering side reactions.

Hydroxyl radicals were detected by monitoring the fluorescence of the $A(^2\Sigma) \rightarrow X(^2\Pi)$ transition at 309.0 nm. The detection block used for the OH reaction studies is depicted in figure 2. Excitation radiation was provided by a capillary μ-wave lamp (0.2 cm i.d.). A flow of argon was passed through a water bubbler at 273 K and then through the lamp. A maximum signal to noise ratio was obtained when the lamp pressure was approximately 3 torr and the power level of the μ-wave generator was set at approximately 20 W (1 W reflected). The lamp color was a bright red. A quartz lens and baffling (0.3 cm i.d. apertures) were used to confine the light to the center of the flow tube and reduce the amount of scattered radiation. The fluorescent intensity was monitored using a photomultiplier tube (EMI 9789QA) shielded by an interference filter with maximum throughput at 310 nm. The fluorescent signal was found to be linear with [OH] for $[OH] < 10^{12}$ molecule cm^{-3} by titrating an excess of hydrogen atoms ($\sim 2 \times 10^{12}$ molecule cm^{-3}) with a known concentration of NO_2. The amount of scattered light was determined either by turning off the upstream discharge or by turning off the flows of NO_2 and H_2 (while the discharge remained on). Both methods yielded similar scattered counts. The scattered counts were found to be minimized if the flow tube was covered with black cloth near the detection block. At 100 torr and a background count of approximately 100 counts s^{-1}, an OH density of 1×10^{11} molecule cm^{-3} gave a signal of approximately 2000 counts s-1. As the pressure was increased, the background count rate increased which subsequently reduced the sensitivity of the detection technique.

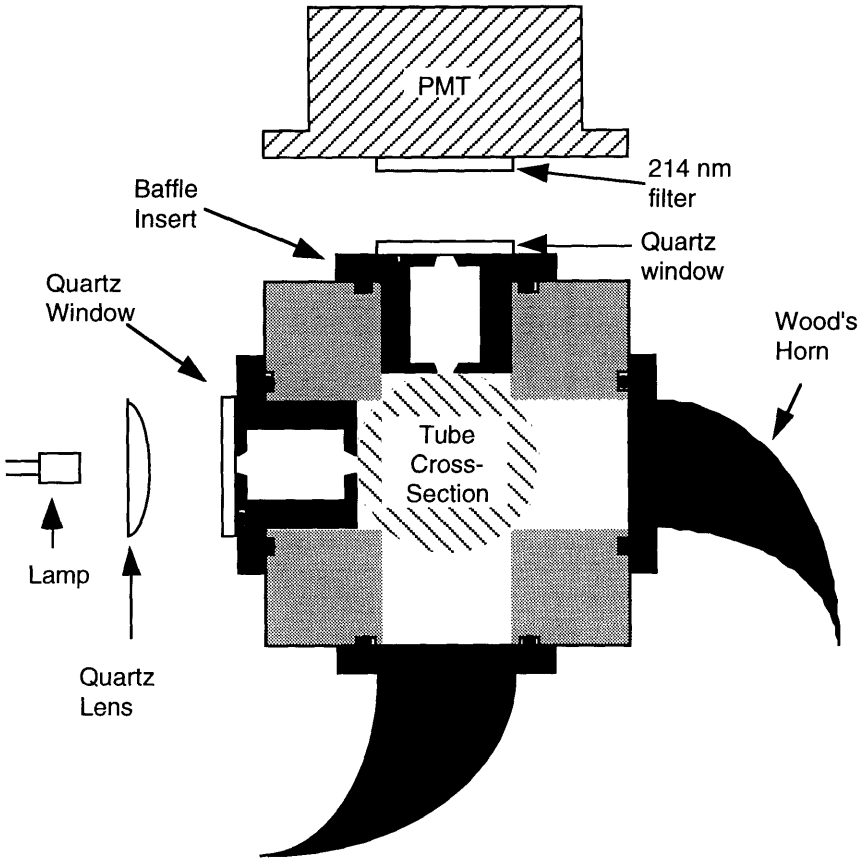

Figure 2. Detection block for studies of OH reactions

Ethane

Ethane was obtained from the Matheson Gas Co. and used without further purification. Its concentration was determined by monitoring its flow through a mass flow meter. Concentrations ranged from 1 to 20 x 10^{14} molecule cm^{-3}.

Hydrogen Peroxide

Hydrogen peroxide was obtained as a 50% mixture in water. The H_2O_2 was concentrated by bubbling Ar through the mixture for several days until the total volume was reduced to approximately 25% of its original value. The concentrated H_2O_2 was then

placed in a bubbler at 0 °C. A flow of argon was passed through the bubbler and into a 10 cm flow-through cell where the partial pressure of H_2O_2 was determined by measuring its absorbance at 213.9 nm. Light was provided by a zinc lamp and the intensity of the light was monitored with a photomultiplier tube. An interference filter (Corion G10-214-F, peak transmission of 12% at 214 nm, 10 nm width at half maximum transmittance) was placed in front of the photomultiplier tube. The cross section of H_2O_2 at 213.9 nm was taken to be 3.10×10^{-19} cm^2 $molecule^{-1}$ [*Kurylo et al.*, 1982a]. The H_2O_2 mixture was then further diluted with Ar before being passed into the movable inlet. After the partial pressure of hydrogen peroxide was determined, the reaction mixture was only exposed to glass and Teflon surfaces.

The concentration of hydrogen peroxide in the flow tube, $[H_2O_2]$, ranged from 1-15 $\times 10^{13}$ molecule cm^{-3}.

Nitric Acid

Anhydrous nitric acid was produced by mixing finely crushed $NaNO_3$ with concentrated sulfuric acid (approximately a 1:3 molar ratio) in a round bottom flask. The reaction mixture was evacuated for roughly 2 minutes to remove any dissolved gases. The reaction mixture was then stirred with a magnetic stirring bar while being gently heated with steam. Heating was necessary to dissolve $NaHSO_4$: a product of the reaction that can coat the $NaNO_3$ particles. Nitric acid was collected in a trap at 77K or 198K. The collected nitric acid was then placed in a bubbler. A flow of argon was passed through the anhydrous nitric acid for at least 1 hr before rate constant measurements were made. Similar nitric acid syntheses have yielded anhydrous nitric acid with less than 0.5% NO_2 [*Connell and Howard*, 1985]. We periodically determined the concentration of NO_2 in our nitric acid samples using two different methods. First, the NO_2 content was determined by measuring the UV spectrum of the nitric acid bubbler effluent using a spectrometer with a 172.8 cm path length. In this manner the mole fraction of NO_2 was found to be less than

0.6%. Second, the NO_2 content was determined by measuring the amount of OH produced by the reaction H + NO_2 when the nitric acid mixture was injected into a flow of H-atoms with the upstream NO_2 flow shut off. With this method the concentration of NO_2 was found to be roughly 0.1%.

Nitric acid was injected into the flow tube with the same configuration that was used for H_2O_2. The nitric acid cross section at 213.9 nm was determined to be 4.55 x 10^{-19} cm^2 $molecule^{-1}$ by interpolating values recommended by *DeMore et al.* [1992]. The nitric acid concentration was also periodically determined downstream of the OH detection block by monitoring its absorption at 184.9 nm in a 50 cm flow-through cell. Light was provided by a Pen-ray mercury lamp and the intensity of the light was monitored with a photomultiplier tube (Hamamatsu R1259). An interference filter with maximum transmittance at 185 nm was placed in front of the photomultiplier. The value of the nitric acid cross section at 184.9 nm was taken from *Connell and Howard* [1985] to be 1.64 x 10^{-17} cm^2 $molecule^{-1}$. The upstream and downstream values of [HNO_3] agreed to within 5% of each other at all temperatures and pressures indicating that no substantial decomposition was occurring during the injection process.

Nitric acid concentrations in the flow tube ranged from 1-15 x 10^{14} molecule cm^{-3}.

VI.3 Model Results

The numerical model described in chapter II was used to predict the error incurred when using the plug flow approximation with hydroxyl radical reactions in turbulent flow conditions. For simulating measurements at room temperature the following parameters were used: $\bar{u}$ = 1500 cm s^{-1}, a = 1.2 cm, T = 298 K, Ar carrier gas, μ = 0.000227 cm g s^{-1}, $D_A P$ = 234 cm^2 s^{-1} torr, γ = 1, developing turbulent flow conditions, radial averaging of C_A over the region of $r < 0.5a$. The model results are

depicted in figure 3. Notice the predicted deviation is approximately 13% at Re = 2000 and slowly decreases to approximately 10% at Re = 10,000.

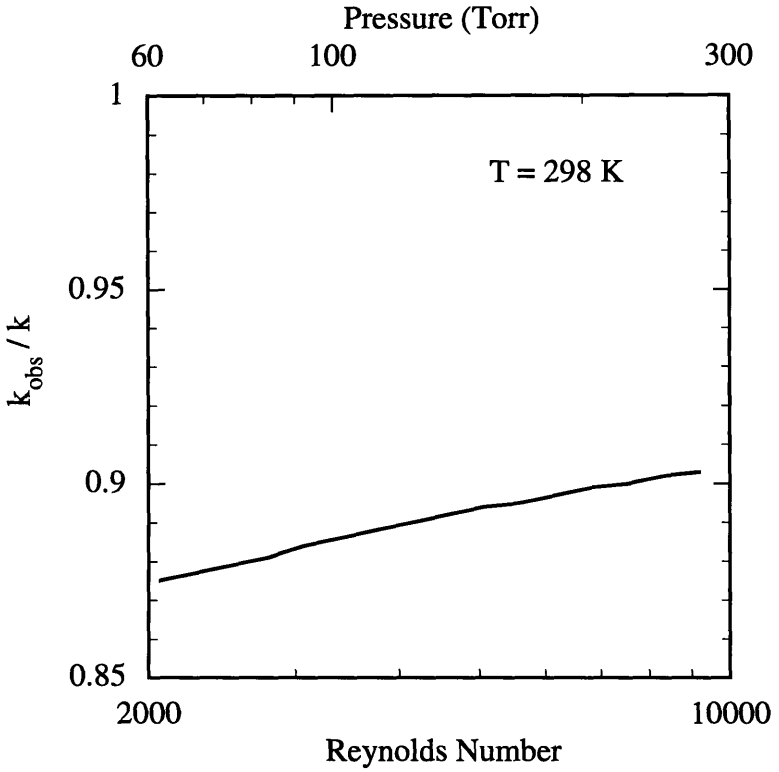

Figure 3. Calculated relative observed rate constant for OH reactions in turbulent flow conditions at room temperature.

In order to observe the effect of operating at lower temperatures, we used the model to simulate conditions at 240 K. The following parameters were used for the simulation: $\bar{u}$ = 1500 cm s^{-1}, a = 1.2 cm, T = 240 K, Ar carrier gas, μ = 0.000189 cm g s^{-1}, $D_A P$ = 161 cm^2 s^{-1} torr, γ= 1, developing flow conditions, radial averaging of C_A over the region of $r < 0.5a$. At both temperatures, the molecular diffusion coefficient was calculated according to the procedure recommended by *Reid et al.* [1987]. Results from the model showed that the correction factors computed for T = 298 K and T = 240 K at a given *Re* agreed to within 0.1%. Thus we reached the same conclusion for the case of OH

reactions as we did for Cl-atom reactions: the deviation from plug flow is primarily dependent upon the Reynolds number and not greatly affected by the temperature.

VI.4 Results and Discussion

VI.4.1 Reaction with Ethane

In order to test the experimental apparatus for systematic errors, the reaction rate for the well characterized reaction

$$OH + C_2H_6 \rightarrow H_2O + C_2H_5 \qquad (3)$$

was determined. The observed axial decays of OH were well fit with a single exponential and plots of k^I_{obs} vs. $[C_2H_6]$ were linear. The values of k_{obs} were multiplied by a correction factor generated using our numerical model (see section VI.3). It was assumed that the magnitude of the correction factor was a function of *Re* only. The bimolecular rate coefficients determined for this reaction are summarized in table I. Near room temperature, the rate constants are in reasonable agreement with each other. When the temperature is lowered to near 240 K, the rate constants decrease to approximately 50% of the room temperature values. At both temperatures our results do not exhibit a significant pressure dependence.

Table I. Observed bimolecular reaction rate constants for $OH + C_2H_6$.

Temp. (K)	Pressure (torr)	Velocity (cm/s)	Re	$k_{obs} \pm 2\sigma$ (10^{-13} cm^3s^{-1})	Correction Factor	$k \pm 2\sigma$ (10^{-13} cm^3s^{-1})
293	70	1649	2714	2.02 ± 0.14	1.13	2.29 ± 0.16
292	87	1763	3637	1.75 ± 0.07	1.13	1.97 ± 0.08
293	140	1667	5502	1.88 ± 0.18	1.12	2.10 ± 0.20
242	71	1747	4136	0.84 ± 0.04	1.12	0.95 ± 0.05
239	145	1787	8902	1.04 ± 0.15	1.11	1.15 ± 0.16

The rate constants we have determined for reaction 3 are in good agreement with the accepted literature values. Figure 4 contains a comparison between our experimentally determined rate constants and the values recommended by *DeMore et al.* [1992]. The good agreement between our experimental values and the literature values led us to conclude that our system did not suffer from large systematic errors and that the numerically generated correction factors were reasonably accurate.

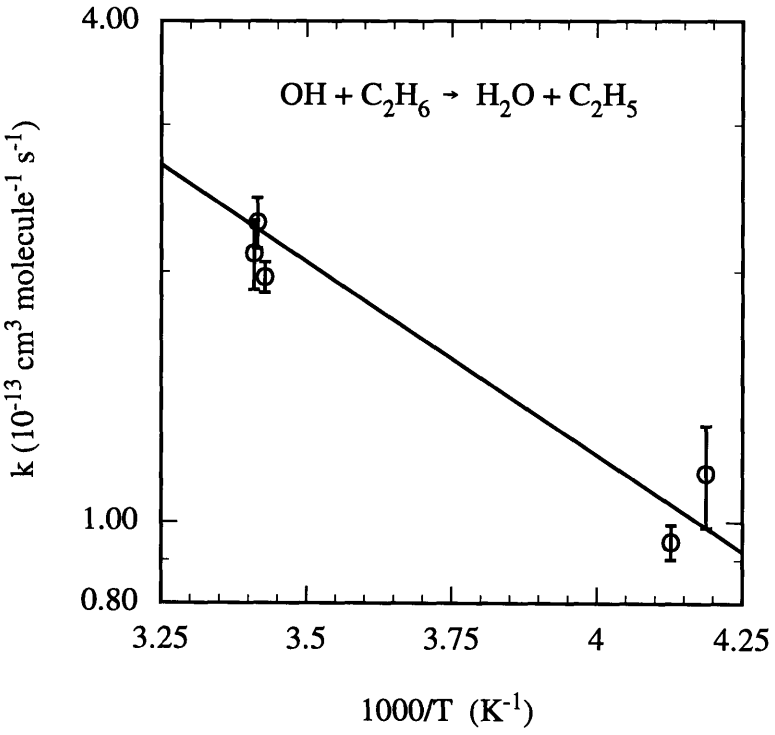

Figure 4. Comparison of our experimentally determined reaction rate constants for OH + C_2H_6 (circles) with the values recommended by *DeMore et al.* [1992] (solid line).

VI.4.2 Reaction with Hydrogen Peroxide

Experimental Results

The reaction of OH with hydrogen peroxide was studied at temperatures between 245 and 297 K. Temperatures were kept above 245 K to avoid condensation of hydrogen peroxide. In all conditions, plots of *ln* [OH] vs. *z* were linear (see figure 5) indicating that side reactions were minimal.

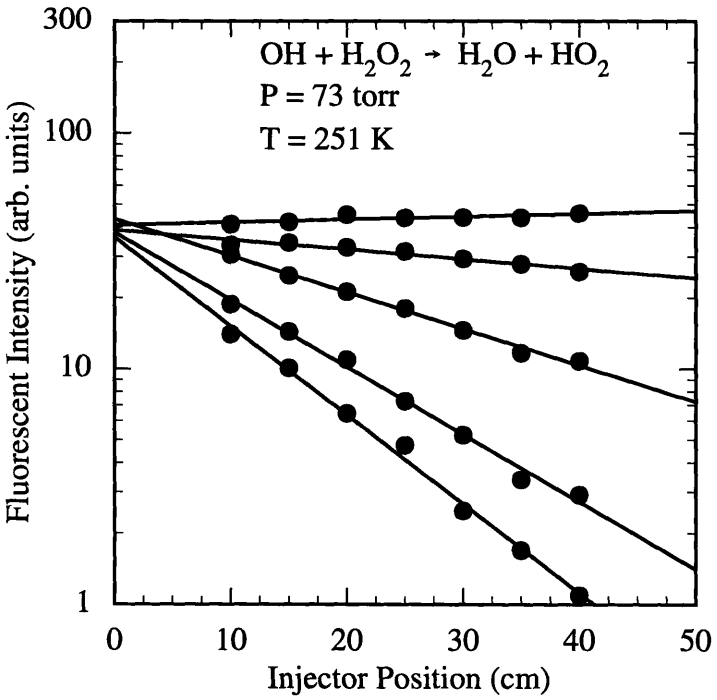

Figure 5. Typical plots of *ln* [OH] vs. injector position for reaction 1.

Plots of k^I_{obs} vs. [H_2O_2] were also linear at each temperature of this study indicating that secondary reactions and condensation of H_2O_2 were minimal. Figure 6 contains a typical plot.

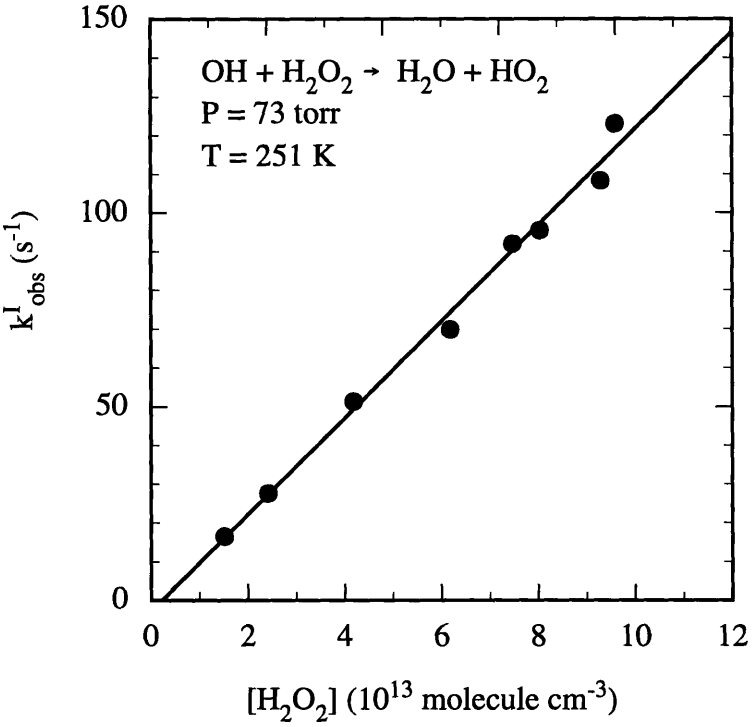

Figure 6. Typical plots of k^{I}_{obs} vs. $[H_2O_2]$ for reaction 1.

The values of k_{obs} were multiplied by a correction factor generated using our numerical model (see section VI.3). It was assumed that the magnitude of the correction factor was a function of *Re* only. Table II contains a summary of the bimolecular rate constants determined at various temperature settings. Near room temperature we obtained an average value of $(1.58 \pm 0.15) \times 10^{-12}$ cm^3 molecule^{-1} s^{-1} for the rate constant. As the temperature is lowered, we observed only a small decrease in the rate constant. Within experimental error we did not observe that the rate constant had a pressure dependence.

Table II. Summary of experimentally determined bimolecular rate constants for OH + H_2O_2.

Temp. (K)	Pressure (torr)	Velocity (cm/s)	Re	$k_{obs} \pm 2\sigma$ (10^{-12} cm^3s^{-1})	Correction Factor	$k \pm 2\sigma$ (10^{-12} cm^3s^{-1})
297	79	1863	3381	1.35 ± 0.11	1.13	1.52 ± 0.12
297	141	1594	5165	1.46 ± 0.16	1.12	1.63 ± 0.18
290	75	1815	3266	1.39 ± 0.06	1.13	1.57 ± 0.07
280	150	1466	5626	1.43 ± 0.18	1.12	1.59 ± 0.22
279	76	1805	3531	1.19 ± 0.10	1.13	1.34 ± 0.12
278	64	1686	2797	1.24 ± 0.11	1.13	1.41 ± 0.13
267	72	1751	3518	1.34 ± 0.07	1.13	1.51 ± 0.09
266	77	1651	3573	1.32 ± 0.05	1.13	1.49 ± 0.07
265	147	1389	5776	1.35 ± 0.14	1.12	1.51 ± 0.18
262	68	1773	3485	1.07 ± 0.09	1.13	1.21 ± 0.12
257	147	1495	6579	1.43 ± 0.07	1.11	1.60 ± 0.09
251	73	1632	3727	1.22 ± 0.06	1.13	1.37 ± 0.09
250	145	1473	6730	1.29 ± 0.16	1.11	1.44 ± 0.22
245	76	1649	4101	1.27 ± 0.13	1.12	1.43 ± 0.17

The Arrhenius parameters for reaction 1 were determined to be $A = 2.45 \pm 0.71 \times 10^{-12}$ cm^3 $molecule^{-1}$ s^{-1} and that $E/R = 138 \pm 93$ K (see figure 7).

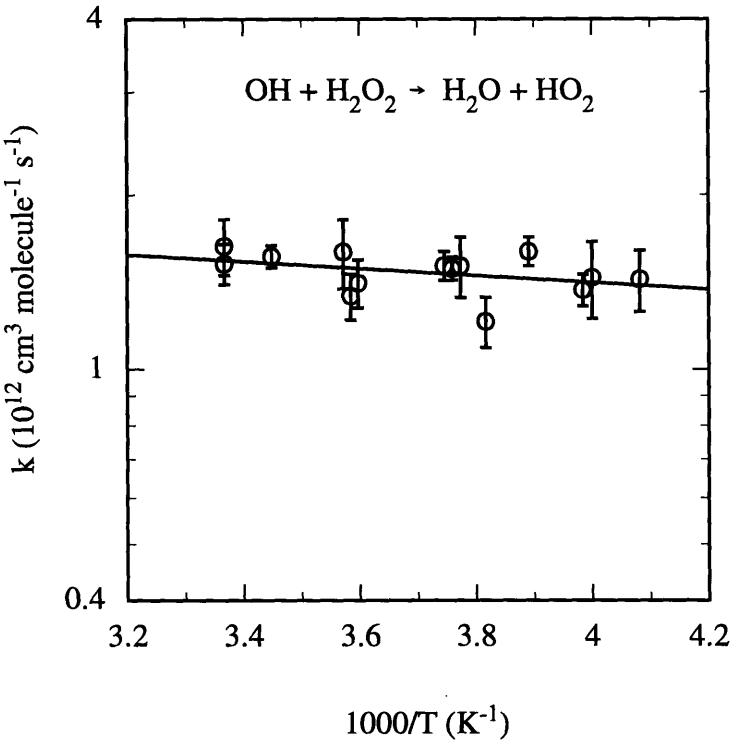

Figure 7. Arrhenius plot for OH + H_2O_2. The line represents a least-squares fit to the data points.

Comparison with Previous Results

The rate constant of reaction 1 has previously been determined over the temperature range of this study. The majority of these investigations have reported a slight decrease in the reaction rate constant as the temperature is lowered. However, *Lamb et al.* [1983] observed an increase in the rate constant with decreasing temperature when the temperature is below 298 K. Detailed evaluations of all of the previous investigations of reaction 1 can be found in the literature [*Atkinson et al.*, 1989; *DeMore et al.*, 1992]. Table III contains a summary of these studies.

Table III. Summary of previous experimental results for $OH + H_2O_2$.

k at 298 K ($10^{-12}cm^3s^{-1}$)	A ± 1σ ($10^{-12}cm^3s^{-1}$)	E / R ± 1σ (K)	Temp. Range (K)	Method	Reference
1.64 ± 0.32	2.51 ± 0.60	126 ± 76	245–423	Flow Tube	Keyser [1980]
1.69 ± 0.26	2.96 ± 0.50	164 ± 52	250–459	Flow Tube	Sridharan et al. [1980]
1.59 ± 0.08	3.7 ± 0.6	260 ± 50	273–410	Flash Photolysis	Wine et al. [1981a]
1.79 ± 0.14	2.91 ± 0.30	161 ± 32	250–370	Flash Photolysis	Kurylo et al. [1982a]
1.80 ± 0.30	1.47 ± 0.20	-70 ± 41	241–413	Flash Photolysis	Lamb et al. [1983]
1.86 ± 0.18	2.76 ± 0.80	110 ± 60	273–410	Flash Photolysis	Vaghjiani et al. [1989]
1.7	2.9	160 ± 100	240–460	Review Evaluation	Demore et al. [1992]
1.58 ± 0.15	2.45 ± 0.71	138 ± 93	245–297	Turbulent Flow	This Work

The value we obtained for the room temperature rate constant is slightly lower (< 10%) than observed in the previous studies. However, our value for the activation energy is in reasonable agreement with those determined in most of the previous studies. Figure 8 contains a comparison of our rate constants along with an Arrhenius plot of the values recommended by *DeMore et al.* [1992]. Although our data is approximately 10% lower at all temperatures, our results closely match the relative temperature dependence of the recommended values.

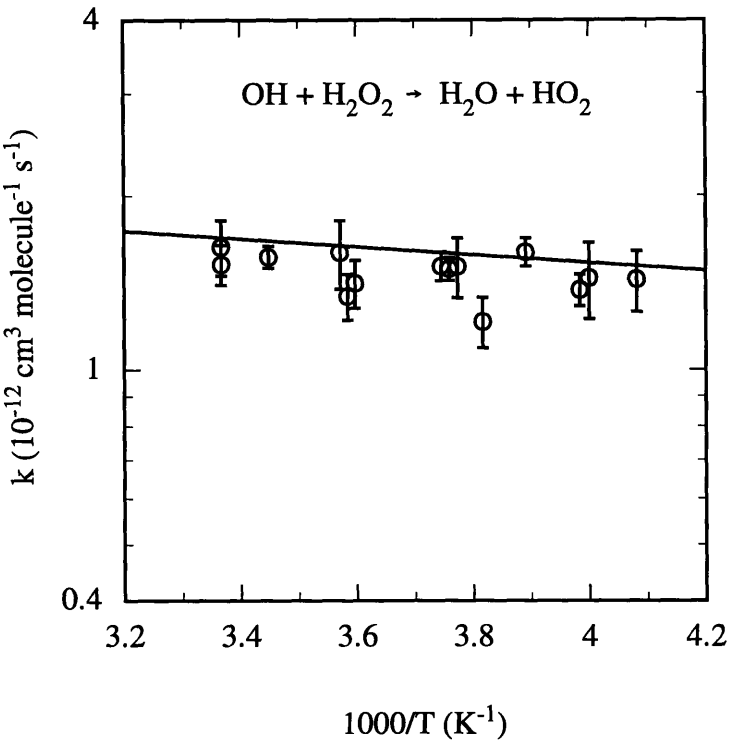

Figure 8. Comparison of our experimentally determined reaction rate constants for OH + H_2O_2 (circles) with the values recommended by *DeMore et al.* [1992] (solid line).

The reason for the negative deviation of our results is uncertain. A potential cause of this discrepancy may be the value used for the cross section of H_2O_2 at 213.9 nm. *Vaghjiani et al.* [1989] reported a cross section approximately 8% higher than the one used for this study. If we use their value, our rate constants would be increased by 8% placing them in close agreement with the recommended values.

VI.4.3 Reaction with Nitric Acid

Experimental Results

Reaction 2 was studied at temperatures between 235 and 293 K and pressures from 49 to 298 torr. At all pressures and temperatures, plots of *ln* [OH] *vs. z* and k^I_{obs} *vs.* [HNO_3] were linear indicating that side reactions were minimal and that condensation of nitric acid on the flow tube walls was not substantial. Figures 9 and 10 contain typical plots of *ln* [OH] *vs. z* and k^I_{obs} *vs.* [HNO_3] observed for reaction 2.

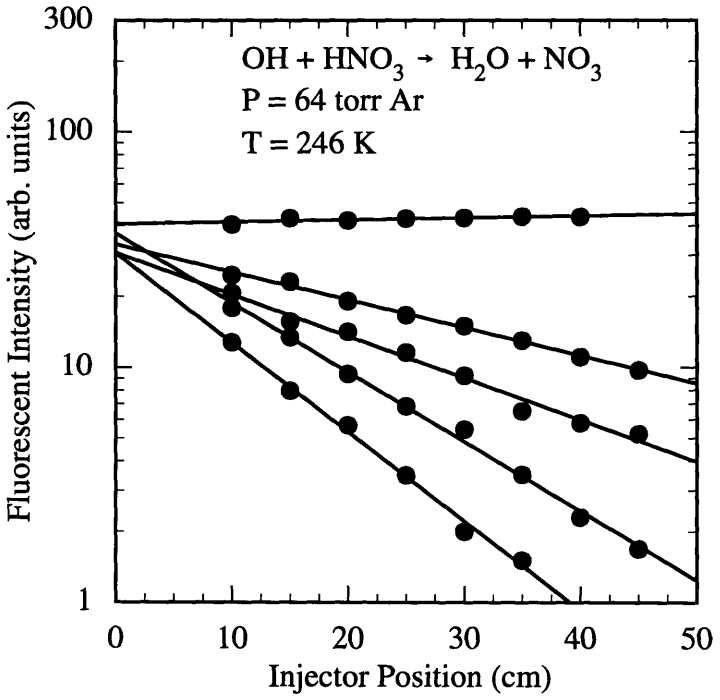

Figure 9. Typical plots of *ln* [OH] vs. injector position for reaction 2.

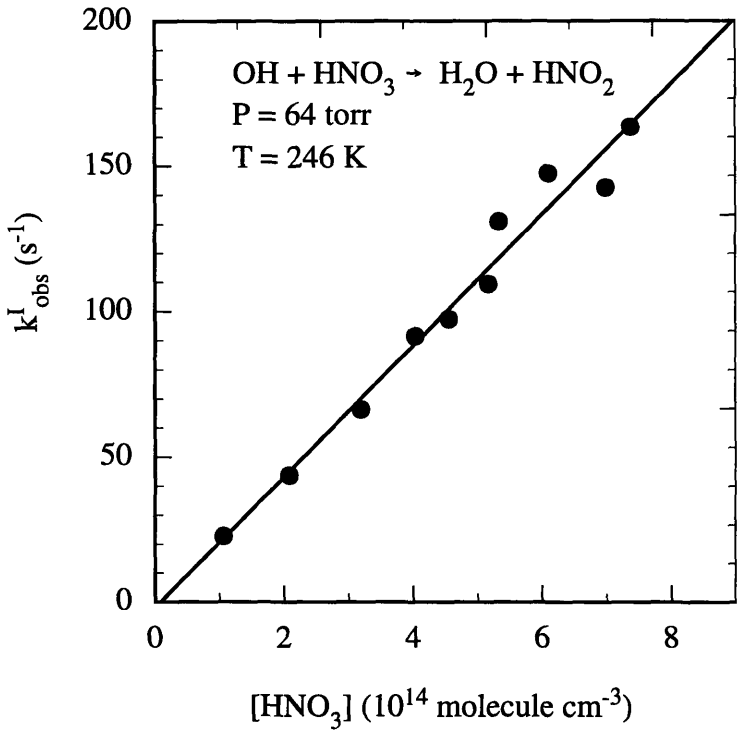

Figure 10. Typical plots of k^{I}_{obs} vs. [HNO_3] for reaction 2.

The values of k_{obs} were multiplied by a correction factor generated using our numerical model (see section VI.3). It was assumed that the magnitude of the correction factor was a function of *Re* only.

Table IV contains a summary of the bimolecular rate constants determined for reaction 2. Near room temperature we found that the rate constant possessed a slight pressure dependence: the rate constant was observed to increase by approximately 20% when the pressure was raised from 50 to 200 torr. As the temperature was lowered, the rate constant was observed to increase in magnitude and also to be increasingly sensitive to the total pressure. At temperatures near 240 K the rate constant was found to increase by approximately 45% when the pressure was raised from 50 to 200 torr. Unfortunately, the scatter in the data obtained at pressures greater than 100 torr makes it difficult to accurately assess the pressure dependence of reaction 2. The increase in the variance of our data is

largely a result of the decrease in OH detection sensitivity that occured when the pressure is raised.

Table IV. Summary of experimentally determined bimolecular rate constants for OH + HNO_3.

Temp. (K)	Pressure (torr)	Velocity (cm/s)	Re	$k_{obs} \pm 2\sigma$ (10^{-13} cm^3s^{-1})	Correction Factor	$k \pm 2\sigma$ (10^{-13} cm^3s^{-1})
293	49	1673	1926	1.09 ± 0.10	1.14	1.24 ± 0.11
292	67	1793	2854	1.13 ± 0.09	1.13	1.28 ± 0.10
293	76	1634	2924	1.13 ± 0.09	1.13	1.28 ± 0.10
292	93	1602	3521	0.99 ± 0.12	1.13	1.12 ± 0.14
293	110	1422	3683	1.05 ± 0.11	1.13	1.18 ± 0.12
291	118	1630	4581	1.23 ± 0.08	1.12	1.38 ± 0.09
292	152	1626	5866	1.34 ± 0.06	1.12	1.49 ± 0.07
291	160	1666	6357	1.37 ± 0.05	1.11	1.53 ± 0.05
291	200	1501	7146	1.33 ± 0.08	1.11	1.48 ± 0.09
291	298	1185	8397	1.34 ± 0.11	1.11	1.48 ± 0.12
286	109	1607	4320	1.16 ± 0.04	1.12	1.31 ± 0.05
272	70	1896	3579	1.22 ± 0.04	1.13	1.38 ± 0.05
277	77	1521	3066	1.16 ± 0.07	1.13	1.31 ± 0.08
273	137	1709	6273	1.46 ± 0.07	1.11	1.62 ± 0.08
272	154	1555	6457	1.59 ± 0.04	1.11	1.78 ± 0.05
271	188	1419	7244	1.80 ± 0.09	1.11	2.00 ± 0.10
273	281	1177	8839	1.51 ± 0.14	1.11	1.67 ± 0.15
263	55	1865	2952	1.57 ± 0.09	1.13	1.78 ± 0.10
261	63	1824	3339	1.39 ± 0.13	1.13	1.57 ± 0.15
261	128	1589	5909	1.73 ± 0.21	1.12	1.93 ± 0.23
262	192	1569	8685	1.93 ± 0.04	1.11	2.14 ± 0.05
261	284	1135	9384	1.91 ± 0.14	1.11	2.11 ± 0.16

Table IV (cont.). Summary of experimentally determined bimolecular rate constants for OH + HNO_3.

Temp. (K)	Pressure (torr)	Velocity (cm/s)	Re	$k_{obs} \pm 2\sigma$ (10^{-13} cm^3s^{-1})	Correction Factor	$k \pm 2\sigma$ (10^{-13} cm^3s^{-1})
255	74	1629	3643	1.63 ± 0.14	1.13	1.84 ± 0.16
251	82	1629	4186	1.83 ± 0.05	1.12	2.06 ± 0.06
251	126	1656	6542	1.80 ± 0.12	1.12	2.01 ± 0.13
251	135	1611	6779	2.21 ± 0.19	1.11	2.45 ± 0.21
255	144	1559	6845	2.17 ± 0.15	1.11	2.41 ± 0.17
257	151	1704	7684	1.65 ± 0.21	1.11	1.84 ± 0.23
257	168	1605	8090	2.37 ± 0.31	1.11	2.63 ± 0.34
255	187	1294	7376	1.97 ± 0.32	1.11	2.19 ± 0.35
255	253	1103	8473	2.17 ± 0.14	1.11	2.41 ± 0.16
243	57	2041	3857	1.66 ± 0.07	1.13	1.87 ± 0.08
248	57	1909	3485	1.62 ± 0.10	1.18	1.91 ± 0.12
246	64	1863	3895	2.24 ± 0.18	1.13	2.52 ± 0.20
246	84	1642	4471	2.00 ± 0.19	1.12	2.24 ± 0.21
246	111	1654	5975	2.30 ± 0.12	1.12	2.56 ± 0.13
245	190	1273	7919	2.04 ± 0.24	1.11	2.27 ± 0.27
241	51	2118	3650	2.01 ± 0.18	1.13	2.27 ± 0.20
241	62	1606	3356	1.98 ± 0.05	1.13	2.24 ± 0.05
240	84	2005	5725	2.24 ± 0.15	1.12	2.50 ± 0.17
241	97	1682	5510	2.35 ± 0.19	1.12	2.62 ± 0.21
241	100	1744	5897	2.29 ± 0.14	1.12	2.56 ± 0.16
240	136	1500	6949	2.57 ± 0.18	1.11	2.86 ± 0.20
241	140	1653	7801	2.18 ± 0.16	1.11	2.42 ± 0.17
240	149	1782	9005	2.64 ± 0.26	1.11	2.92 ± 0.29
239	183	1511	9495	3.12 ± 0.47	1.11	3.45 ± 0.52
239	187	1629	10455	2.98 ± 0.30	1.10	3.29 ± 0.34
238	196	1649	11127	2.96 ± 0.66	1.10	3.26 ± 0.73
235	112	1909	7578	2.37 ± 0.15	1.11	2.63 ± 0.17

Arrhenius plots were made in order to quantitate the negative temperature dependence of reaction 2 (see figure 11). We obtained the following values for the activation energy: for $P < 100$ torr the activation energy was given by $E / R = -909$ K, for

100 torr < P < 150 torr the activation energy was given by E / R = -1001 K, and for P > 150 torr the activation energy was given by E / R = -955 K.

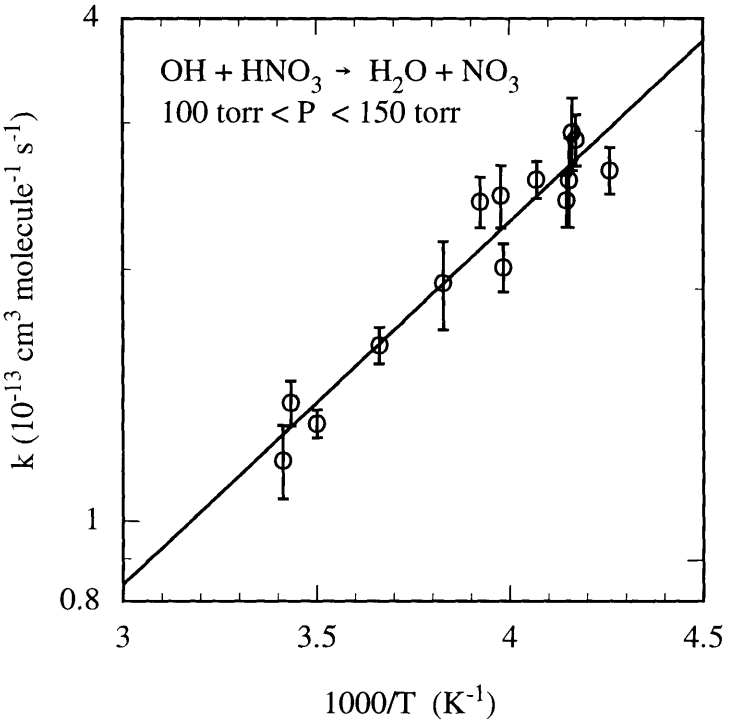

Figure 11. Arrhenius plot for reaction 2 for data obtained in pressures between 100 and 150 torr. The line represents a least-squares fit to the data points.

Comparison with Previous Results

The results obtained from previous investigations of reaction 2 are summarized in table V. Early studies [pre-1980] reported a temperature and pressure independent rate constant of approximately 0.8 x 10^{-13} cm^3 $molecule^{-1}$ s^{-1} [*Smith and Zellner*, 1975; *Margitan et al.*, 1975]. In 1981 *Wine et al.* [1981b] reported a 50% higher room temperature value and negative temperature dependence. Six subsequent studies have corroborated their results [*Jourdain et al,* 1982; *Marinelli and Johnston*, 1982; *Kurylo et al.,* 1982b; *Margitan and Watson*, 1982; *Smith et al.,* 1984; *Stachnik et al.*, 1986]. Three relatively recent studies have reported room temperature values similar to those of the early studies, while still observing a negative temperature dependence [*Devolder et al.*, 1984; *Connell and Howard*, 1985; *Jolly et al.,* 1985]. In order to explain the negative temperature dependence *Lamb et al.* [1984] developed a double transition state model which maintains that reaction 2 proceeds through a stable intermediate complex. Their model also predicts that reaction 2 should have a rate constant which increases with increasing pressure (especially at low temperatures). However, only two of the twelve previously mentioned studies [*Margitan and Watson*, 1982; *Stachnik et al.*, 1986] have observed a pressure dependence. Despite the large number of studies that did not observe a pressure dependent rate constant, *DeMore et al.* [1992] have recommended the following pressure dependent expression for the rate constant

$$k(M,T) = k_0 + \frac{k_3\,[M]}{1 + \frac{k_3\,[M]}{k_2}} \qquad (1)$$

where [M] is the total concentration of all flow tube species, $k_0 = 7.2 \times 10^{-15} \exp(785/T)$ cm^3 $molecule^{-1}$ s^{-1}, $k_2 = 4.1 \times 10^{-16} \exp(1440/T)$ cm^3 $molecule^{-1}$ s^{-1}, and $k_3 = 1.9 \times 10^{-33}$ $\exp(725/T)$ cm^6 $molecule^{-2}$ s^{-1}.

Table V. Summary of previous investigations of the reaction OH + HNO_3.

$k \pm 2\sigma$ near 295K (10^{-13} cm^3 s^{-1})	E / R (K)	Pressure Dependence?	Method	Reference
0.80 ± 0.20	0	No	Flash Photolysis	Smith and Zellner [1975]
0.89 ± 0.13	0	No	Flow Tube	Margitan et al. [1975]
1.25 ± 0.28	- 649 ± 69	No	Flash Photolysis	Wine et al. [1981b]
1.25 ± 0.07	- 877 ± 85	No	Flow Tube	Jourdain et al. [1982]
1.31 ± 0.24	- 644 ± 79	No	Flash Photolysis	Marinelli and Johnston [1982]
1.38 ± 0.20	- 759 ± 100	No	Flash Photolysis	Kurylo et al. [1982b]
1.08 at 20 torr 1.30 at 300 torr	- 700 at 0 torr - 800 at 40 torr	Yes	Flash Photolysis	Margitan and Watson [1982]
0.93 ± 0.10	- 843	No	Flow Tube	Devolder et al. [1984]
1.40 ± 0.20	- 850	No	Flash Photolysis	Smith et al. [1984]
0.77 ± 0.04		No	Flash Photolysis	Jolly et al. [1985]
0.85 ± 0.30	- 430 ± 60	No	Flow Tube	Connell and Howard [1985]
1.11 at 10 torr 1.54 at 730 torr	- 710 at 0 torr - 1165 at high P	Yes	Flash Photolysis	Stachnik et al [1986]
1.24 at 49 torr 1.48 at 298 torr	~950	Yes	Turbulent Flow	This Work

At room temperature our results lie within 1.12 x 10^{-13} cm^3 $molecule^{-1}$ s^{-1} and 1.53 x 10^{-13} cm^3 $molecule^{-1}$ s^{-1}, in good agreement with the higher values obtained by *Wine et al.* and the six corroborating studies. Our estimate of the activation energy (~ -950 K) is in good agreement with the values obtained by *Stachnik et al.* and slightly lower than those reported in the rest of the investigations. The rate constant expression of *DeMore et al.* (equation 1) provides a reasonably good fit to our data. Figure 12 contains a comparison

between our experimentally determined rate constants obtained at temperatures near 292 and 261 K and the respective values predicted using equation 1.

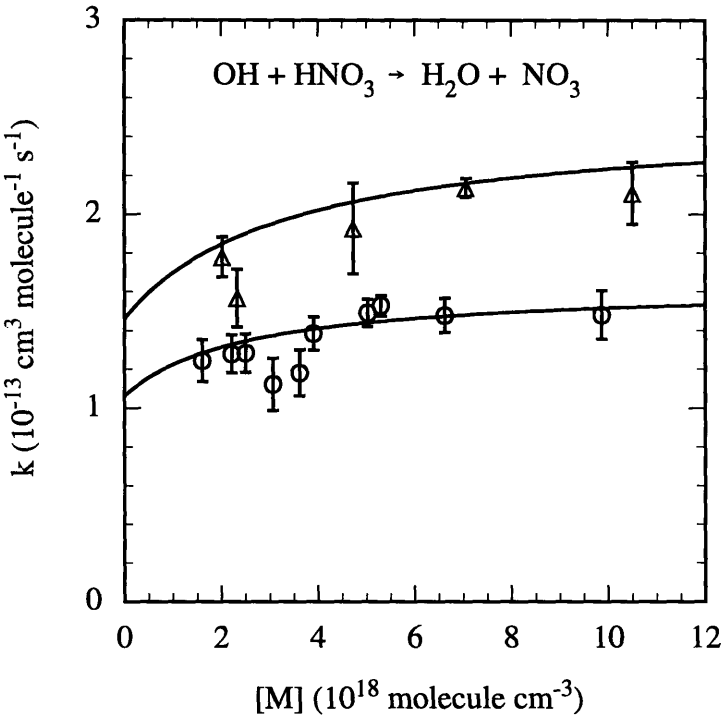

Figure 12. Experimental values of k obtained at temperatures near 292 K (circles) and near 261 K (triangles) for the reaction of OH + HNO_3. Also plotted are the values predicted using equation 1 with T = 292 K and T= 261 K (solid lines).

VI.5 Chapter Conclusions

The turbulent flow tube technique has been used to study the temperature and pressure dependence of three bimolecular reactions involving the OH radical. Rate constants determined for the reaction of OH + C_2H_6 have been found to be in excellent agreement with accepted literature values. Rate constants determined for the reaction of OH + H_2O_2 have been found to be independent of pressure and to slightly decrease with

decreasing temperature. The observed temperature dependence of the hydrogen peroxide reaction is in good agreement with the recommendation of *DeMore et al.* [1992]. Finally, the rate constant of the reaction of OH + HNO_3 has been shown to have a negative temperature dependence and a pressure dependence. These findings indicate that an intermediate complex is formed. Our results are in good agreement with the experimental results of *Margitan and Watson* [1982] and *Stachnik et al.* [1986], the theoretical findings of *Lamb et al.* [1984], and the review evaluation of *DeMore et al.* [1992].

References for Chapter VI

Atkinson, R., D. L. Baulch, R. A. Cox, R. F. Hampson, J. A. Kerr, and J. Troe, Evaluated kinetic and photochemical data for atmospheric chemistry: supplement III, *J. Phys. Chem. Ref. Data, 18*, 881, 1989.

Connell, P. S., and C. J. Howard, Kinetics study of the reaction HO + HNO_3, *Int. J. Chem. Kinet., 17,* 17, 1985.

DeMore, W. B., S. P. Sander, C. J. Howard, A. R. Ravishankara, D. M. Golden, C. E. Kolb, R. F. Hampson, M. J. Kurylo, and M. J. Molina, *Chemical kinetics and photochemical data for use in stratospheric modeling, JPL Publication 92-20*, 1992.

Devolder, P., M. M. Carlier, J. F. Pauwels, and L. R. Sochet, Rate constant for the reaction of OH with nitric acid: a new investigation by discharge flow resonance fluorescence, *Chem. Phys. Lett., 111,* 94, 1984.

Jolly, G. S., G. Paraskevopoulos, and D. L. Singleton, The question of a pressure effect in the reaction OH + HNO_3. A laser flash-photolysis resonance-absorption study, *Chem. Phys. Lett., 117*, 132, 1985.

Jourdain, J. L., G. Poulet, and G. LeBras, Determination of the rate parameters and products for the reaction of hydroxyl radicals with nitric acid, *J. Chem. Phys., 76*, 5827, 1982.

Keyser, L. F., Absolute rate constant of the reaction OH + $H_2O_2 \rightarrow HO_2 + H_2O$ from 245 to 423 K, *J. Phys. Chem., 84*, 1659, 1980.

Kurylo, M. J., J. L. Murphy, G. S. Haller, and K. D. Cornett, A flash photolysis resonance fluorescence investigation of the reaction OH + $H_2O_2 \rightarrow HO_2 + H_2O$, *Int. J. Chem. Kinet., 14*, 1149, 1982a.

Kurylo, M. J., K. D. Cornett, and J. L. Murphy, The temperature dependence of the rate constant for the reaction of hydroxyl radicals with nitric acid, *J. Geophys. Res., 87*, 3081, 1982b.

Lamb, J. J., L. T. Molina, C. A. Smith, and M. J. Molina, Rate constant of the OH + $H_2O_2 \rightarrow HO_2 + H_2O$ reaction, *J. Phys. Chem., 87*, 4467, 1983.

Lamb, J. J., M. Mozurkewich, and S. W. Benson, Negative activation energies and curved Arrhenius plots. 3. OH + HNO_3 and OH + HNO_4, *J. Phys. Chem., 88*, 6441, 1984.

Margitan, J. J., and R. T. Watson, Kinetics of the reaction of hydroxyl radicals with nitric acid, *J. Phys. Chem., 86*, 3819, 1982.

Margitan, J. J., F. Kaufman, and J. G. Anderson, Kinetics of the Reaction OH + $HNO_3 \rightarrow H_2O_2 + NO_3$, *Int. J. Chem. Kinet. Symp., 1,* 281, 1975.

Marinelli, W. J., and H. S. Johnston, Reaction rates of hydroxyl radical with nitric acid and with hydrogen peroxide, *J. Chem. Phys., 77*, 1225, 1982.

Reid, R. C., J. M. Prausnitz and T. K. Sherwood, *The Properties of Gases and Liquids, 4th ed.,* McGraw-Hill, New York, 1987.

Smith, C. A., L. T. Molina, J. J. Lamb, and M. J. Molina, Reaction of OH with nitric acids, *Int. J. Chem. Kinet., 16*, 41, 1984.

Smith, I. W. M., and R. Zellner, Rate measurements of OH by resonance absorption. IV. reactions of OH with NH_3 and HNO_3, *Int. J. Chem. Kinet. Symp., 1*, 341, 1975.

Sridharan, U. C., B. Reimann, and F. Kaufman, Kinetics of the reaction OH + $H_2O_2 \rightarrow$ HO_2 + H_2O, *J. Chem. Phys., 73,* 1286, 1980.

Stachnik, R. A., L. T. Molina, and M. J. Molina, Pressure and temperature dependences of the reaction of OH with nitric acid, *J. Phys. Chem., 90,* 2777, 1986.

Vaghjiani, G. L., and A. R. Ravishankara, Reactions of OH and OD with H_2O_2 and D_2O_2, *J. Phys. Chem., 93*, 7833, 1989.

Wine, P. H., A. R. Ravishankara, N. M. Kreutter, R. C. Shah, J. M. Nicovich, R. L. Thompson, and D. J. Wuebbles, Rate of reaction of OH with HNO_3, *J. Geophys. Res., 86*, 1105, 1981a.

Wine, P. H., D. H. Semmes, and A. R. Ravishankara, A laser flash photolysis kinetics study of the reaction OH + $H_2O_2 \rightarrow$ HO_2 + H_2O, *J. Chem. Phys., 75*, 4390, 1981b.

Chapter VII: Conclusions and Current Directions

VII.1 Conclusions from Previous Studies

In the previous chapters, we have shown that operating a standard flow tube system in the turbulent flow regime allows the rate constants of gas phase reactions to be accurately determined under a wide range of temperatures and pressures. This finding represents a substantial advance for experimental flow tube kinetics. We believe that the turbulent flow tube technique will allow the pressure and temperature dependencies of many bimolecular, termolecular and complex mode reactions to be more fully characterized.

The turbulent flow tube technique also has potential applications outside the realm of neutral gas phase reaction studies. For example, this technique is ideal for studying ion-molecule reactions because reactant collisions with the flow tube walls are minimized. Another example is the study of heterogeneous reactions occurring on small aerosols. The higher operating pressures of the turbulent flow tube technique would allow small particles to be suspended in the flow with minimal interactions with the walls.

In this thesis, we have shown that many of the key features of low pressure flow tube systems, such as microwave discharges, titration reactions, and resonance fluorescence detection, can be used at the higher operating pressures of the turbulent flow tube technique. However, we believe that several of the powerful detection techniques available to low pressure flow tube systems, such as magnetic resonance and mass spectrometry, will require modification to be implemented at higher pressures.

VII.2 Preliminary Results from Mass Spectrometry Studies

VII.2.1 Introduction

We are currently attempting to develop a mass spectrometric technique with the capability of detecting low concentration levels (i.e., < 10^{10} molecule cm^{-3}) of gas phase species at the higher pressures of turbulent flow. Initially, we focused on mass spectrometers with molecular beam sampling and electron impact ionization. Such a system was constructed in our laboratory by J. T. Jayne in 1992 and is described in *Zhang et al.* [1994]. This system provided excellent sensitivity at low flow tube pressures (P ~ 1 torr) but less than adequate sensitivity at flow tube pressures greater than 100 torr. Our focus then shifted to systems which ionize at higher pressures (i.e. flow tube pressures) instead of the ultra-high vacuum pressures necessary for electron impact ionization. The main benefit of ionizing at high pressure is that ions can be focused with electrostatic or quadrupole lenses at each pumping stage. This process leads to an enrichment in the ion content of the gas passing into the mass analyzing quadrupole chamber.

High pressure ionizing mass spectrometer systems have been previously shown to be capable of detecting extremely low levels of gas phase species at total pressures as high as one atmosphere. *McLuckey et al.* [1988] have created an atmospheric sampling glow discharge ion source which when coupled to a mass spectrometer is capable of detecting certain gas phase species at concentrations as low as 2 x 10^7 molecule cm^{-3}. *Eisele and Tanner* [1991] developed an atmospheric pressure chemical ionization technique for the specific purpose of measuring the concentration of OH in the atmosphere. With this technique they have been able to detect OH concentrations below 1 x 10^6 molecule cm^{-3}. *Eisele and Berresheim* [1992] have created a high-pressure chemical ionization mass spectrometer designed to monitor gas chromatography effluent. Their system has been shown to be capable of detecting several gas phase species at concentrations as low as 1 x 10^7 molecule cm^{-3}. *Mohler et al.* [1993] have created a high pressure chemical ionization

mass spectrometer which is mounted in an airplane for the in situ detection of trace atmospheric species. With their instrument they estimate that several trace species can be detected with concentrations as low as 1 x 10^7 molecule cm^{-3}.

In the remainder of this chapter, we will present the preliminary results of our current effort to develop a high pressure ionizing mass spectrometer which can eventually be coupled to a flow tube system. Our research up to this point has been devoted to studying possible ion-molecule reaction schemes which will allow HCl and Cl_2 to be detected at low concentration levels.

VII.2.2 Experimental Details

A schematic of the chemical ionization source used for these studies is depicted in figure 1. Nitrogen from a liquid nitrogen tank was injected into a stainless steel tube (15 cm long, 10 mm i.d.) which served as the flow tube for the ion-molecule reactions. The average velocity of the nitrogen carrier gas was approximately 700 cm s^{-1} (Re ~ 5000). Ions were initially formed by passing the N_2 flow over a corona discharge. The corona discharge was formed between the tip of a sewing needle and the electrically grounded stainless steel tube. A needle voltage of -3 kV resulted in a stable discharge with a current of approximately 25 μA. The needle was mounted on the end of a piece of Pyrex tubing (40 cm long, 3 mm o.d.) which could be moved along the axis of the stainless steel tube, allowing the ion-molecule reaction time to be varied. The downstream end of the stainless steel tube was positioned within 0.5 cm of the front aperture of the mass spectrometer. The flow tube effluent was exhausted into the laboratory atmosphere.

For several experiments, trace quantities of SF_6 were mixed in with the main carrier gas before being injected into the tube. The quantity of SF_6 injected into the flow was monitored with a mass flow meter. Permeation tubes were used to deliver small amounts of Cl_2 or HCl. The permeation tube was placed at the upstream end of a 60 cm long dilution cell. A flow of nitrogen was passed over the permeation tube. At the downstream

end of the cell, a portion of the flow was diverted through a pressure release valve, while the remainder of the flow was passed through a mass flowmeter and into the ion flow tube. The quantity of trace species injected into the flow tube was varied by keeping the total flow through the dilution cell constant while varying the fraction injected into the flow tube. The injection point of HCl or Cl_2 was 7.5 cm from the downstream end of the ion flow tube. Chlorine was obtained from Dynacal Permeation Devices as a liquid encased in a 1,280 ng min^{-1} permeation tube. Hydrochloric acid was also obtained from Dynacal Permeation Devices in a 1,100 ng min^{-1} permeation tube.

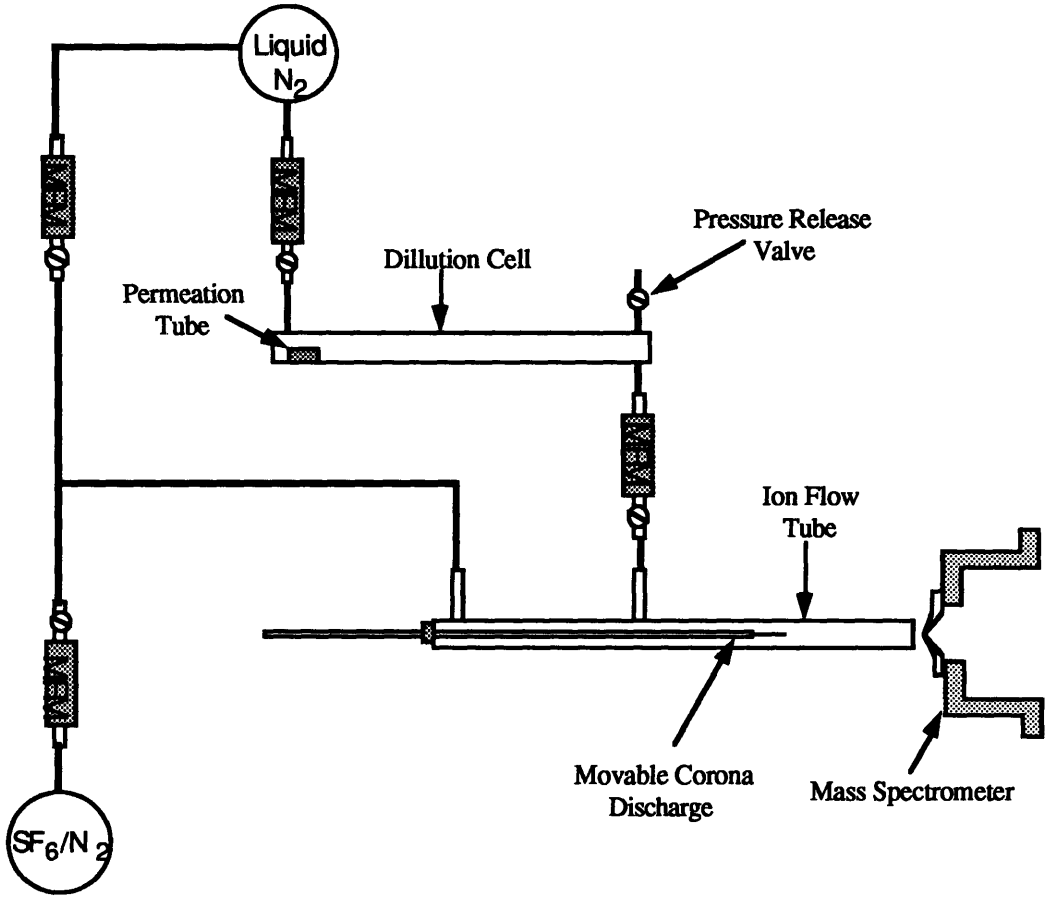

Figure 1. Schematic of the chemical ionization source.

The mass spectrometer used for this study was a modified Extrel atmospheric pressure ionization mass spectrometer system (see figure 2) configured for monitoring negative ions. The sampled ions first passed through the front aperture into the declustering region. The front aperture also served as the first of three declustering lenses which were used to focus and accelerate the negative ions. We found that high ion intensities could be obtained when the voltage of the front aperture lens was maintained at -200 V, the second lens at -188 V, and the last lens at -121 V. The pressure in the declustering region was typically kept at 3 torr with a 600 L min^{-1} rotary pump.

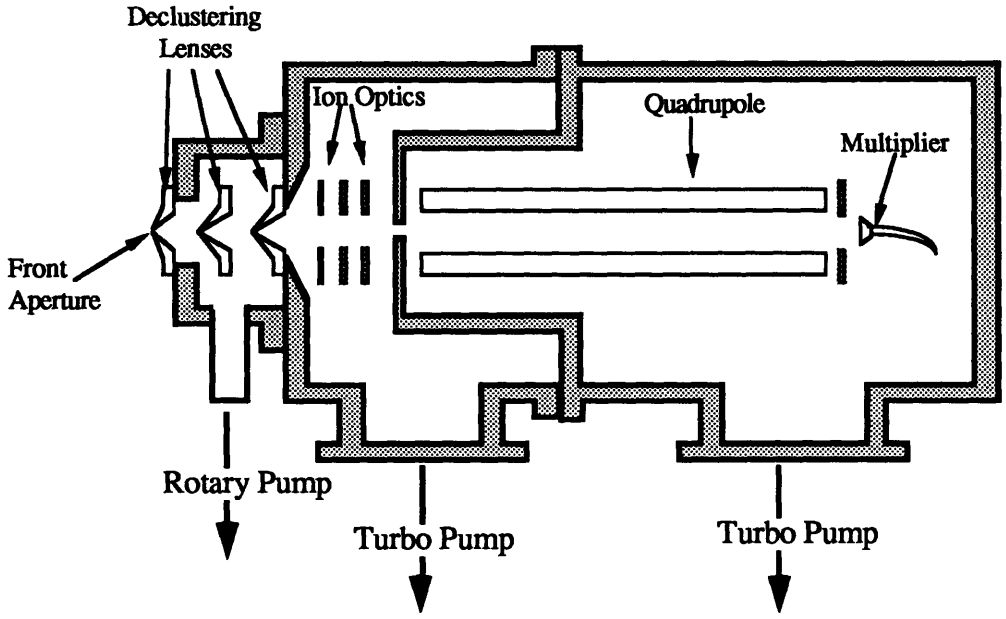

Figure 2. Schematic of high pressure ionizing mass spectrometer system.

The sampled ions then passed into a two stage high vacuum chamber. The first vacuum stage contained several ion lenses and was pumped by a turbomolecular pump (520 L s^{-1}) which maintained the pressure at approximately 4 x 10^{-4} torr. The second stage contained the quadrupole mass filter and was pumped by a turbomolecular pump (520 L s-

1) which maintained the pressure at approximately 2 x 10^{-6} torr. Both turbomolecular pumps were backed by a 300 L min^{-1} rotary pump. The quadrupole had 1.9 cm diameter poles and a mass range of 2 to 300 amu. The power supplies and operating electronics for the quadrupole mass spectrometer were provided by Extrel as part of their C-50 mass spectrometer system.

VII.2.3 Results and Discussion

Description of Observed Spectra

Figure 3 shows a spectrum obtained with only N_2 flowing down the tube and with the needle 2 cm upstream of the front aperture.

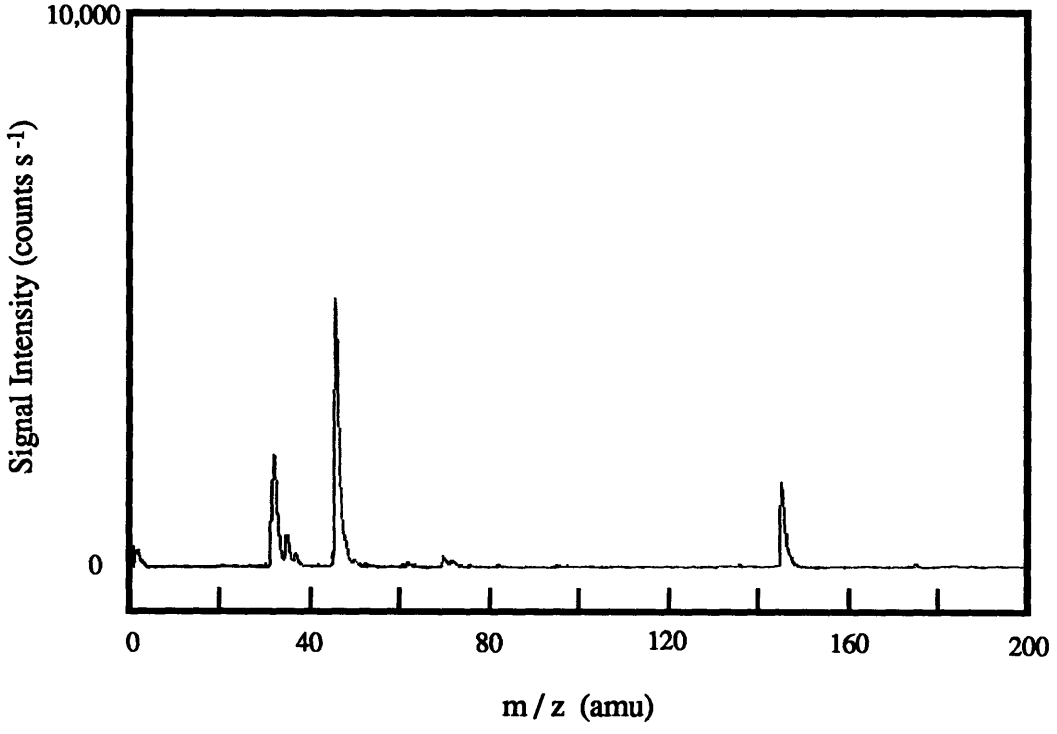

Figure 3. Mass spectrum obtained when only N_2 is passed down the flow tube. The needle was positioned 2 cm upstream of the front aperture.

Most of the peaks in figure 3 are due to trace impurities. The peaks observed at 32 and 46 amu are due to O_2^- and NO_2^- respectively, while the peak at 146 is due to residual SF_6^- leftover from previous experiments. When the distance between the corona discharge and the front aperture was increased to 9.5 cm, the intensity of all of the peaks were observed to decrease by approximately 50%.

When a trace amount of SF_6 was added to the flow, the peak at 146 amu (SF_6^-) drastically increased in intensity (see figure 4). A smaller peak due to SF_5^- was observed at 135 amu.

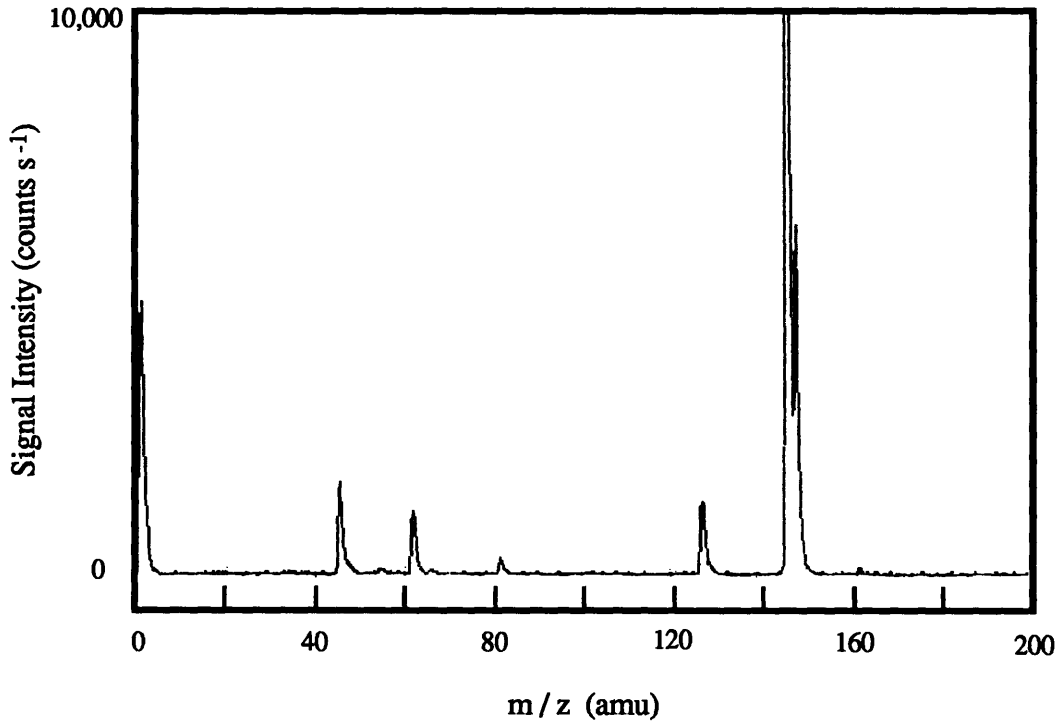

Figure 4. Mass spectrum obtained when appromately 1 ppm of SF_6 is added to the flow of N_2. The needle was positioned 2 cm upstream of the front aperture.

The formation of SF_6^- and SF_5^- is most likely via

$$\begin{aligned} e^- + SF_6 &\rightarrow SF_6^- \\ &\rightarrow SF_5^- + F \end{aligned} \qquad (1)$$

At room temperature, *Fehsenfeld* [1972] observed reaction 1 to proceed with a rate constant of 2.2×10^{-7} cm^3 s^{-1} with the SF_5^- / SF_6^- branching ratio to be approximately 0.1. Note that adding SF_6 to the flow results in a loss of the O_2^- signal at 32 amu. This result agrees with findings of *Streit* [1982] who observed the rate of $O_2^- + SF_6 \rightarrow SF_6^- + O_2$ to be much faster than the reverse reaction. When the distance between the corona and the front aperture was increased to 9.5 cm the SF_6^- peak was observed to decrease in intensity by approximately 90%, while the rest of the peaks only slightly decreased in intensity (~30%).

HCl Spectra

When HCl was added to the flow of N_2 (with no SF_6 added), peaks were observed at 35 and 37 amu. Figure 5 shows a spectrum obtained with 20 ppb of HCl in a flow of N_2. The pair of peaks observed at 35 and 37 amu were both due to Cl^- (the natural isotopic abundance of ^{37}Cl is roughly 33% of ^{35}Cl). The most likely reactions leading to the formation of Cl^- are

$$O_2^- + HCl \rightarrow Cl^- + HO_2 \qquad (2)$$

$$NO_2^- + HCl \rightarrow Cl^- + HNO_2 \qquad (3)$$

both of which have been shown by *Ferguson et al.* [1972] to have rate constants larger than 1×10^{-9} molecule cm^{-3} s^{-1}. The spectrum in figure 5 also shows a series of peaks at 71, 73, and 75 amu, and a series of peaks at 83 and 85. Based on their relative intensities, the series of peaks beginning at 71 amu were most likely due to $HCl \cdot Cl^-$ formed by

$$Cl^- + HCl \rightarrow HCl \cdot Cl^- \quad (4)$$

and peaks at 83 and 85 are most likely due to

$$Cl^- + NO_2 \rightarrow Cl\,NO_2^- \quad (5)$$

Unfortunately, the rate constants for reactions 4 and 5 have not previously been determined.

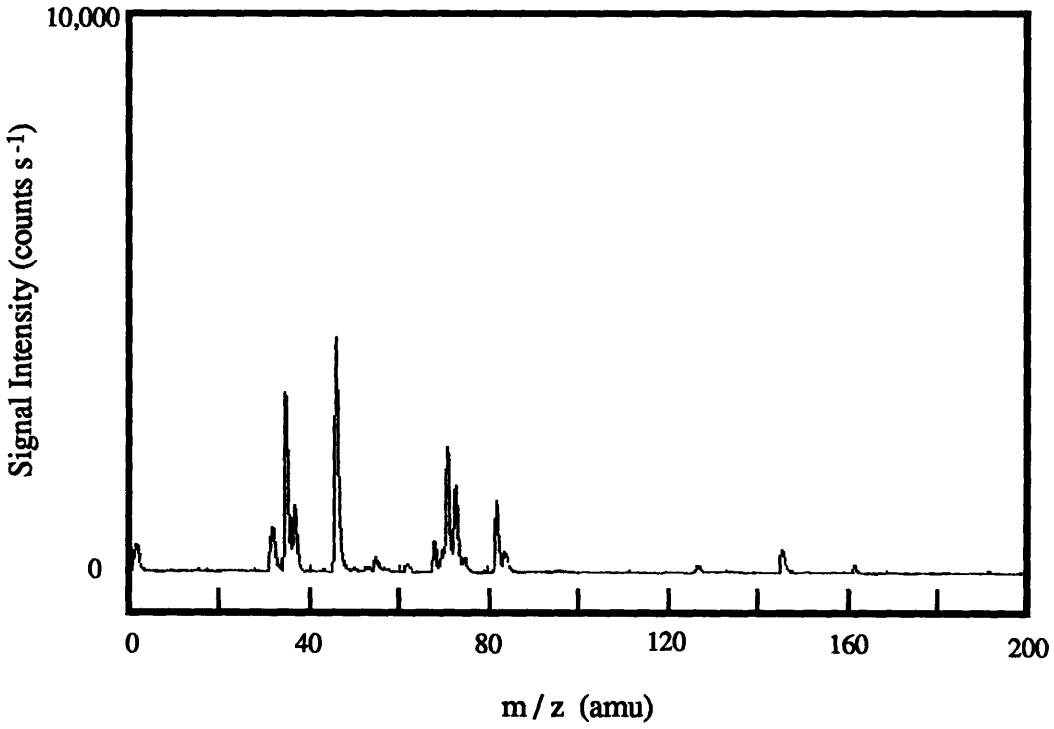

Figure 5. Mass spectrum obtained when approximately 20 ppb of HCl is added to a flow of N_2. The needle was positioned 2 cm upstream of the front aperture.

When the distance between the corona and the front aperture was increased to 9.5 cm the series of peaks at 71, 73, and 75 amu did not change in intensity while the rest of the peaks greatly decreased in intensity.

When a trace amount of SF_6 (~1 ppm) was added to the HCl / N_2 flow, the spectrum changed. Adding SF_6 to the flow caused peaks to be formed at 55, 57, 162, and 164 amu in addition to the SF_5^- and SF_6^- peaks at 137 and 146 amu respectively (see figure 6). Also note that the intensity of the SF_5^- peak is much larger than observed when only SF_6 is added to the flow (see figure 4).

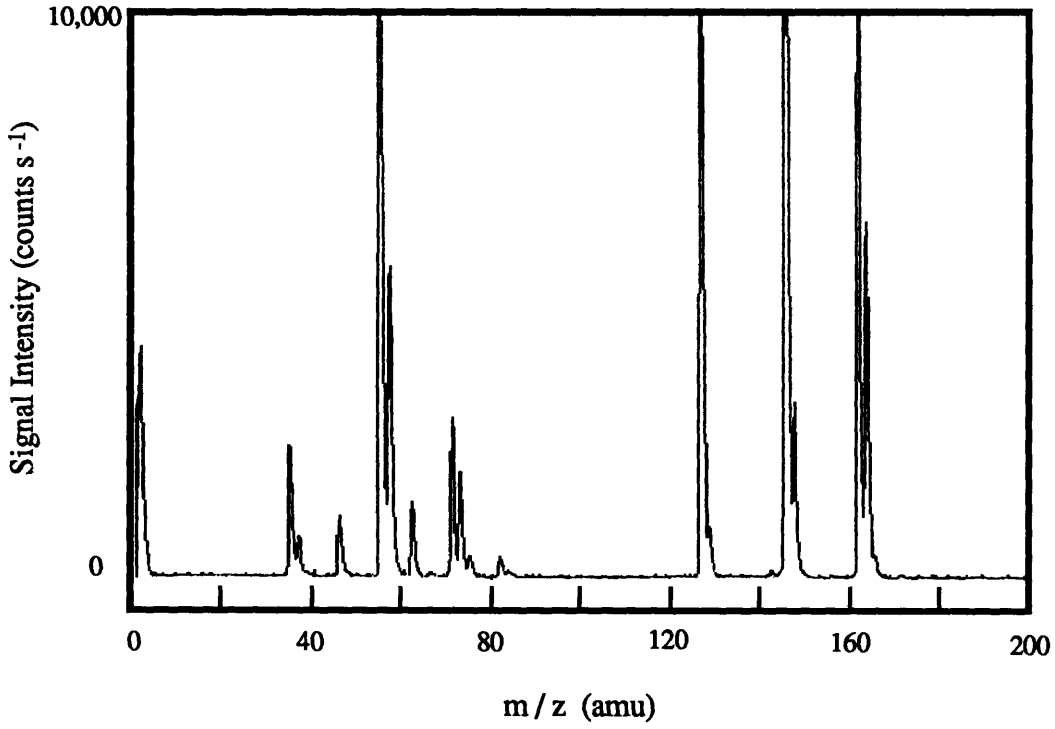

Figure 6. Mass spectrum obtained when approximately 1 ppm of SF_6 is added to a flow of 20 ppb of HCl in N_2. The needle was positioned 2 cm upstream of the front aperture.

The main features of the HCl / SF_6 / N_2 spectrum are probably due to the products of the reaction of SF_6^- with HCl. *Streit* [1982] has shown that this reaction proceeds through the following three product channels

$$\begin{aligned} SF_6^- + HCl &\rightarrow SF_5 + FHCl^- \\ &\rightarrow HF + SF_5Cl^- \\ &\rightarrow HF + Cl + SF_5^- \end{aligned} \qquad (6)$$

with a rate constant of 4.2 x 10^{-10} molecule cm^{-3} s^{-1}. When the distance between the corona and the front aperture was increased to 9.5 cm, the series of peaks due to $HCl{\bullet}Cl^-$ did not change in intensity while the rest of the peaks greatly decreased in intensity.

Molecular Chlorine Spectra

When 12 ppb of Cl_2 was added to the flow of N_2 (with no SF_6 added) and the corona was 2 cm from the front aperture, several groups of peaks were observed: a pair of peaks at 35 and 37 amu, three peaks at 70, 72, 74 amu, and a series of six peaks starting at 105 amu (see figure 7). The pair of peaks observed at 35 and 37 amu are due to Cl^-. Some potential mechanisms for the formation of Cl^- are

$$e^- + Cl_2 \rightarrow Cl^- + Cl \qquad (7)$$

$$O_2^- + Cl_2 \rightarrow Cl^- + ClO_2 \qquad (8)$$

both of which have been shown by *Streit* [1982] to have large rate constants. On the basis of their relative intensities, the series of peaks beginning at 70 amu are due to Cl_2^- which was likely to be formed by

$$NO_2^- + Cl_2 \rightarrow NO_2 + Cl_2^- \qquad (9)$$

or

$$O_2^- + Cl_2 \rightarrow O_2 + Cl_2^- \quad (10)$$

The series of peaks beginning at 105 amu are due to Cl_3^-. A likely mechanism for the formation of Cl_3^- is

$$Cl^- + Cl_2 + M \rightarrow Cl_3^- + M \quad (11)$$

Reaction 11 has been shown by *Babcock and Streit* [1982] to have a third order rate constant of 0.9×10^{-29} cm^6 $molecule^{-2}$ s^{-1}.

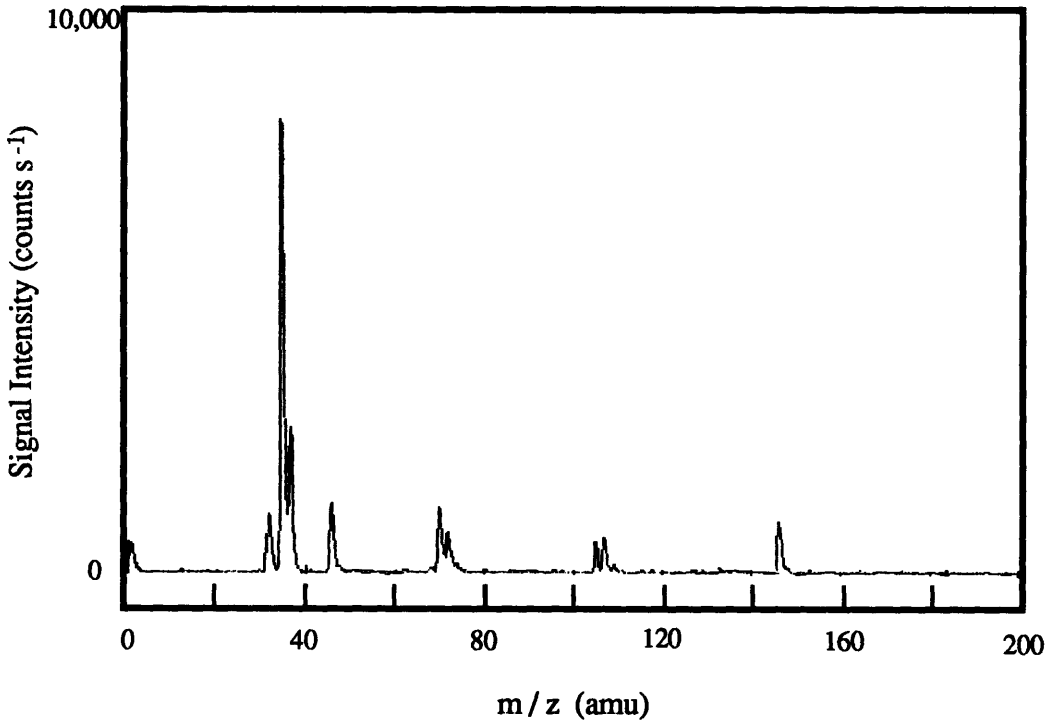

Figure 7. Mass spectrum obtained when approximately 12 ppb of Cl_2 was added to a flow of N_2. The needle was positioned 2 cm upstream of the front aperture.

When the distance between the corona and the front aperture was increased to 9.5 cm the series of peaks due to Cl_2^- decreased in intensity by approximately 50% while the rest of the peaks were barely detectable.

When a trace amount of SF_6 (~1 ppm) was added to the Cl_2 / N_2 flow, the spectrum changed (see figure 8). Adding SF_6 to the flow caused the peaks at 35 and 37 amu to be reduced, while the peaks at 70, 72 and 74 amu increased in intensity.

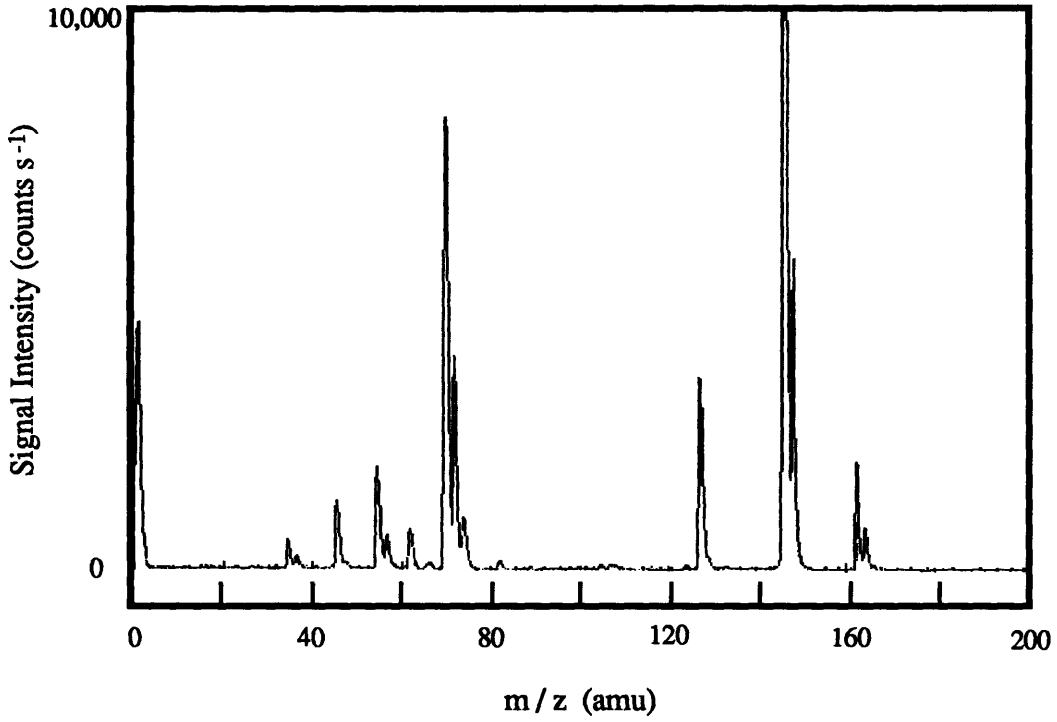

Figure 8. Mass spectrum obtained when approximately 1 ppm of SF_6 is added to a flow of 12 ppb of Cl_2 in N_2. The needle was positioned 2 cm upstream of the front aperture.

The reduction of the Cl^- peaks is probably due to the ability of SF_6 to scavenge electrons and to remove negative charge from O_2^-. As a result, reactions 7 and 8 (which form Cl^-) are minimized. The increase in the peaks at 70, 72 and 74 is most likely due to the following reaction

$$SF_6^- + Cl_2 \rightarrow SF_6 + Cl_2^- \quad (12)$$

Reaction 12 has been shown by *Streit* [1982] to have a rate constant of 6.1×10^{-11} molecule cm^{-3} s^{-1}. There were also small peaks formed at 55 and 57 amu and 162 and 164 amu. These peaks are probably caused by a small amount of HCl on the exterior of the permeation tube. These peaks decreased in intensity as the amount of time the Cl_2 permeation tube was left in the dilution system increased. When the distance between the corona and the front aperture was increased to 9.5 cm, the series of peaks due to Cl_2^- were observed to decrease in intensity by approximately 50% while the rest of the peaks were barely detectable.

Sensitivity Analysis

The sensitivity of the API-MS system was determined by monitoring the intensity of a selected peak while varying the amount of HCl or Cl_2 injected into the flow tube. In order to ensure good mixing, the trace species of interest (HCl or Cl_2) was added to the main carrier gas stream before being injected at the rear of the flow tube. We found that maximum sensitivity was obtained when a small quantity of SF_6 was added to the flow and when the corona was placed approximately 3.5 cm upstream of the mass spectrometer front aperture. A typical curve obtained for HCl is shown in figure 9. The intensity of the peak at 55 amu ($FHCl^-$ formed by reaction 6) was observed to vary linearly with the concentration of the HCl when [HCl] was greater than 0.2 ppb. Below 0.2 ppb the peak intensity was observed to remain fairly constant. We believe this is a result of HCl adsorbed on the interior surfaces of the flow tube system. A typical curve obtained for Cl_2 is shown in figure 10. The intensity of the peak at 70 amu (Cl_2^-) was observed to vary linearly with the concentration of the Cl_2 when [Cl_2] was greater than 0.15 ppb. Below

0.15 ppb the peak intensity was observed to remain fairly constant. Again, we believe this is a result of Cl_2 adsorbed on the interior surfaces of the flow tube system.

For both HCl and Cl_2, we believe that our high pressure ionizing mass spectrometer system is currently capable of detecting concentrations as low as 0.1 ppb. At atmospheric pressure, this corresponds to a detection sensitivity of approximately 2.4×10^9 molecule cm^{-3}. This detection limit is adequate for many kinetic studies.

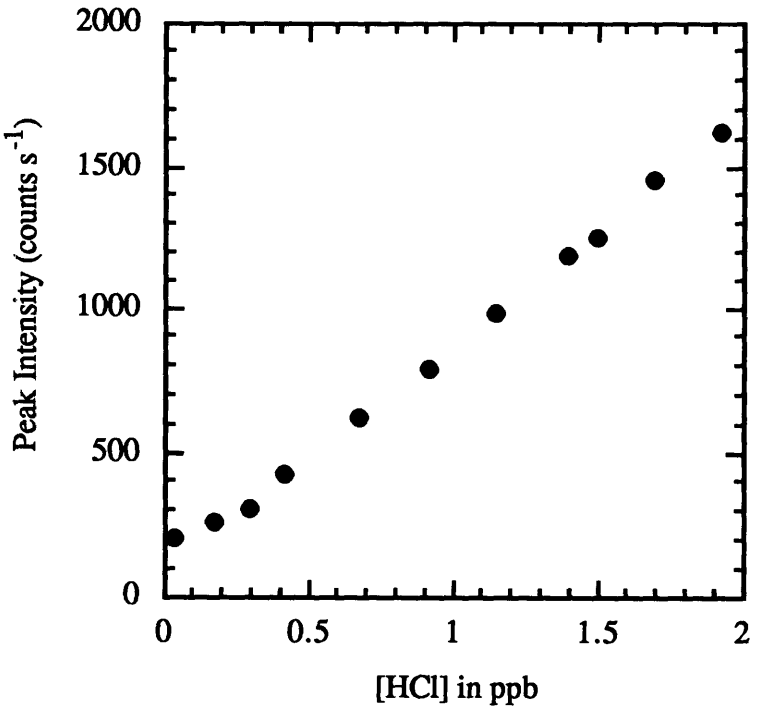

Figure 9. Plot of the peak intensity at 55 amu ($FHCl^-$) as a function of HCl concentration. The SF_6 concentration was 100 ppb. The corona was 3.5 cm from the front aperture.

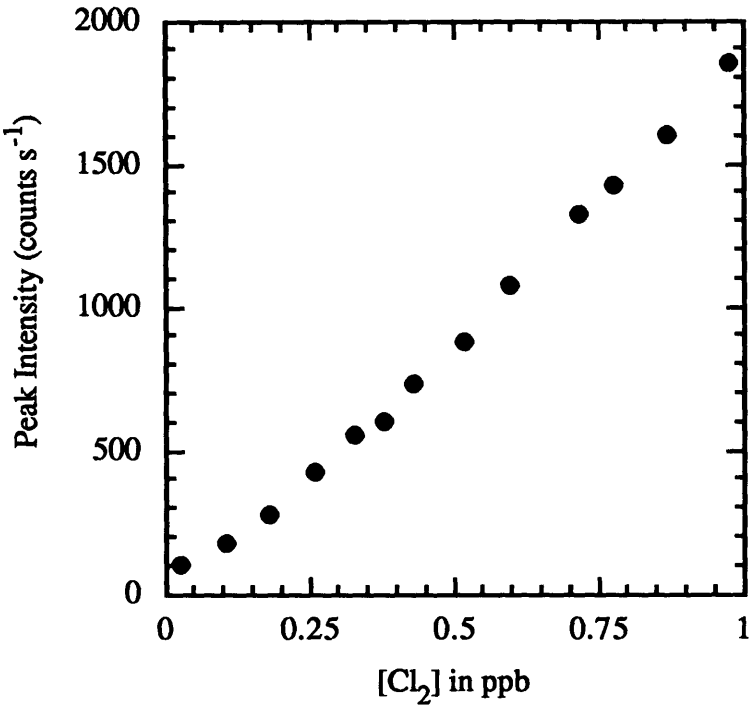

Figure 10. Plot of the peak intensity at 70 amu (Cl_2^-) as a function of Cl_2 concentration. The SF_6 concentration was 100 ppb. The corona was 3.5 cm from the front aperture.

VII.3 Ongoing Studies

We are currently attempting to apply the high pressure ionizing mass spectrometer to the detection of reactive species such as ClO, HO_2, HOCl, and OH. Assuming we can detect a few of these species with sensitivites similar to that found for HCl and Cl_2, we plan to use the technique as a detector in a study of

$$\begin{aligned} ClO + HO_2 &\rightarrow O_2 + HOCl \\ &\rightarrow O_3 + HCl \end{aligned} \qquad (13)$$

Central to this effort will be determining the product distribution of reaction 13 over a wide range of temperatures.

References for Chapter VII

Babcock, L. M., and G. E. Streit, Ion-molecule reactions of Cl_2 with Cl^- and F^-, *J. Chem. Phys., 76*, 2407, 1982.

Eisele, F. L., and H. Berresheim, High-pressure chemical ionization flow reactor for real-time mass spectrometric detection of sulfur gases and unsaturated hydrocarbons in air, *Anal. Chem., 64*, 283, 1992.

Eisele, F. L., and D. J. Tanner, Ion-assisted tropospheric OH measurements, *J. Geophys. Res., 96*, 9295, 1991.

Fehsenfeld, Electron attachment to SF_6, *J. Chem. Phys., 53*, 2000, 1970.

Ferguson, E. F., D. B. Dunkin, and F. C. Fehsenfeld, Reactions of NO_2^- and NO_3^- with HCl and HBr, *J. Chem. Phys., 57*, 1459, 1972.

McLuckey, S. A., G. L. Glish, K. G. Asano, and B. C. Grant, Atmospheric sampling glow discharge ionization source for the determination of trace organic compounds in ambient air, *Anal. Chem., 60*, 2220, 1988.

Mohler, O., T. Reiner, and F. Arnold, A novel aircraft–based tandem mass spectrometer for atmospheric ion and trace gas measurements, *Rev. Sci. Instrum., 64*, 1199, 1993.

Streit, G. E., Negative ion chemistry and the electron affinity of SF_6, *J. Chem. Phys., 77*, 826, 1982.

Zhang, R., J. T. Jayne, and M. J. Molina, Heterogeneous interactions of $ClONO_2$ and HCl with sulfuric acid tetrahydrate: implications for the stratosphere, *J. Phys. Chem., 98*, 867, 1994.